Heat assisted spin-transfer torque manipulation on the nanoscale using a spin-polarized scanning tunneling microscope

Dissertation
zur Erlangung des Doktorgrades
am Department Physik
der Universität Hamburg

vorgelegt von
Dipl.-Phys. Gabriela Herzog
aus Homburg

Hamburg
2011

Gutachter der Dissertation:
Prof. Dr. R. Wiesendanger
Prof. Dr. U. Merkt

Gutachter der Disputation:
Prof. Dr. R. Wiesendanger
PD Dr. habil. Guido Meier

Datum der Disputation:
01.07.2011

Vorsitzender des Prüfungsausschusses:
Prof. Dr. M. A. Rübhausen

Vorsitzender des Promotionsausschusses:
Prof. Dr. P. Hauschildt

Dekan der MIN-Fakultät:
Prof. Dr. H. Graener

Abstract

Within the framework of this Ph.D. thesis, spin-transfer torque manipulation on the local scale is demonstrated by means of spin-polarized scanning tunneling microscopy (SP-STM).

The experiments presented are performed on Fe/W(110) monolayer nanoislands, a system exhibiting uniaxial anisotropy. As a first step, the intrinsic, thermally induced switching behavior of several individual nanoislands is investigated as a function of the temperature. The energy barrier and the attempt frequency for the magnetization reversal are determined and analyzed as function of the island size and shape. The reversal is found to occur via domain wall nucleation and propagation through the nanostructure.

Elevated spin-polarized tunnel currents are utilized to manipulate the thermally activated magnetization reversal. The local current injection from the magnetic probe tip leads to a distinct modification of the intrinsic switching behavior. The contributions of spin torque and Joule heating are identified and quantified. Spatially resolved measurements to analyze the modified switching behavior as a function of the lateral position of current injection reveal the role of the Oersted field. Further, heat assisted spin-torque magnetization switching of individual, quasi-stable nanostructures is demonstrated. The effect of spin-polarized current pulses on a static magnetization is investigated at fixed bias polarity. Experiments with varying pulse parameters reveal that the spin torque depends on the current polarization. Spin-polarized current pulses and ramps at alternating bias polarity are utilized to reliably switch the magnetization direction of a nanoisland back and forth. The evaluation of the switching efficiency as a function of the pulse parameters allows for the discrimination and quantification of spin torque and Joule heating. Finally, critical currents for magnetization reversal are determined by the application of triangular current sweeps at different sweep rates. The analysis allows for a comparison of spin torque and Joule heating found by the different manipulation procedures.

Inhaltsangabe

Im Rahmen der vorliegenden Dissertation werden Experimente zur lokalen, spinstrominduzierten Manipulation von magnetischen Nanostrukturen mittels spinpolarisierter Rastertunnelmikroskopie (SP-RTM) vorgestellt.

Monolagige Eiseninseln auf einer (110) Wolframoberfläche dienen als Probensystem mit uniaxialer Anisotropie. Zunächst wird das intrinsische, thermisch induzierte Schaltverhalten individueller Nanoinseln als Funktion der Temperatur untersucht. Die Energiebarriere und die Versuchsfrequenz der Magnetisierungsumkehr werden für Inseln unterschiedlicher Größe bestimmt. Die Analyse in Abhängigkeit der Inselgröße und -form zeigt, dass die Magnetisierungsumkehr über die Nukleation und Diffusion einer Domänenwand durch die magnetischen Partikel erfolgt.

Durch den Einsatz hoher, spin-polarisierter Tunnelströme wird das thermisch aktivierte Schaltverhalten verschiedener Eiseninseln manipuliert. Die lokale Injektion des spin-polarisierten Tunnelstroms mit Hilfe der RTM Spitze führt zu einer Modifikation des intrinsischen Schaltens. Spindrehmoment-Übertrag (engl. Spintransfer torque) und Joule'sches Aufheizen werden als auftretende Effekte herausgearbeitet und quantifiziert. Zusätzlich machen lateral aufgelöste Experimente den Einfluss des Oerstedfeldes auf das Schaltverhalten sichtbar.
Die wärmeunterstützte Manipulation quasistabiler Nanoinseln durch den Übertrag von Spindrehmoment wird demonstriert. Zunächst werden bei fester Stromrichtung spin-polarisierte Strompulse verschiedener Länge und Amplitude verwendet um die Magnetisierung einer Eiseninsel zu schalten. Durch die Variation der angelegten Probenspannung wird die Polarisationsabhängigkeit des Spindrehmoments gezeigt. Anschliessend wird die Magnetisierung einer Insel aus rund 40 Atomen durch Strompulse alternierender Polarität gezielt und reversibel geschaltet. Die Unterscheidung und Abschätzung der Effekte von Spindrehmoment und Joule'schem Aufheizen erfolgt anhand der Schaltwahrscheinlichkeit in Funktion der Pulshöhe, Pulslänge und Pulsrichtung. Die Verwendung von Stromrampen bei verschiedenen Rampengeschwindigkeiten schliesslich erlaubt die direkte Bestimmung der kritischen Stromdichte für die Magnetisierungsumkehr der Nanoinseln.

Contents

Chapter 1

Introduction

The first reports on the experimental evidence of the effect of an electric current on a magnet can be traced back 200 years. In 1820, the Danish physicist Hans Christian Oersted, professor of physics at the University of Copenhagen, attracted the public interest with his four page essay entitled "Experimenta circa effectum conflictus electrici in acum magneticam" (Latin: "Experiments on the effect of an electrical conflict [current] on a magnetic needle"). Oersted observed an effect on a magnet when connecting a wire in the vicinity to the ends of a voltaic battery. He discovered that the current itself caused the magnet to move: The discipline of electrodynamics was born[1]. A series of discoveries (including Ampere's law describing the force between two parallel conductors, and Faraday's law of electromagnetic induction) and technical developments (the galvanometer and the telegraph system) followed shortly after. The explanation of the observed effects was elaborated over the years resulting in the four prominent Maxwell equations and the Lorentz law that are the basis for classical electrodynamics as it is known today. And a vast number of technical applications, such as electromotors, relais, and speakers just to name a few, still rely on the interplay between the "classical" electric current (as a charge flow) and electromagnets or permanent magnets.

In 1856, William Thomson, Baron Kelvin, who is mainly known for his scientific achievements in the field of thermodynamics, reported on experiments with iron wires in magnetic fields. He found different electric conductivities of the wires when sending the current "along [...] or across the lines of magnetization" [1]. This was the first observation of magnetoresistivity, where the electrical current flow *through* a structure is affected by its magnetic properties. The effect Thomson

[1] Actually, there still is a discussion on whether the Italian jurist and amateur physicist Gian Domenico Romagnosi should be given the credit for the discovery of electromagnetism. He worked on a similar experimental setup as Oersted and published his results already in 1802 (18 years before Oersted's work). However, the unclear description of his experimental procedure prevents an unambiguous interpretation of his observation.

observed, in particular, is known today as *anisotropic magnetoresistance* (AMR). It originates from the spin-orbit interactions of electrons inside the ferromagnet, i.e. from a quantum mechanical effect. Thus, it is no surprise that this time a whole century passed between the discovery of an effect and the development of a technical application: the AMR was found 40 years before Joseph J. Thomson accomplished the experimental proof of the electron's existence as electrically charged particle [2]. It took approximately 30 additional years to discover and prove the electron's non-classical spin nature, its intrinsic and quantized angular momentum and its magnetic moment as additional degree of freedom [3]. Today, the AMR effect has its main application in magnetic field sensors.

With the technical developments on the preparation of thin films, hybrid layer systems consisting of different materials came into the scope of investigation. In the 1970s, Michel Jullière could demonstrate a magnetoresistance effect in *magnetic tunnel junctions* (MTJ), where the electron current is sent through two ferromagnetic layers separated by a thin, non-conducting barrier [4]. The conductance of the junction was shown to depend on the relative magnetic orientation of the two ferromagnetic layers. Since the *tunnel magnetoresistance* (TMR) effect observed was small, it was initially paid only a little attention.
Today's most prominent magnetoresistance effect was first observed in 1988 by Peter Grünberg and Albert Fert, who were honored in 2007 with the Nobel prize for their investigations. Both were working on hybrid systems of magnetic and non-magnetic metallic layers and observed independently a resistance dependency on the relative magnetization orientation of the ferromagnetic layers: the *giant magnetoresistance* effect (GMR). Soon this effect was utilized in hard disc drive read heads.

The rediscovery of magnetoresistance for technical applications resulted in the vast growth of the research field of spin-dependent transport. In 1996, Luc Berger and John C. Slonczewski independently predicted in their theoretical works the existence of current-driven magnetic excitation processes in the metallic multilayer structures of GMR devices [5, 6]. An unpolarized current sent through such a device becomes spin-polarized when passing through the first, so-called "fixed" ferromagnetic layer and then transfers spin angular momentum to the second, "free" ferromagnetic layer. This so-called *spin-transfer effect* at the interface between a non-magnetic and a ferromagnetic layer can be sufficiently high enough to achieve a steady precession of the free layer's magnetization by the exerted torque, or even lead to magnetization reversal when adjusted appropriately. In contrast to the long-range Oersted field generated by a current, spin-transfer torque provides the possibility of local magnetization manipulation. This novel form of current-induced magnetization switching (CIMS) became famous under the name *spin-transfer torque (STT) switching*. In 2000, Katine and coworkers succeeded in

demonstrating STT switching in all-metallic GMR devices [7], and 4 years later it was also shown in magnetic tunnel junctions [8, 9]. When Stuart Parkin and coworkers reported a "giant tunnel magnetoresistance at room temperature with MgO tunnel barriers" [10], magnetic tunnel junctions came again into play for possible technical (STT) applications.

One application currently under development that utilizes spin-transfer torque switching is the spin-torque magnetic random access memory (ST-MRAM) [11]. MRAM itself has recently become highly interesting because of its combination of several of the benefits of common solid-state drives. It is non-volatile like Flash memories, and fast like dynamic and static RAM (DRAM/SRAM). The idea behind MRAM is bit storage in magnetic tunnel junctions, where the free layer is magnetized either parallel or antiparallel with respect to the fixed layer ("0" or "1"). Whereas in conventional field MRAM the free layers are switched by the Oersted field generation through nearby current lines [12], in ST-MRAM the write current is passed directly through the magnetic tunnel junction to switch the free magnetic layer. Thus, a less complex RAM architecture is possible [13]. Especially for portable electronics (mobile phones, laptops, etc.) such a non-volatile and low power consuming memory device is of great interest.

Parallel to the evolution of magnetoresistance devices for information technology, an important milestone was achieved in the field of surface science: the invention of the scanning tunneling microscope (STM) as a new surface investigation technique. In a STM setup, two electrically conducting electrodes, the atomically sharp probe tip and the sample surface, are placed in a non-conducting medium. Both are biased and the distance between tip and sample is lowered until a tunnel current starts to flow - typically at a distance of some Å. In March 1981, Gerd Binnig, Heinrich Rohrer, and coworkers performed the first tunneling experiments with a tungsten tip on a platinum surface. The measurements of the tunnel current as function of the tip-sample distance demonstrated the feasibility of "vacuum tunneling with externally controllable tunnel distance" [14]. In the same year, surface microscopy was performed resulting in atomic scale topography images of different surfaces [15]. Here, recording the tip-sample distance while scanning the surface laterally at constant tunneling current allows to map the surface topography - scanning tunneling microscopy was born. For the first time scientists had direct access to atomic scale topography of surfaces in real space. Additionally, the observation of dynamic surface processes, such as diffusion or growth, became possible. And further, the spectroscopic operation modes of the instrument allowed the scientists to investigate electronic properties on the local scale. Both, Binnig and Rohrer were awarded the Nobel prize in 1986 for their design of the STM.

In 1990, the first spin-polarized (SP) STM experiments were performed which demonstrated the spin dependence of the tunnel current when using a magnetic sample and probe tip [16], thus utilizing the instrument as a TMR device. Roland Wiesendanger and coworkers chose the surface of Cr(001) as a sample system that was predicted to show a topological antiferromagnetic order, i.e. neighboring ferromagnetic terraces separated by monatomic steps should show alternating magnetization directions. For comparison, a non-magnetic tungsten tip and a ferromagnetic CrO_2 tip were used to record constant current topography images of the Cr(001) surface. Indeed, while the non-magnetic tungsten tip mapped regular steps of one atomic height on the surface, the magnetic tip revealed an alternating step height between adjacent terraces due to spin-polarized electron tunneling. The magnetic contrast in STM measurements was confirmed. (SP) STM became over the years a very powerful technique that has found various applications ranging from mapping magnetic order on the nanoscale [17], measurements on magnetization curves of individual adatoms [18], and time-resolved studies to investigate fast magnetization dynamics [19], to single atom manipulation [20].

The aim of this work is to demonstrate and investigate the spin-torque manipulation on the local scale by means of SP-STM. The natural TMR setup of the SP-STM junction is utilized to control the magnetization of individual nanostructures by the local injection of a spin-polarized tunnel current through the magnetic STM probe tip. This thesis is organized as follows:
Chapter 2 is dedicated to the SP-STM as a general measurement technique. After the treatment of the one-dimensional tunnel effect, the Tersoff-Hamann theory of electron tunneling between probe tip and sample will be discussed. Finite-bias effects on the tunnel current are examined, before coming to the tunneling between two magnetic electrodes for spin-polarized STM. At the end of this chapter, we will summarize the experimental requirements arising from the above mentioned considerations.
Chapter 3 will treat the theoretical background of spin-transfer torque switching. After the introduction of the spin-transfer effect, the concept of spin-transfer torque switching for multilayer structures will be explained. Then, the results of Slonczewski's original work on the spin-transfer torque are recapitulated. In the end, we come to the model of a macro-spin and regard its magnetization dynamics under the influence of a spin-polarized current and a finite temperature.
In *Chapter 4* the experimental setup is introduced, i.e. the ultra-high vacuum system and the variable-temperature microscope, in particular. Further, the probe tip and the sample preparation utilized for the presented experiments are explained.
Chapter 5 will give an overview of the knowledge about the growth and the magnetism of the chosen sample system, Fe/W(110), and focus then on the Fe monolayer nanoislands on the W(110) surface, that will be target of the current-induced manipulation.

In *Chapter 6*, before coming to the manipulation experiments, the intrinsic thermal switching behavior of individual iron nanoislands is investigated. The switching behavior is observed as a function of the temperature, and the energy barrier and the attempt frequency for the magnetization reversal are investigated as function of the island's respective size and shape.
The *Chapters 7* and *8* contain the main experimental work, the spin-transfer torque manipulation of the nanoislands. First, in Chapter 7, elevated spin-polarized tunnel currents are utilized to manipulate the magnetization switching in the *thermally activated* regime. The distinct modification of the intrinsic switching behavior due to the elevated current injection is analyzed as a function of the tunnel parameters and the lateral position of current injection. Different effects of the elevated current are identified and quantified.
In *Chapter 8*, the effect of current pulses and ramps on individual, *quasi-stable* nanostructures is investigated. The effect of high, spin-polarized current pulses and ramps on the magnetic nanoislands is observed, first at fixed bias polarity, then at alternating current directions. The evaluation as function of pulse parameters will reveal the impact of the different parameters. Finally, we will compare and discuss the results and summarize the dissertation in *chapter 9*.

Chapter 2

The theory of spin-polarized scanning tunneling microscopy

In scanning tunneling microscopy (STM) two electrically conducting electrodes, probe tip and sample, are placed in a non-conducting medium and biased. Then the distance between them is lowered to some Å until a current starts to flow. The underlying physical mechanism to obtain this current emanates from quantum mechanics and is called the tunnel effect.
This chapter is dedicated to the theoretical background of STM as an experimental technique. After introducing the one-dimensional tunnel effect as a basic principle, we will examine the Tersoff-Hamann theory of electron tunneling including the electronic structure of probe tip and sample. The following section will summarize the effect of a finite bias on the tunnel current. Then we will treat the tunneling between two magnetic electrodes for spin-polarized (SP) STM. At the end of this chapter we will look at the experimental requirements arising from these considerations.

2.1 The tunnel effect

In classical mechanics, a particle having the energy E can not overcome a potential barrier of the height $V_0 > E$. It will be reflected at the potential wall. In quantum mechanics particles are described by wave functions $\Psi(x)$ and have a non-zero probability to penetrate a potential barrier and to *tunnel* through the barrier. It easily can be demonstrated for the one dimensional case (see Figure 2.1).
Let us assume a stepped potential $V(x)$ forming a wall,

$$V(x) = \begin{cases} 0 & \text{for} \quad x < 0 \quad \text{(region I)} \\ V_0 & \text{for} \quad 0 \leq x \leq d \quad \text{(region II)} \\ 0 & \text{for} \quad x > d \quad \text{(region III).} \end{cases}$$

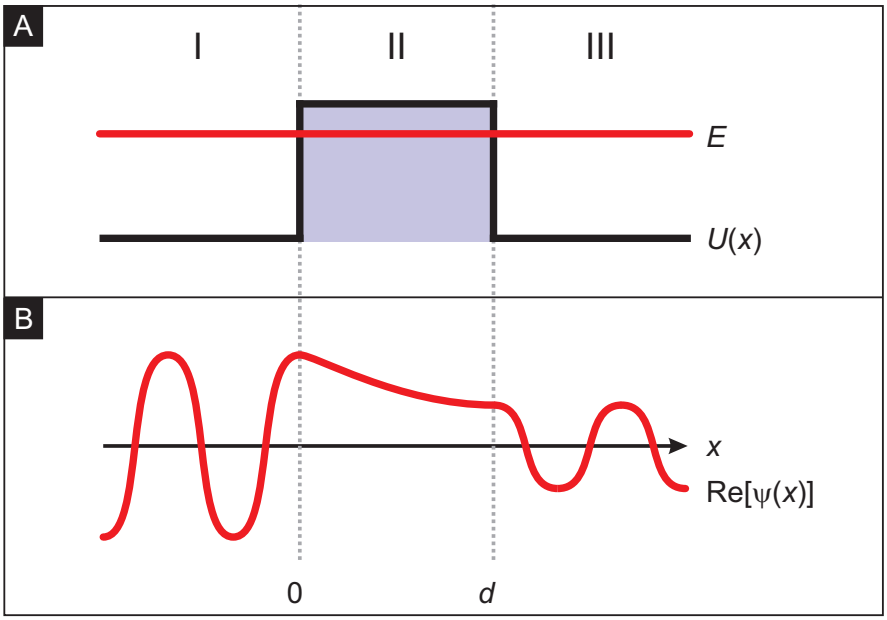

Figure 2.1: The tunnel effect (**A**) Schematic energy landscape $U(x)$. A particle with energy E passes region I coming from the left. It has a nonzero probability to pass the potential barrier in region II and to reach region III. (**B**) The wave function $\Psi(x)$ of the particle has to fulfill continuity conditions at the borders of region II, positions 0 and d, for a solution of the time dependent Schrödinger equation to exist.

An electron with the wave function $\Psi(x)$ and the energy E enters region I from the left. The wave function has to satisfy the time-dependent Schrödinger equation

$$\left[V(x) - \frac{\hbar^2}{2m}\frac{\mathrm{d}^2}{\mathrm{d}x^2}\right]\Psi(x) = E\Psi(x) \quad , \tag{2.1}$$

where m denotes the electron mass, and $\hbar$ is Planck's constant. This leads to the general ansatz

$$\mathrm{I}: \ \Psi_{|}(x) = A\mathrm{e}^{\mathrm{i}kx} + B\mathrm{e}^{-\mathrm{i}kx} \tag{2.2}$$

$$\mathrm{III}: \ \Psi_{|||}(x) = C\mathrm{e}^{\mathrm{i}kx} + D\mathrm{e}^{-\mathrm{i}kx} \tag{2.3}$$

$$\text{with} \quad k = \frac{\sqrt{2mE}}{\hbar} \tag{2.4}$$

for regions I and III where $V(x) = 0$. A, B, C and D are, in the first instance, arbitrary coefficients. In region I, the incoming wave ($A\mathrm{e}^{ikx}$) and the reflected wave at the barrier ($B\mathrm{e}^{-ikx}$) superimpose upon one another, whereas the wave in region III ($C\mathrm{e}^{ikx}$) leaving to $+\infty$ is not reflected. Therefore $D = 0$. For the region

II one can write

$$\text{II}: \ \Psi_{||}(x) = F\mathrm{e}^{\mathrm{i}k'x} + G\mathrm{e}^{-\mathrm{i}k'x} \tag{2.5}$$

$$\text{with} \quad k' = \frac{\sqrt{2m\,(E - V_0)}}{\hbar} \quad , \tag{2.6}$$

or with κ, the inverse decay constant

$$\kappa^2 = -k'^2 = \frac{2m\,(V_0 - E)}{\hbar^2} \tag{2.7}$$

$$\Rightarrow \text{II}: \ \Psi_{||}(x) = F\mathrm{e}^{-\kappa x} + G\mathrm{e}^{\kappa x} \quad . \tag{2.8}$$

Since $E - V_0 < 0$, k' is imaginary, the exponents are real and the particle is described by an exponentially damped wave (see Fig. 2.1). The coefficients A, B, C, F and G are given by the requirement of continuity of the wave function and its derivative at the discontinuities of the potential ($x = 0$ and $x = d$) and the normalization $\int \mathrm{d}x\,|\Psi^2(x)| = 1$.
The transmission coefficient of the wave through the barrier T is given by the ratio of incident and transmitted current density, j_0 and j_t, defined by $j = \frac{\hbar}{2im}\,(\Psi^*\nabla\Psi - \Psi\nabla\Psi^*)$. Inserting the wave functions results in

$$T = \frac{j_T}{j_0} = \frac{1}{1 + \frac{(k^2+\kappa^2)^2}{4k^2\kappa^2} \cdot \sinh^2(\kappa d)} \quad . \tag{2.9}$$

In the limit of a strongly attenuating barrier ($\kappa d \gg 1$) one can find the approximation

$$T \approx \frac{16k^2\kappa^2}{(k^2+\kappa^2)^2} \exp(-2\kappa d) \quad . \tag{2.10}$$

This equation explains the high vertical resolution of the STM technique. The tunnel probability and therefore the tunnel current depend exponentially on the barrier width d given by the distance between the tip and the sample in the experiment.

2.2 The Tersoff-Hamann model of STM

In 1985, Tersoff and Hamann presented a theory for tunneling in a STM geometry, i.e. between a surface and a model tip, that includes the electronic structure of both electrodes [21]. Bardeen's first-order time-dependent perturbation theory treatment of tunneling [22] was applied to describe the tunneling of electrons in a STM. The wave functions of tip and sample were considered as separate and undisturbed systems, and the wave function of the whole system was calculated by solving the time-dependent Schrödinger equation including a perturbation given

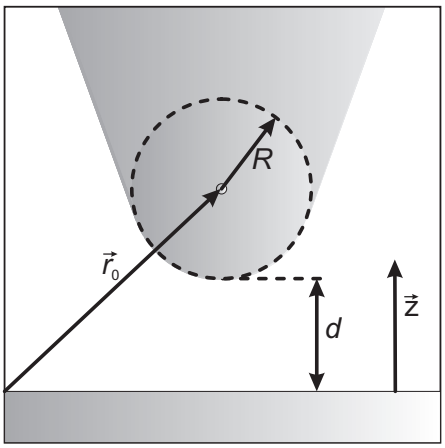

Figure 2.2: Tunneling geometry within the Tersoff-Hamann model. R denotes the effective tip radius from the center of curvature of the tip r_0. The tip sample distance is d.

by the tip potential. A sketch of the considered geometry is shown in Fig. 2.2, where R is the effective tip radius and r_0 the center of curvature. The tip is modeled as a locally spherical potential well where it approaches nearest the surface and only s-type tip wave functions of the form

$$\Psi_\mu = \frac{1}{R} \exp(-\kappa R) \tag{2.11}$$

were considered for the calculations. κ again denotes the inverse decay length for the tip wave function in vacuum, $\kappa = \frac{\sqrt{2m\phi}}{\hbar}$ where ϕ is the work function. As a result, the following expression for the tunnel current I is obtained for the limit of zero temperature and low bias voltage:

$$I \propto U \cdot \rho_t(E_F) \cdot \exp(2\kappa R) \cdot \sum_\nu |\Psi_\nu(\vec{r}_0)|^2 \cdot \delta(E_\nu - E_F) \quad , \tag{2.12}$$

where $\rho_t(E_F)$ denotes the density of states (DOS) of the tip at the Fermi energy E_F, and Ψ_ν the wave function of the sample. The sum

$$\sum_\nu |\Psi_\nu(\vec{r}_0)|^2 \cdot \delta(E_\nu - E_F) = \rho_s(E_F, \vec{r}_0) \tag{2.13}$$

is the surface local density of states ρ (LDOS) at the Fermi energy at the effective center of the tip. This is the key to interpreting data obtained with this technique: STM images taken at small bias voltage and at constant current represent areas of constant sample LDOS at E_F evaluated at the center of the tip. Since, for chemically homogeneous samples, the LDOS is a good approximation of the topography, images obtained at constant-current are referred to as "topography" images.

The exponential decay of the sample wave function in the vacuum is proportional to $-\kappa z$. This leads to

$$|\Psi_\nu(\vec{r}_0)|^2 \propto \exp[-2\kappa(d + R)] \quad . \tag{2.14}$$

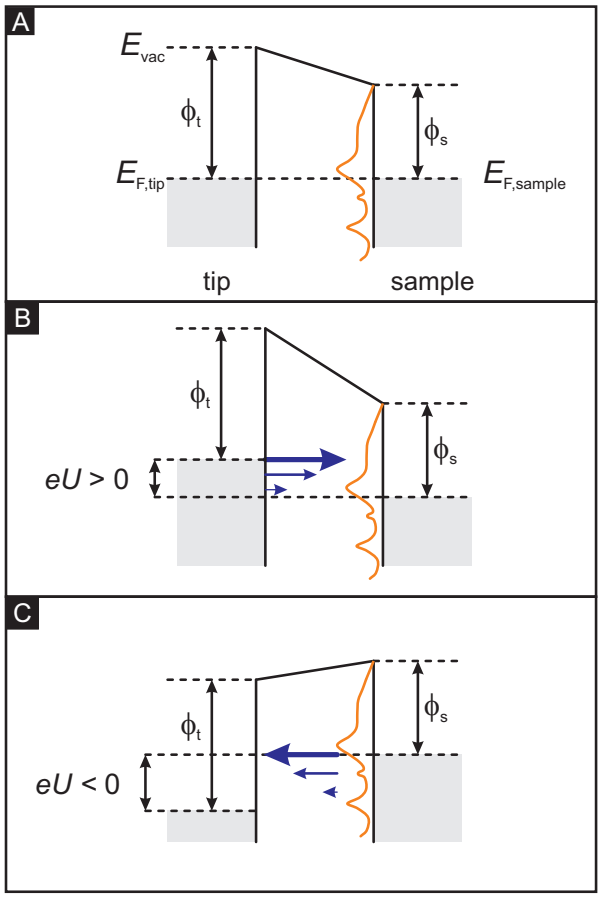

Figure 2.3: Energy diagrams for the tunneling process between the tip and the sample. Filled states are shaded gray. ϕ_i designates the work function. (**A**) If the tip and the sample are close enough to allow for a tunnel current, the Fermi levels of both tip and sample will align: $E_{F,tip} = E_{F,sample}$. A net current will only flow until equilibrium is reached. (**B**) Applying a positive bias voltage U leads to a tunnel current from the tip to the sample. Electrons near the Fermi level experience a smaller energy barrier than the electrons in lower energy states and therefore have a higher contribution to the tunnel current (symbolized by different arrow sizes). (**C**) At negative bias the situation is reversed and electrons tunnel from occupied sample states into unoccupied tip states.

For the tunnel current this results in

$$I \propto \exp\left(-2\kappa d\right) \quad . \tag{2.15}$$

In agreement with the basic treatment of tunneling introduced before the tunnel current I depends exponentially on the tip-sample distance d in the experiment.

2.3 Finite bias effects

The Tersoff-Hamann description of the tunnel current (Eq. (2.12)) holds only in the limit of small bias voltages. The application of a finite bias U to the sample leads to a shift in the energy levels by an amount of eU relative to the tip (e denotes here the electron charge). The tunnel current I then reads to a first approximation

$$I \propto \int_{E_F=0}^{E_1=eU} \rho_s(E)\rho_t(-eU+E)T(E,eU)dE \quad , \tag{2.16}$$

where ρ_t and ρ_s denote the DOS of tip and sample, respectively. The energy- and bias-dependent transmission coefficient T includes the exponential dependency of

the tunnel current on the distance. Thus, the tunnel probability of the electrons depends on their energetic distance to the Fermi level. This will become clearer in the following image. Figure 2.3 shows energy level diagrams for the tip-sample system. The energy states on both sides are occupied to E_F (gray shaded regions). For the sake of simplicity, the tip DOS is taken as featureless. If the tip-sample distance is lowered, a tunnel current I sets in and adjusts the Fermi levels of tip and sample. When equilibrium is reached, i.e. $E_{F,tip} = E_{F,sample}$, the net electron flow stops (Fig. 2.3 (A)). The application of a finite, positive bias voltage U shifts the DOS of the tip with respect to E_F by $+eU$, and electrons tunnel from occupied states of the tip into unoccupied states of the sample (Fig. 2.3 (B)). The electrons coming from tip states close to the Fermi level experience a smaller potential barrier than the electrons from lower levels and therefore have a higher transmission probability. Thus, the tunnel current is predominantly carried by the electrons close to E_F symbolized in the figure by arrows of different thickness. If a negative bias voltage is applied, the situation is reversed (Fig. 2.3 (C)): the DOS of the tip is shifted with respect to E_F by $-eU$. Now, the electrons tunnel from occupied sample states to unoccupied tip states. Thus the bias *polarity* determines whether occupied or unoccupied sample states are probed and the bias *value* selects the electronic states contributing to the tunnel current.

To investigate the electronic properties of the sample the differential conductance $\mathrm{d}I/\mathrm{d}U$ is analyzed. Differentiation of Equation 2.16 yields

$$\frac{\mathrm{d}I}{\mathrm{d}U}(U) \propto \rho_t \rho_s(eU) T(E, eU) + \rho_t \cdot \int_{E_F=0}^{E_1=eU} \rho_s(E) \frac{\mathrm{d}T(E, eU)}{\mathrm{d}U} dE \quad , \tag{2.17}$$

with the approximation that the tip DOS is constant: $\rho_t(E) = const.$.
Since $\frac{\mathrm{d}T(E,eU)}{\mathrm{d}U}$ is often small, the second term can be neglected and the equation reads

$$\frac{\mathrm{d}I}{\mathrm{d}U}(U) \propto \rho_t \rho_s(eU) T(E, eU) \quad . \tag{2.18}$$

Consequently, the differential conductance is a measure for the density of states of the sample ρ_s at the energy eU. Hence, measuring the differential conductance $\mathrm{d}I/\mathrm{d}U$ as a function of the applied bias voltage U allows to gain information of the sample's electronic structure. Figure 2.4 shows again energy level diagrams for the tip-sample system at different applied bias voltages U. As stated before, a positive bias voltage U_1 leads to a tunnel current from the tip to the sample (A). The differential conductance $\mathrm{d}I/\mathrm{d}U$ is then directly proportional to $\rho_s(eU_1)$, the number of empty states available in the sample *at* the energy eU_1 (in contrast to the tunnel current I that is a measure for the energy-*integrated* sample LDOS). When changing the bias voltage to U_2 (B), the differential conductance increases due to the elevated sample LDOS ρ_s at the energy eU_2 in comparison to $\rho_s(eU_1)$. At negative voltages (C) the differential conductance is proportional

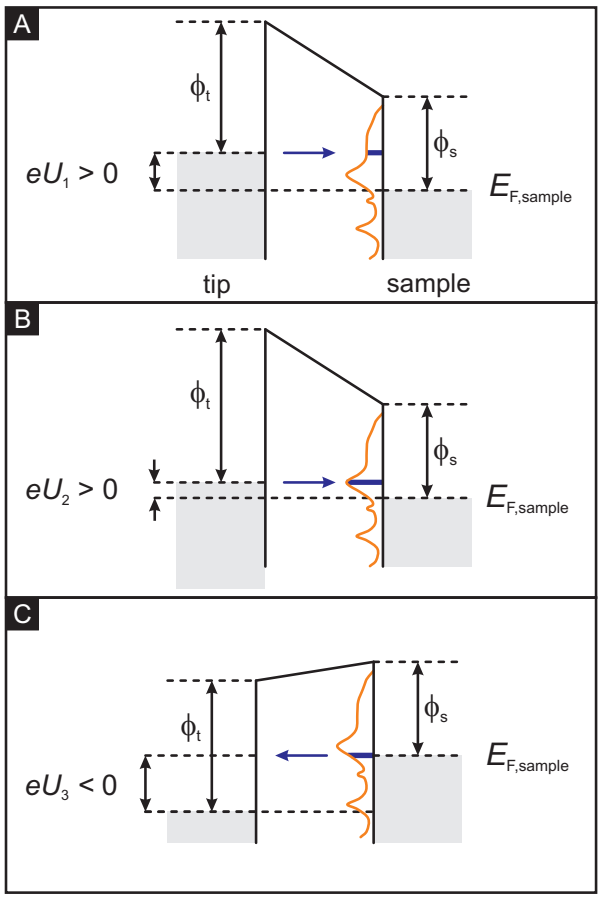

Figure 2.4: Dependency of the differential conductance $\mathrm{d}I/\mathrm{d}U$ on the sample DOS $\rho_s(E)$.
(**A**) At a positive bias voltage U_1 the electrons tunnel from occupied tip states to unoccupied sample states. The signal of differential conductance $\mathrm{d}I/\mathrm{d}U$ is proportional to the sample density of states (DOS) ρ_s at the energy $+eU_1$.
(**B**) Changing the applied bias voltage to U_2 leads to an energetic shift in the density of states: A peak at $+eU_2$ in the sample DOS ρ_s leads to an increased differential conductance $\mathrm{d}I/\mathrm{d}U$.
(**C**) At a negative bias U_3 the tunnel current direction is reversed. The differential conductance is on the sample side governed by electrons around the Fermi level $E_{F,\mathrm{sample}}$.

to the sample LDOS at the Fermi level $E_{F,\mathrm{sample}}$ and the unoccupied tip LDOS at eU_3. Thus, mapping the signal of differential conductance as a function of positive bias voltage allows to probe the unoccupied sample states. In contrast, the $\mathrm{d}I/\mathrm{d}U$ signal at a negative chosen voltage provides information of the sample LDOS at the Fermi level.

In the experiment this is realized by stabilizing the tip at a fixed tip-sample distance and measuring the tunnel current I as a function of the applied bias voltage U while keeping the feedback loop open (switched off). The resulting $I(U)$ curve can then be numerically differentiated. An alternative way to directly measure the $\mathrm{d}I/\mathrm{d}U$ signal is the usage of the lock-in technique. A small, alternating modulation voltage U_{mod} is then superimposed on the bias voltage U, and the tunnel current response at the respective modulation frequency is measured by a lock-in amplifier. Then $\mathrm{d}I/\mathrm{d}U$ (U) can be directly measured in the experiment. For more detailed discussions, the reader is referred to [23, 24]. The differential conductance, however, can give further information about the magnetic properties of the sample and will thus reappear in the following chapter.

2.4 Spin-resolved STM

The spin of the electrons was disregarded thus far in the discussion of the tunnel process. This property is of special interest if magnetic materials are used for both the tip and sample. In 1989, Slonczewski developed a theoretical description for the conductance between two ferromagnetic electrodes separated by a non-magnetic barrier [25]. Using a free-electron model for the conduction electrons, one finds the following expression for the spin-polarized tunnel current I_{SP} in the limit of low bias U:

$$I_{SP} = I_0 \cdot [1 + P_1 P_2 \cos(\theta)] \quad . \tag{2.19}$$

I_0 is the spin-averaged current and θ the angle enclosed by the magnetization directions of the two electrodes. $P_i = \frac{\rho^i_\uparrow - \rho^i_\downarrow}{\rho^i_\uparrow + \rho^i_\downarrow}$ denotes the polarization of the electrode i given by its density of states ρ for the two spin directions $\uparrow$ and $\downarrow$ at the Fermi level. The tunnel current is now dependent on the *spin-resolved* LDOS of the tip and the sample.

We want to illustrate the resulting effect of different magnetic tip-sample configurations on the tunnel current at finite bias. Figure 2.5 compares the situation in the DOS for parallel and antiparallel alignment of tip and sample magnetization. The DOS inside both ferromagnets are spin-split into $\rho_\uparrow$ and $\rho_\downarrow$ due to exchange interaction, leading to majority and minority bands at the Fermi level E_F. Spin- and energy-conservation are considered for the tunnel processes. A positive bias voltage is applied leading to a tunnel current from the tip to the sample. In the parallel configuration (A), the $\downarrow$ electrons tunnel from the occupied $\downarrow$ tip states into the available unoccupied $\downarrow$ sample states. The same holds for the $\uparrow$ electrons but their contribution to the tunnel current I will be small, since fewer electrons and empty sample states are available from the $\uparrow$ tip and sample DOS. In the antiparallel configuration the sample DOS is changed and less empty $\downarrow$ states are now available for the electrons coming from the tip. This leads to a diminution of the tunnel current. For the $\uparrow$ electrons, more unoccupied $\uparrow$ states are now available in the sample but still the $\uparrow$ tip DOS is small. Therefore, the tunnel current in the antiparallel configuration $I_{\uparrow\downarrow}$ will be lower in comparison to the current at the parallel configuration $I_{\uparrow\uparrow}$.

In 1990, the first spin-polarized STM experiments were performed which demonstrated the spin dependence of the tunnel current when using magnetic sample and probe tip [16]. The surface of Cr(001) was investigated with a ferromagnetic CrO_2 tip. This particular sample system exhibits an interesting link between the surface topography and its magnetization: It is a topological antiferromagnet, i.e. adjacent terraces separated by monatomic steps are alternately magnetized, as shown in Figure 2.6 (A). Scanning this surface with a magnetic tip *at a constant*

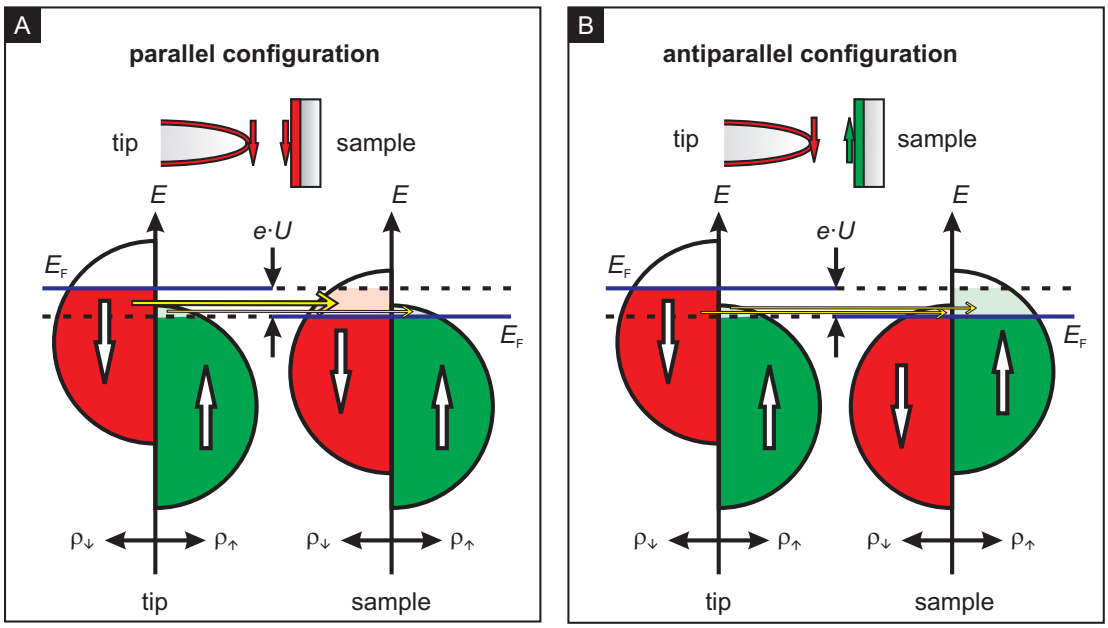

Figure 2.5: Simplified pictures of the spin-polarized tunneling between a magnetic tip and a magnetic sample for positive bias voltage applied. Two possible magnetization configurations of the tip and the sample magnetization are shown, spin- and energy-conservation is assumed. $\rho_{\uparrow,\downarrow}$ denote the *DOS* of the respective electrode and its subband (spin up or spin down). (**A**) The parallel configuration of tip and sample magnetization. The applied bias voltage U shifts the Fermi energy E_F of the electrodes with respect to another. Since many empty states are existent in the sample, many $\downarrow$ electrons can tunnel from the tip to the sample side and a high tunnel current $I_{\uparrow\uparrow}$ can be detected. (**B**) The antiparallel configuration. In this case fewer empty states are available on the sample side for the $\uparrow$ electrons, resulting in a smaller tunnel current $I_{\uparrow\downarrow}$. In both cases the contribution of the $\uparrow$ electrons to the tunnel current is small.

distance d_0, leads to alternating tunnel currents $I_{\uparrow\downarrow}$ and $I_{\uparrow\uparrow}$, according to the changing terrace magnetization orientation with respect to the tip magnetization. As a consequence, the topographic SP-STM images taken in the *constant current mode* show alternating step heights h_1 and h_2 because the feedback loop adjusts the tip-sample distance alternating between $d_1 = d_0 + \Delta d_1$ and $d_2 = d_0 - \Delta d_2$ (B). The apparent step heights are thus $h_1 = h + \Delta d_1 + \Delta d_2$ and $h_2 = h - \Delta d_1 - \Delta d_2$ with h as the real step height. In the limit of low bias, the distance adjustment $\Delta d = \Delta d_1 + \Delta d_2$ can be used to determine the *effective* polarization P of the tunnel junction by

$$P = \frac{\exp\left(A\sqrt{\phi}\Delta d\right) - 1}{\exp\left(A\sqrt{\phi}\Delta d\right) + 1} \quad , \tag{2.20}$$

with ϕ as local barrier height and the constant $A = 1.025\,\mathrm{eV}^{-1/2}\mathrm{\AA}^{-1}$ [16].

Wortmann and coworkers applied the Tersoff-Hamann model to the case of spin-

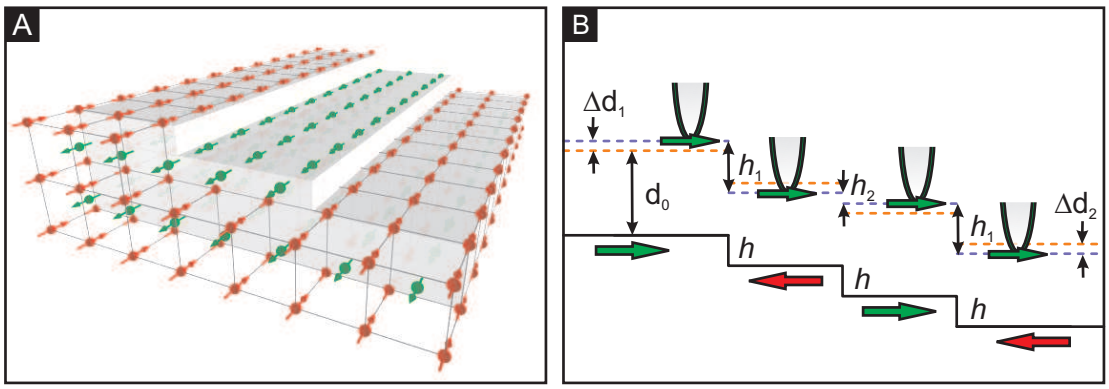

Figure 2.6: (**A**) Schematic drawing of the Cr(001) surface as a topological antiferromagnet. Each terrace is ferromagnetic and adjacent terraces are magnetized antiparallel. (**B**) In SP-STM measurements at *constant current* the step height h appears alternating between h_1 and h_2. Scanning at a *constant tip-sample distance* d_0 (orange line) leads to alternating tunnel currents $I_{\uparrow\uparrow}$ and $I_{\uparrow\downarrow}$.

polarized STM [26]. Under the assumption of a constant spin-up and spin-down tip DOS ($n_{\uparrow,\downarrow}(E) = const.$) the tunnel current I is derived to be:

$$I(\vec{r}_0, U, \theta) = I_0(\vec{r}_0, U) + I_{SP}(\vec{r}_0, U, \theta) \propto n_t \tilde{n}_s(\vec{r}_0, U) + \vec{m}_t \tilde{\vec{m}}_s(\vec{r}_0, U) \quad . \tag{2.21}$$

The tunnel current can be divided into an unpolarized part I_0 and a spin-polarized contribution I_{SP}. The unpolarized current can be expressed by the non-spin-polarized LDOS of the tip n_t and the energy-*integrated* LDOS of the sample, $\tilde{n}_s(\vec{r}_0, U) = \int_{E_F}^{eU} n_s(\vec{r}_0, E)dE$. The spin-polarized current is proportional to the vector of the spin-polarized tip LDOS, $\vec{m}_t = (n_\uparrow - n_\downarrow)\vec{e}_t$ with $\vec{e}_t$ as magnetization axis of the tip, and the corresponding energy-*integrated* spin-polarized LDOS of the sample, $\tilde{\vec{m}}_s(\vec{r}_0, U) = \int_{E_F}^{eU} \vec{m}_s(\vec{r}_0, E)dE$. For a non spin-polarized case, the second term vanishes and the equation reduces to the result of the original Tersoff-Hamann model.

Thus, the unpolarized part of the tunnel current depends on the integrated sample LDOS at the position of the tip $\tilde{n}_s$, and the polarized part on the projection of the integrated spin-polarized LDOS of the sample $\tilde{\vec{m}}_s$ on the direction of the tip magnetization. Whereas $\tilde{n}_s$, and therefore I_0, always increases with bias voltage, $\tilde{\vec{m}}_s$ and I_{SP} can remain constant, or even decrease and vanish. Thus, constant current images might provide no or only small magnetic contrast. An alternative way to image different magnetic configurations is to record maps of differential conductance $\mathrm{d}I/\mathrm{d}U$:

$$\frac{\mathrm{d}I}{\mathrm{d}U}(\vec{r}_0, U) \propto n_t n_s(\vec{r}_0, U) + \vec{m}_t \vec{m}_s(\vec{r}_0, U) \quad . \tag{2.22}$$

A comparison of Equation (2.21) with Equation (2.22) reveals that the former energy-integrated LDOS of the sample enters now directly: The differential conductance is proportional to n_s and $\vec{m}_s$ at the energy $E_F + eU$. Choosing U in the experiment such as to maximize $\vec{m}_t\vec{m}_s$ results in reasonable magnetic contrast in the signal of differential conductance. A recent overview on the topic of spin-polarized STM can be found in [27].

2.5 Experimental realization

In most STM experiments, the probe tip scans a surface at constant current. The tunnel current was shown in the last sections to depend exponentially on the tip-sample distance. Hence, a crucial part in the experimental realization is the control of the tip position above the sample surface: The tip-sample distance must be controlled to a high precision, as well as the lateral tip position in x and y direction. This is realized by mounting the tip in a piezoelectric tube scanner, or *piezo tube*.

The piezoelectric effect was first observed 1880 by Pierre and Jacques Curie, who discovered the generation of electric charge that resulted from applying stress to a quartz plate. The inverse piezoelectric effect, a deformation of the quartz plate due to voltage application, was confirmed two years later. In 1986, Binnig and Smith invented the piezoelectric tube scanner utilizing this inverse effect [28]. A tube made of piezoelectric material is metalized outside and inside, with the coating outside divided into four sections. Two opposing electrodes are connected to the x voltage, the other two to the y voltage, and the inner part to z voltage. If a voltage between the outer x electrodes is applied, one electrode experiences a positive stress (pressure) and elongates, while the respectively other one experiences a negative stress (tension) and contracts, depending on the polarity. As a result the tube is bent along the x direction. The same holds for the y direction, whereas a z elongation or contraction is achieved by biasing the inner versus the outer electrodes.

Figure 2.7 shows the basic setup to perform STM topography measurements in the constant current mode. A bias voltage U between tip and sample is applied and the tip-sample distance lowered until a tunnel current I begins to flow. The tip is mounted on a piezoelectric tube scanner (yellow) for a precise positioning. The lateral tip site is altered by a raster scan generator biasing the outer tube scanner electrodes. A feedback loop keeps the tunnel current I constant by adjusting the vertical tip position. For a chemically homogeneous sample, the tip sample distance, here notated as Δz, is constant, and the tip movement follows the surface topography. A computer records for each scan line the horizontal and

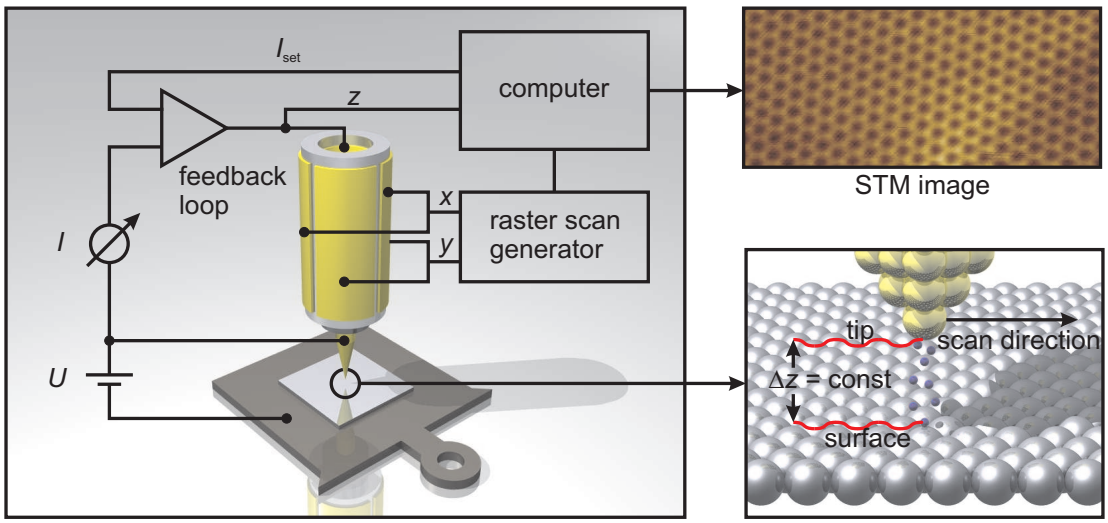

Figure 2.7: Scanning tunneling microscopy in the constant current mode. For a measurement mapping the sample surface, the tip is moved by the raster scan generator of the measurement control system laterally over the surface, while the tip-sample distance z is regulated by a feedback loop keeping the tunnel current constant at a chosen value. Mapping the change in z height as a function of x and y reveals the so-called "topography" images, areas of constant sample LDOS.

vertical tip movement and assembles the tip height information as a function of the lateral tip position to a color-coded topography image of the surface.

The piezo tube usually has a z range well below a micrometer. Thus, an additional position mechanism is necessary for the coarse approach between tip and sample. To implement this approach the piezo tube scanner is integrated into a sapphire prism that can be driven by a piezoelectrical step motor towards the sample, or away from it. Six shear piezos are glued on the inside of the microscope's body, holding the sapphire prism. A so-called stick-slip motion is achieved when an asymmetric saw-tooth voltage is applied to the piezos: during the slow voltage slope the piezos shear slowly and the prism follows the motion (*stick*). On the steep voltage slope the piezos relax too fast for the prism to follow with its inertial mass, and the piezos *slip* along it's surface. The frequency and amplitude of the saw-tooth voltage determines travel time and step size. In our experimental setup the voltage ramps are repeated at a frequency of 0.5 to 1 kHz with a total travel way of 20 mm. Apart from a coarse approach this long travel way allows for a fast in-situ exchange mechanism of the probe tip (see chapter 4).

Chapter 3

The theory of spin torque magnetization switching

A spin-polarized current can transfer a spin angular momentum to a ferromagnet and reverse the magnetization orientation by the exerted spin-transfer torque. The discovery of the spin-transfer effect in magnetic multilayer structures, first treated theoretically 1996 by Berger and Slonczewski [5, 6], lead to a variety of experiments [29–31] and technical applications like the development of spin-torque switched magnetic tunnel junctions for MRAM devices [11].
This chapter is dedicated to the theoretical background of spin-transfer torque, also called spin torque (ST) magnetization switching. We will start with a summary of the physical idea behind the spin-transfer effect. This concept will then be applied to magnetic multilayer structures before presenting the results of Slonczewski's pioneering theoretical treatment of spin-transfer torques in magnetic tunnel junctions. In the last section the phenomenologic Landau-Lifshitz equation will be introduced and augmented to examine the effect of a spin-polarized current on the magnetization dynamics of a macro-spin.

3.1 The spin-transfer effect

This section will summarize the physical idea of the spin-transfer effect. For a detailed quantum-mechanical treatment please refer to the work of Luc Berger [5], or Stiles and Zangwill [32].
Consider a spin-polarized current I impinging perpendicularly on a thin ferromagnetic layer along the $y-z$ plane (see Fig. 3.1). The layer is magnetized along $+z$ direction, and the current is polarized at an angle θ to the layer moments. The wave function of the incoming electrons can then be described by a superposition of basis states with spins in $+z$ direction $(+)$ and spins in $-z$ direction $(-)$. At the interface of the magnetic layer, the electrons will be either reflected or transmitted. Calculating the scattered states by solving the Schroedinger equation separately

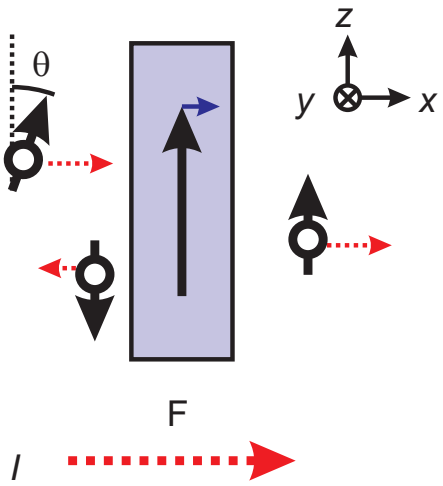

Figure 3.1: Spin torque generation by spin transfer. A spin-polarized current impinges perpendicularly on a thin ferromagnetic layer F magnetized along $+z$ direction. The current is polarized at an angle θ to the layer moments. For F being a perfect spin filter, the spins aligned parallel with the layers magnetization are completely transmitted and those aligned antiparallel are reflected. The component perpendicular to the layer moments is absorbed and generates an effective torque $\propto \sin\theta$ on the layer (blue arrow).

for spin-up and spin-down components, one finds that the transmitted + and − components do not propagate with the same wave vector $\vec{k}$ due to band splitting inside the ferromagnet. Furthermore, the transmission and reflection amplitudes T and R, which are determined by the magnitude of the potential step at the interface, differ for the two spin orientations. The magnet acts as a spin filter. Knowing the spin-dependent transmission $T_{+,-}$ and reflection amplitudes $R_{+,-}$, one can calculate the incoming, reflected and transmitted spin current density. It turns out that the longitudinal spin current is conserved (parallel to the z direction), but the transverse spin current, i.e. perpendicular to the z direction, is not. The latter instead shows a discontinuity that gives rise to a spin torque acting on the magnet.
Assuming the case of the magnet being a perfect spin filter, spins aligned with the layer moments will be completely transmitted ($T_+ = 1$, $R_+ = 0$), while antiparallel spins are completely reflected ($R_- = 1$, $T_- = 0$, see Fig. 3.1). The component of the incident electron flux perpendicular to the magnetization with magnitude $\propto \sin\theta$ will be absorbed in the magnetic layer by exchange interaction of the conducting electrons and the magnetic moments of the layer. The resulting torque Γ is $\propto \sin\theta \cdot I$ and attempts to align the moments of the layer with the polarization of the incident current. Thus, it can be utilized to revert the magnetization direction of the ferromagnetic layer.

3.2 Spin-transfer torque switching in multilayer structures

A current of unpolarized electrons generates no torque from the spin filter effect. Therefore, another ferromagnetic layer is necessary to first polarize the current before it impinges upon the target ferromagnetic layer. Then a spin angular

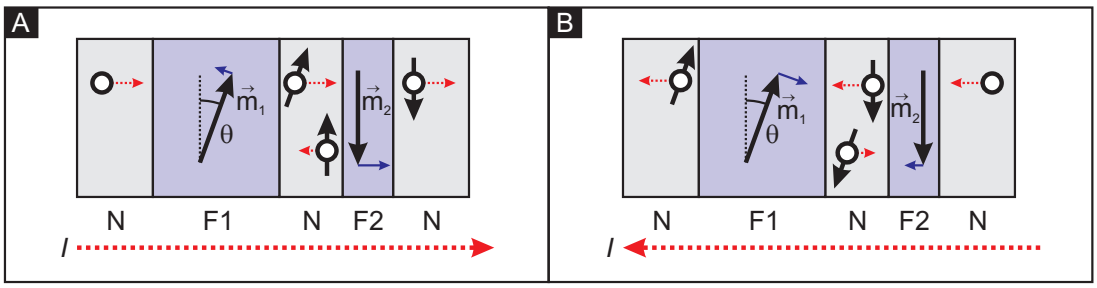

Figure 3.2: Principle of spin transfer torque switching in a ferromagnet- normal metal - ferromagnet (F-N-F) junction. F1 and F2 are magnetized along $\vec{m}_1$ and $\vec{m}_2$, respectively. (**A**) When the electron current is injected from the left, electrons will pass first through F1 and reach F2 polarized along $\vec{m}_1$, tempting to align its magnetic moments parallel to $\vec{m}_1$. F1 experiences a torque, too, by the electrons reflected at the N-F2 interface, but its high anisotropy will prevent magnetization reversal. (**B**) Current reversal: Electrons passing first F2 will impinge on F1 polarized along $\vec{m}_2$. The reflected electrons will exert a torque to align $\vec{m}_2$ antiparallel with respect to $\vec{m}_1$.

momentum is transferred from the first layer to the electron current by polarizing it. Afterwards, the electrons transfer the momentum to the second magnetic layer by exerting a spin-transfer torque. Additionally, the two magnetic layers allow for multiple scattering events of the electrons between them. This is indispensable to achieve magnetization reversal into the antiparallel configuration as will be shown in the following.

Figure 3.2 shows a ferromagnet - normal metal - ferromagnet (F-N-F) junction. The thick ferromagnet (F1) is magnetized along $\vec{m}_1$ and serves as a spin filter, the second ferromagnet (F2) is magnetized along $\vec{m}_2$ and shall be the target of spin torque switching. Both F1 and F2 are contacted by normal metallic leads. An unpolarized current is injected from the left into the trilayer structure (A). The electrons pass first through F1 and are polarized along $\vec{m}_1$. If the normal spacer N is thinner than the spin-diffusion length, the spin-polarization of the current will be preserved when reaching the second layer F2 and the current will exert a torque Γ on the magnetic moment of F2 attempting to align $\vec{m}_2$ with $\vec{m}_1$. In turn, the electrons reflected at the N-F2 interface are aligned antiparallel to $\vec{m}_2$ and therefore exert a torque trying to align $\vec{m}_1$ antiparallel with $\vec{m}_2$ when impinging on F1. Here the different thickness of the two layers comes into play: The high anisotropy of the thick F1 will hold its magnetization orientation along $\vec{m}_1$. In literature this layer is therefore referred to as the *fixed* layer. However, the torque Γ on F2 is of interest here: If it is high enough to overcome the anisotropy forces of F2, it leads to magnetization reversal resulting in parallel alignment of $\vec{m}_2$ and $\vec{m}_1$.

If the current is reversed, the direction of spin torque is reversed, too (Fig. 3.2 (B)). The electrons pass first through F2 and impinge, polarized along $\vec{m}_2$, on F1. As explained before, the magnetization orientation of F1 will stay fixed. The reflected electrons will, however, be polarized antiparallel to $\vec{m}_1$ and exert a torque

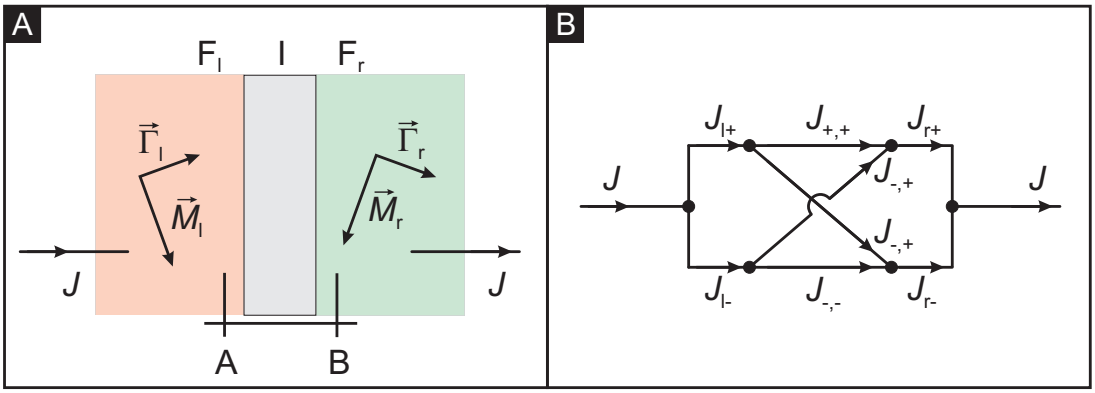

Figure 3.3: (**A**) Magnetic tunnel junction consisting of two ferromagnetic layers $F_{l,r}$ and insulator I. The total current density J flows from the left to the right electrode. (**B**) Equivalent circuit to spin-channel currents.

on F2 to align its magnetic moment antiparallel with respect to $\vec{m}_1$. In conclusion, the current reversal leads to a sign reversal of the exerted torque favoring an antiparallel configuration of $\vec{m}_1$ and $\vec{m}_2$. This asymmetry of the spin transfer torque with respect to the current bias is an important signature distinguishing it from the torques generated by the Oersted field of the electric current.

3.3 Slonczewski's torque in magnetic tunnel junctions

This section will summarize the results of the theoretical work by Slonczewski [33], who examined the torque in magnetic tunnel junctions by applying Bardeen's transfer-Hamiltonian method [22].
Imagine two ferromagnetic films separated by a thin nonmagnetic layer (Fig. 3.3 (A)). The left and right ferromagnetic films $F_{l,r}$ exhibit the magnetizations $\vec{M}_{l,r}$ along the unit vectors $\vec{n}_l$ and $\vec{n}_r$, respectively, enclosing the angle $\theta = \cos^{-1} \vec{n}_r \cdot \vec{n}_l$. The application of an external voltage V leads to an electric current flowing with the density $J = J_0(1 + \iota \cos\theta)$ through this structure. J_0 denotes the unpolarized current, and ι the dimensionless coefficient of magnetoconduction, which is related to the polarization of the two magnetic electrodes. $\vec{J}_{l,\pm} = J_{l,\pm}\vec{n}_l$ denotes the left electric current density in the $\pm$ (up/down) spin-channel flowing through plane A, and $\vec{J}_{r,\pm} = J_{r,\pm}\vec{n}_r$ the right one flowing through plane B. Figure 3.3 (B) shows an equivalent circuit diagram for spin-channel currents. The tunnel current inside the insulating barrier separates into elastic channels with spin conservation ($\vec{J}_{+,+}$ and $\vec{J}_{-,-}$) and inelastic channels ($\vec{J}_{+,-}$ and $\vec{J}_{-,+}$). The conservation of the angular momentum requires that the sum of the interfacial torques $\vec{\Gamma}_{l,r}$ equals the net rate

of spin current flowing into the region bounded by A and B:

$$\vec{\Gamma}_l + \vec{\Gamma}_r = \frac{\hbar}{2e}\left[(J_{l,+} - J_{l,-})\vec{n}_l - (J_{r,+} - J_{r,-})\vec{n}_r\right] \quad , \tag{3.1}$$

where the factor $\frac{\hbar}{2e}$ converts the electric current into one of spin momentum. Adaption of Bardeen's transfer-Hamiltonian method to this spin-dependent case allows the calculation of the spin-channel current density. As a result one finds

$$\vec{\Gamma}_r = \frac{\hbar}{2e} \cdot \tau_r J_0 \vec{n}_r \times (\vec{n}_l \times \vec{n}_r) \quad , \tag{3.2}$$

and

$$\vec{\Gamma}_l = \frac{\hbar}{2e} \cdot \tau_l J_0 \vec{n}_l \times (\vec{n}_r \times \vec{n}_l) \quad , \tag{3.3}$$

or

$$\Gamma_r = -\frac{\hbar}{2e} \cdot \tau_r J_0 \sin(\theta) \quad , \tag{3.4}$$

and

$$\Gamma_l = -\frac{\hbar}{2e} \cdot \tau_l J_0 \sin(\theta) \quad , \tag{3.5}$$

where $\tau_{r,l}$ are dimensionless torque coefficients. If the inter-channel particle currents $\vec{J}_{+,-}$ and $\vec{J}_{-,+}$ are separable into left- and right-dependent factors, the torque coefficient of one electrode τ_i is equal to the tunnel polarization P_j of the other electrode, i.e.

$$\tau_r = P_l \quad \text{and} \quad \tau_l = P_r \quad . \tag{3.6}$$

3.4 Magnetization dynamics in the macro-spin model

The model of a macro-spin is often applied to describe the dynamics of a nanomagnet. The magnetization of a particle is assumed to be homogeneously magnetized and to behave like a single giant magnetic moment, with the total moment given by the sum of the individual magnetic moments of the atoms of the particle. The following theoretical descriptions will follow the overview given in [34].
An electron current I spin-polarized along $\vec{n}_s$ impinging on a macro-spin with magnetization $\vec{m}$ along $\vec{n}_m$ exerts the torque $\vec{\Gamma}_\mathrm{s}$:

$$\vec{\Gamma}_\mathrm{s} = g(\vec{n}_m, \vec{n}_s)\frac{\hbar\eta I}{2e}\vec{n}_m \times (\vec{n}_s \times \vec{n}_m) \quad , \tag{3.7}$$

where $\eta = \frac{I_\uparrow - I_\downarrow}{I_\uparrow + I_\downarrow}$ is the spin-polarization factor of the polarizing magnet given by its majority and minority spin currents $I_\uparrow$ and $I_\downarrow$, and e is the electron charge (see section 3.3, and [6]). The scalar function $g(\vec{n}_m, \vec{n}_s)$ denotes a prefactor that

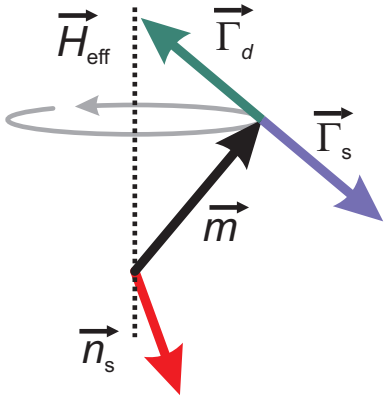

Figure 3.4: Spin transfer torque in the macro-spin model. The magnetization $\vec{m}$ precesses around the effective field $\vec{H}_{\text{eff}}$. An incoming current spin-polarized along $\vec{n}_{\text{s}}$ generates a spin-transfer torque $\vec{\Gamma}_{\text{s}}$ that competes here with the damping torque $\vec{\Gamma}_{\text{d}}$. If the spin torque overcompensates the damping $\Gamma_{\text{s}} > \Gamma_{\text{d}}$ the precession cone angle will increase.

takes into account the angular dependence of the efficiency of the spin-angular momentum transfer. In the following discussion we will assume $g(\vec{n}_m, \vec{n}_s) \equiv 1$, which describes a redirection of the current polarization and total absorption of its transverse angular momentum by the macro-spin.
The phenomenological Landau-Lifshitz (LL) equation [35] can be used to describe the magnetization dynamics of the macro-spin magnetization $\vec{m}$ as

$$\frac{1}{\gamma}\frac{d\vec{m}}{dt} = \vec{m} \times \left[\vec{H}_{\text{eff}} - \frac{\alpha}{m}\vec{m} \times \vec{H}_{\text{eff}}\right] \quad , \tag{3.8}$$

with $\gamma = \frac{g\mu_B}{\hbar}$ as the gyromagnetic ratio and α as the phenomenological LL damping coefficient. $\vec{H}_{\text{eff}}$ includes all magnetic fields acting effectively on the macro-spin, such as an uniaxial anisotropy field $\vec{H}_{\text{K}}$, or an applied external magnetic field $\vec{H}$. The first term in Equation (3.8) is the so-called precession term, which causes the magnetization of the macro-spin to precess around the effective magnetic field. The second term describes a damping of this motion, a torque $\vec{\Gamma}_{\text{d}}$ trying to align $\vec{m}$ with $\vec{H}_{\text{eff}}$. Including the spin-transfer torque of Eq. (3.7) into this equation gives

$$\frac{1}{\gamma}\frac{d\vec{m}}{dt} = \vec{m} \times \left[\vec{H}_{\text{eff}} - \frac{\alpha}{m}\vec{m} \times \left(\vec{H}_{\text{eff}} + \vec{H}_{\text{s}}\right)\right] \quad , \tag{3.9}$$

where the spin torque enters the second addend as an additional field $\vec{H}_{\text{s}}$ along the spin-polarization direction $\vec{n}_s$:

$$\vec{H}_{\text{s}} = \frac{\hbar\eta I}{2em\alpha}\vec{n}_s \quad .$$

Figure 3.4 depicts the resulting dynamics: The magnetization $\vec{m}$ precesses around the effective field $\vec{H}_{\text{eff}}$ (first term in Equation (3.9)). Additionally, damping torque $\vec{\Gamma}_{\text{d}}$ and spin-transfer torque $\vec{\Gamma}_{\text{s}}$ are acting (second term). The damping torque $\vec{\Gamma}_{\text{d}}$ attempts to align $\vec{m}$ with $\vec{H}_{\text{eff}}$. Depending on the polarization direction of the incoming current, the spin torque can assist this damping, or compete with it,

as shown in Fig. 3.4. If the spin torque overcompensates the damping torque $\Gamma_s > \Gamma_d$, the precession cone angle will increase and magnetization reversal becomes possible.

Finite-temperature effects

The effect of finite temperature T on the macro-spin can be described by adding a Langevin random field H_L to the effective field term of the LL equation [36]. The fluctuating random forces due to thermal agitation can be described by

$$H_{L,i} = \sqrt{\frac{2\alpha k_B T}{\gamma m}} \cdot h_{ran,i}(t), \quad i = x, y, z \quad , \tag{3.10}$$

where each component i has its own Gaussian random function $h_{ran}(t)$ that fulfills $\langle h_{ran,i}(t) \rangle = 0$. If only an additional anisotropy field $\vec{H}_K$ is acting, the LL equation reads

$$\frac{1}{\gamma}\frac{d\vec{m}}{dt} = \vec{m} \times \left[\vec{H}_K + \vec{H}_L - \frac{\alpha}{m}\vec{m} \times \vec{H}_K\right] \quad . \tag{3.11}$$

This equation describes the thermally activated dynamics of a macro-spin in a potential well given by the anisotropy field $\vec{H}_K$: The magnetization $\vec{m}$ fluctuates around a minimum, seeing a potential barrier height E_b. Equation (3.11) holds for the case, where $E_b \gg k_B T$. The finite mean lifetime $\bar{\tau}$ of the macro-spin remaining in the potential well then follows the Boltzmann statistics:

$$\bar{\tau} = \tau_0 \exp\left[\frac{E_b}{k_B T}\right] \quad , \tag{3.12}$$

with $\tau_0 \propto (\gamma H_K)^{-1}$ as the reciprocal attempt frequency [36]. Adding the spin-torque term now leads to

$$\frac{1}{\gamma}\frac{d\vec{m}}{dt} = \vec{m} \times \left[\vec{H}_K + \vec{H}_L - \frac{\alpha}{m}\vec{m} \times \left(\vec{H}_K + \vec{H}_s\right)\right] \quad . \tag{3.13}$$

If $\vec{H}_K$ and $\vec{H}_s$ are collinear, $H_K + H_s(I_{crit}) = 0$ describes a stability boundary: If the current I exceeds the critical current

$$I_{crit} = -\frac{2em\alpha}{\hbar\eta} H_K \quad ,$$

a net gain of the precession cone angle results and reversal of the magnetic moment can occur. We can rewrite Eq.(3.13) such that

$$\frac{1}{\gamma}\frac{d\vec{m}}{dt} = \vec{m} \times \left[\vec{H}_K + \vec{H}_L - \frac{\tilde{\alpha}}{m}\vec{m} \times \vec{H}_K\right] \quad , \tag{3.14}$$

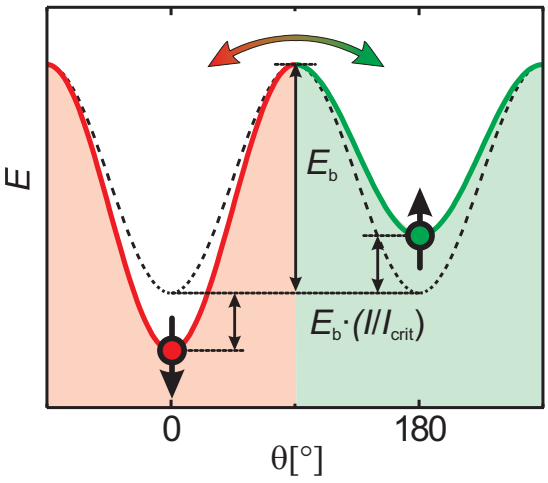

Figure 3.5: Impact of the spin-transfer torque on the macro-spin dynamics in a potential landscape of an uniaxial anisotropy field. In absence of a spin-polarized current, both magnetization states are degenerate (dashed line) and the energy barrier E_b needs to be overcome for magnetization reversal. The spin torque exerted by a polarized current modifies the effective energy barrier for both states by $\pm\frac{I}{I_\mathrm{crit}}E_\mathrm{b}$. Thus one state is favored against the other and the mean lifetime for both states will differ.

where

$$\tilde{\alpha} = \alpha\left(1+\frac{H_\mathrm{s}}{H_\mathrm{K}}\right) = \alpha\left(1-\frac{I}{I_\mathrm{crit}}\right) \quad .$$

This notation makes clear that the spin-transfer torque term modifies the effective damping of the magnet. Beyond the critical current I_crit the effective damping becomes negative: instead of shrinking the precession cone angle, deviations from the equilibrium positions are amplified and magnetization reversal can occur. To maintain the validity of the Langevin random field H_L in Eq.(3.10) when replacing α by $\tilde{\alpha}$, one introduces a fictitious temperature $\tilde{T}$ the macro-spin experiences, such as $\alpha T = \tilde{\alpha}\tilde{T}$. For the mean lifetime $\bar{\tau}$ this leads to [37]

$$\bar{\tau} = \tau_0 \exp\left[\frac{E_\mathrm{b}}{k_\mathrm{B}\tilde{T}}\right] = \tau_0 \exp\left[\frac{E_\mathrm{b}}{k_\mathrm{B}T}\frac{\tilde{\alpha}}{\alpha}\right] \tag{3.15}$$

$$= \tau_0 \exp\left[\frac{E_\mathrm{b}}{k_\mathrm{B}T}\left(1-\frac{I}{I_\mathrm{crit}}\right)\right] \quad . \tag{3.16}$$

Equation (3.16) shows that the spin-transfer excitation of the macro-spin by the spin-polarized current can be regarded as an effective energy barrier modification $E_\mathrm{b} \to E_\mathrm{b}\cdot\left(1-\frac{I}{I_\mathrm{crit}}\right)$. Depending on the current sign, the spin torque will stabilize $(I<0)$ or destabilize $(I>0)$ the magnetization $\vec{m}$ by increasing or decreasing the effective energy barrier by $\pm\frac{I}{I_\mathrm{crit}}E_\mathrm{b}$, respectively.

Chapter 4

Experimental setup and preparation of tip and sample

A scanning tunneling microscope is a compact instrument, usually about the size of a beverage can. However, to perform reproducible measurements on the atomic scale the experimental setup must fulfill high demands. For the experiments presented here, the most important conditions are:

- a high level of cleanliness and purity,
- a maximal thermal stability, and
- variable temperatures.

Normal atmosphere can be excluded as possible experimental environment: surfaces exposed to air are covered within very short time with water and isolating oxide layers making SP-STM experiments unfeasible. To achieve the required condition of high cleanliness, the setup has to allow for preparation and analysis within vacuum. Ultra-high vacuum conditions (UHV) with pressures $p \leq 10^{-9}$ mbar are therefore utilized. A flow cryostat operating with liquid helium allows for temperature control. The following sections will give insight into the experimental setup and the tip and sample preparation methods used for the presented studies.

4.1 The UHV chamber system

To ensure a high degree of cleanliness all experiments are performed in an UHV chamber system based on a commercial system designed by the company Omicron [38]. It consists of four different chambers connected by manually operated UHV valves (Fig. 4.1):

- the load lock,

- the preparation chamber,
- the analysis chamber, and
- the dosing chamber (not used here).

Linear manipulators enable the transfer of tips and samples within the system. Autonomous operation of each chamber is realized by the usage of several vacuum pumps: The load lock can be evacuated independently from the residual system by a membrane and a turbo pump. This small chamber enables tip and sample transfer into and out of the UHV system without breaking system vacuum. The two main chambers, the preparation and analysis chambers, are each equipped with an ion-getter pump and a titanium sublimation pump (TSP) and will be introduced in the following section in more detail.

4.1.1 Preparation chamber

Tip and sample preparations take place within the preparation chamber (Fig. 4.1, top). This part of the system contains a home-built electron beam heater that can achieve temperatures of up to $T = 2400\,\mathrm{K}$ which are required for the cleaning procedure of W(110) (see section 4.3). For heating, the tip or sample holder is positioned on a tungsten wire stage above a tungsten filament that acts as cathode. The wire stage is connected to high voltage ($U_{\mathrm{HV}} \leq 2000\,\mathrm{V}$) and the filament powered by a DC current ($I_{\mathrm{fil}} = 3.1\,\mathrm{A}$): The heated filament emits electrons that are accelerated by the high voltage towards the tip or sample holder. This electron bombardment leads to the desired heating. An infra-red pyrometer is used to check the obtained temperature through a viewport.
For material deposition, the tip and the sample are positioned with a (x,y,z) manipulator in front of water-cooled evaporation guns. The material to be deposited is heated by electron bombardment. Additional heating of the housing is prevented by water-cooled copper shields. This hinders desorption of undesired additional adsorbates which reduce the film quality. The evaporation rates are calibrated by depositing submonolayer amounts of the respective material onto the W(110) surface and evaluating the coverage by STM measurements. Chromium is evaporated at a rate of 9 ML/minute from a crucible, iron at a rate of 1.2 ML/minute from a wire. A valve connected to an oxygen vessel allows for O_2 dosing which is necessary for the tungsten cleaning procedure as will be discussed in section 4.3.

4.1.2 Analysis chamber

The analysis chamber (Fig. 4.1, bottom) contains the core of the apparatus, the variable-temperature (VT) STM, in a satellite chamber. This instrument will be

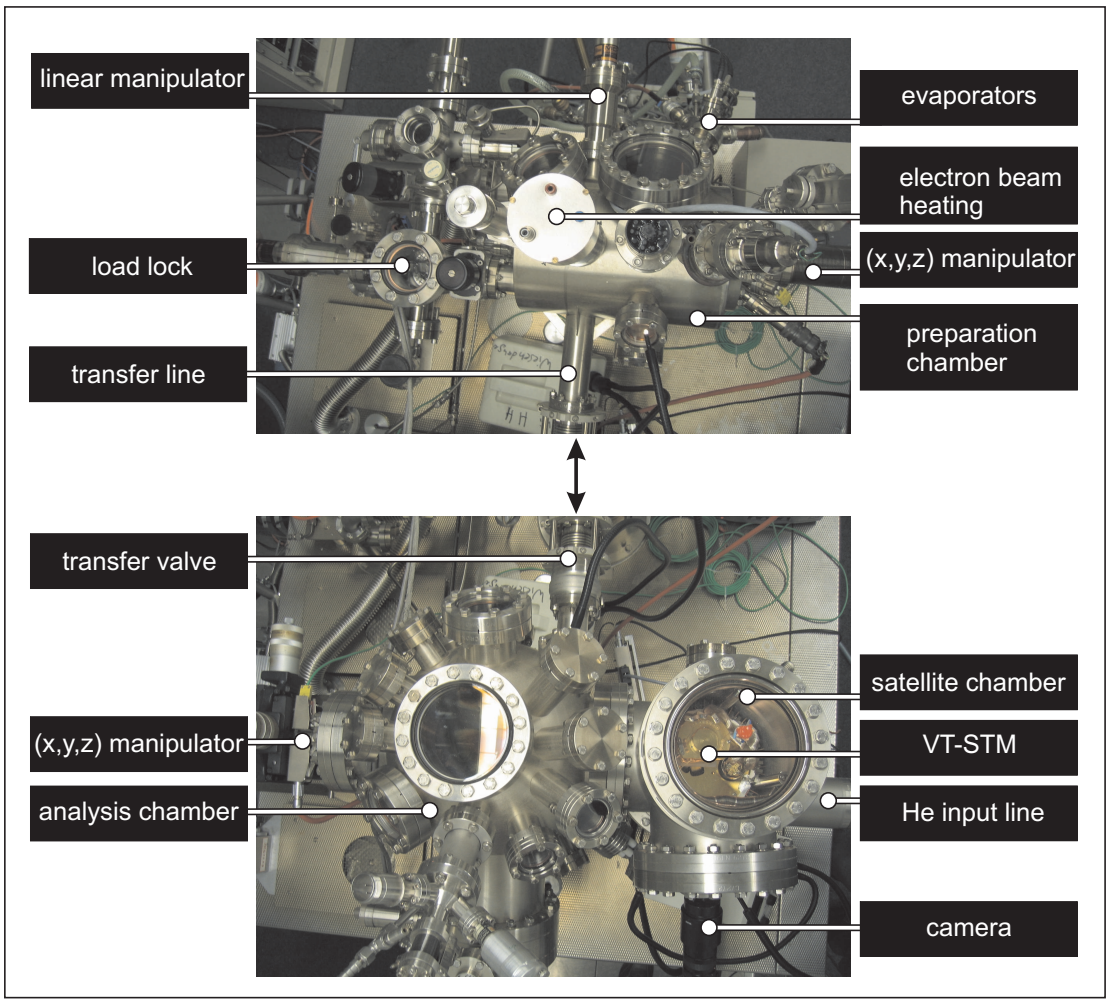

Figure 4.1: Bird's eye view of the chamber system. Top: Preparation chamber for the tip and sample preparation. It is equipped with an electron beam heater to heat samples and tips within the cleaning procedures. Three evaporators allow for covering the cleaned tips and samples with different materials. The considerably smaller load lock chamber enables to transfer tips and samples from and into the chamber system. Bottom: Analysis chamber connected by a transfer valve. It contains a LEED/Auger unit and the VT-STM in a satellite chamber.

introduced in the following section in detail. LEED and Auger setups are also integrated in this chamber for further surface analysis.
A (x,y,z) manipulator is installed to receive the tips and samples coming via a transfer valve from the preparation chamber. The manipulator includes a second resistive heater to enable the annealing of the tip or the sample at lower pressures than in the preparation chamber. The tip and sample holders can be brought from this manipulator by a wobble stick directly into the STM, or left for storage in a carousel.

Since any mechanical vibration has to be avoided during the measurements this chamber is evacuated by pumps without mechanically moving parts: a TSP and an ion-getter pump. The base pressure within this chamber is $\leq 2 \times 10^{-11}$ mbar.

A liquid He flow cryostat manufactured by the company CryoVac is used to achieve variable temperatures for the experiments [39]. Liquid helium is provided by mobile He dewars (100 l or 250 l) that can be attached by a transfer tube to the flow cryostat of the system. An oil-less rotary vane pump behind the cryostat sucks the cooling liquid through the apparatus. The helium flux and therewith the temperature is regulated in first instance by two manually operated mechanical valves within the line. A laminar helium flow is desired since a turbulent flow causes mechanical vibrations and unsteady heat transport. The helium coming from the dewar is lead by a He-line to a heat exchanger mounted near the microscope. Highly flexible copper braids provide the last centimeters of cooling connection from here to the STM. The braids consist of about 800 silver plated copper wires, each of them with a diameter of ≈ 0.05 mm. Their flexibility prevents vibration transmission from the cryostat to the microscope. At the heat exchanger the temperature T_{ex} is measured with a Si-diode. An integrated heater regulated by a PID temperature controller is used to stabilize the temperature. The helium consumption is minimized by regulating the helium flow by the valve setting such as to achieve a temperature only slightly below the desired value. The PID controller then regulates the heating power to achieve the desired temperature.

4.2 The microscope

The microscope is specifically designed to study temperature dependent magnetic phenomena at operation temperatures ranging from 20 to 300 K. In contrast to standard variable-temperature instruments, the whole microscope including the tip is cooled. This has multiple advantages: there is a better energy resolution and a reduced thermal drift between the tip and the sample. Further, an increased range of possible tip coating materials is achieved, since Curie- or Néel-temperatures of magnetic ultra-thin films are often below room temperature. The materials used to build the microscope have been chosen carefully to fulfill a compromise of several requirements and properties, such as UHV compatibility and similar thermal expansion coefficients. A more detailed description on these aspects can be found in the Ph.D. thesis of Thorben Hänke [40].

The instrument is mounted within a shield to protect it from the thermal radiation of the surroundings. To thermally decouple the microscope from its radiation shield, ruby balls are clamped between the microscope and the top of the radiation shield realizing thereby point contacts with minimal thermal transmis-

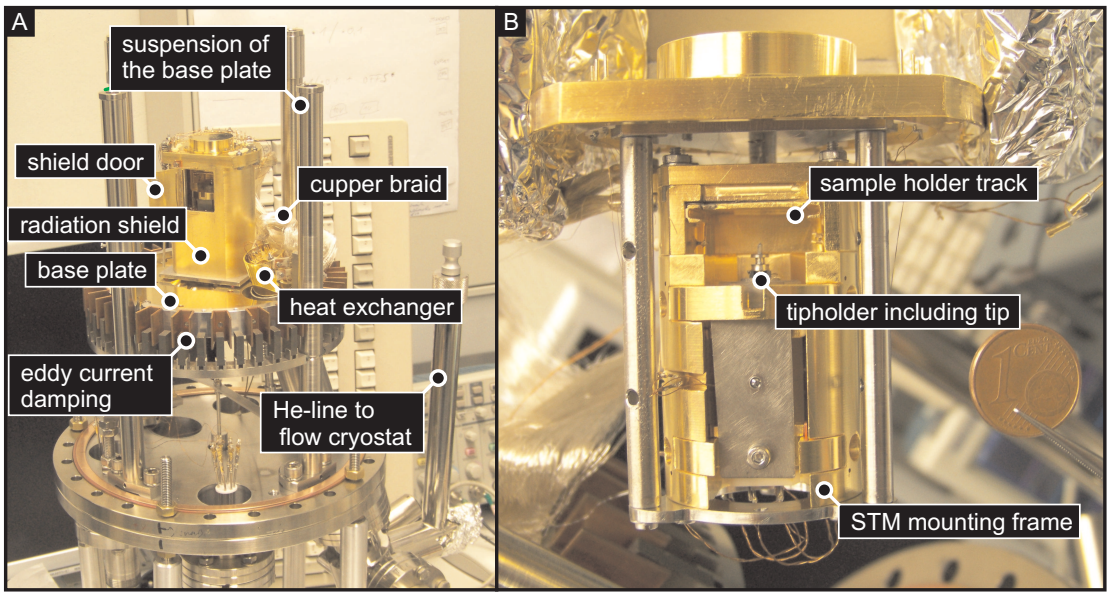

Figure 4.2: (**A**) Base flange and content of the satellite chamber without outer walls. The microscope is mounted on a base plate that is either mechanically fixed for tip and sample exchange or stabilized against mechanical vibrations by metal leads and an eddy current damping. A heat exchanger connects the radiation shield of the microscope with the flow cryostat. A door in the radiation shield allows to exchange tip and samples from the inner laying STM. Ruby balls are used to thermally disconnect the radiation shield from the base plate.
(**B**) The STM outside its radiation shield. The sample holder is mounted above the tip such as the sample is inserted upside down for the measurements. An one euro cent coin gives a notion of the instrument's size.

sion (see Figure 4.3). The copper braids coming from the heat exchanger are fed through small openings in the radiation shield and are screwed to the microscope's body. The radiation shield is cooled additionally via a second copper braid by the flow cryostat exhaust. In this configuration the instrument can be operated at a constant temperature of approximately $T_{STM} \approx T_{ex} + 14\,\mathrm{K}$. The temperature is monitored by an GaAs/GaAlAs diode mounted close to the sample holder on the STM body. When starting a cooling procedure the temperature of the heat exchanger decreases quickly while the microscope's temperature follows with some delay. The STM-body cools down at a rate of approximately 150 K/h and reaches a stable base temperature of $T = 18\,\mathrm{K}$ after about two hours.

For a vibrational isolation the radiation shield is mounted on a massive copper plate (300 mm diameter, 30 mm thickness) that is suspended by four metal springs. During the experiments an eddy current damping decouples the base plate with the instrument from mechanical vibrations of the rest of the setup. The low resonance frequency of this damping system, in combination with the high resonance

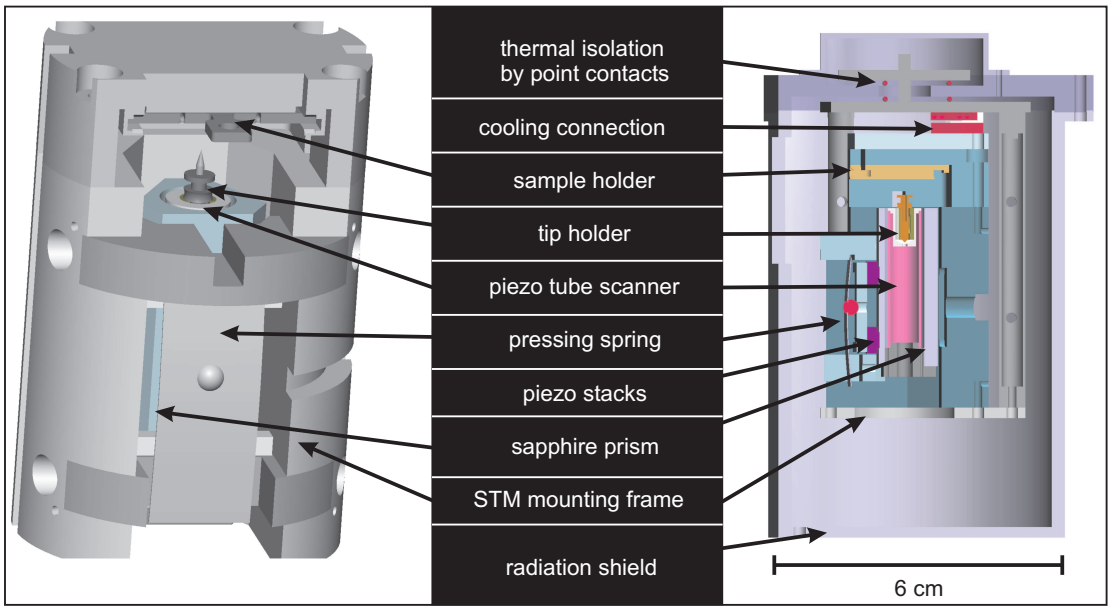

Figure 4.3: Schematic drawing of the STM. View of the microscope from outside (left) and cross sectional view of the instrument in its radiation shield (right). Ruby balls realize point contacts between the microscope's upper plate and the top of the shield for thermal isolation. A cooling connection is responsible for the heat transport to the heat exchanger. The samples are inserted upside down into the sample holder above the tip. The sapphire prism including the tube scanner is hold by a pressing spring within the STM body. Outermost part is the radiation shield.

frequency of the microscope itself, is an effective filter against external, mechanical noise.

A door within the radiation shield allows for a sample and tip exchanging with the wobble stick without breaking vacuum. The *in-situ* tip exchange mechanism is based on a development by Daniel Haude [41]. Since it is an essential part of the tunnel junction, the coarse approach mechanism that moves the tip towards the sample needs to be mechanically stable. Therefore a piezoelectrically driven stepper motor is used. It is built in the walker design and operated in the slip-stick mode (see section 2.5). A first rough approach between sample and tip is done manually by operating the piezoelectrical step motor with a remote control box while observing the decreasing tip-sample distance by means of a camera and a monitor. The final approach into tunnel contact is subsequently performed in an automatic approach mode of the STM control unit.

The microscope is operated by an electronic control unit called Scala manufactured by the Omicron company [38]. A graphical user interface provided by a commercial software on a workstation allows the user to operate the unit for STM measurements. The Scala electronics is connected directly with the microscope to operate the piezoelectric drives and the tube scanner. Additional instruments are used to augment the Scala capabilities to apply high currents and voltages. To achieve tunnel currents above 50 nA (the limit of the original Scala electronics) a commercial current-to-voltage amplifier is utilized [42]. Further, a home-built voltage amplifier is integrated into the setup that allows for bias voltages of up to $U_{bias} = 36\,\mathrm{V}$ for measurements (not used here). The $\mathrm{d}I/\mathrm{d}U$ signal is recorded during the measurements simultaneously with the topography channel using a commercial lock-in amplifier [43]. Therefore, a modulation voltage of $U_{mod} = 40\,\mathrm{mV}$ with a frequency of either $f = 3.333\,\mathrm{kHz}$ or $4.333\,\mathrm{kHz}$ is imposed upon the bias voltage.

4.3 Tip and sample preparation

As mentioned before, a high level of cleanliness is necessary to allow for SP-STM measurements on the atomic scale. This section is dedicated to the preparation of the magnetic tips and samples. To ensure a high purity, most of the preparation is performed *in-situ* as will be explained in the following section.

4.3.1 Tip preparation

An essential requirement for SP-STM measurements is the magnetic probe tip generating a spin-polarized current. Hence the preparation of an electronically and magnetically stable probe tip is a crucial part of the experiment. Several approaches to achieve suitable probe tips have been explored [44]. The currently most common way to produce such a tip is to use magnetic tip material. The STM probe tips are then either:

- directly made from bulk magnetic material [45, 46],
- made from a non-magnetic material (for instance W or PtIr) and subsequently covered by an ultrathin magnetic film [47, 48], or
- made from a non-magnetic material with a magnetic atom or cluster attached on the foremost tip apex [19].

For the experiments presented here the second approach listed, the deposition of a thin magnetic film on a non-magnetic tip, was chosen.

Ex-situ preparation

Starting point of the preparation procedure is the AC-electrochemical etching of a nonmagnetic tungsten tip. A polycrystalline tungsten wire of 0.8 mm diameter is sharpened in a sodium hydroxide solution (8g NaOH per 100 ml H_2O, $U_{\mathrm{etch}} = 5\,\mathrm{V}$). The tip obtained is then clamped into a tip holder and transfered for the subsequent in-situ preparation with a tip shuttle into the UHV chamber system.

In-situ preparation

Before coating the tip with magnetic material, it is flashed with the electron beam heater to a temperature of $T = 1500\,\mathrm{K}$ to remove oxides and any further contaminents left from the etching procedure. This cleaning leads to a better adhesion of the magnetic thin film onto the tip.
The type of magnetic material and the amount deposited onto the tip determines the magnetic sensitivity of the tip [27]. To achieve a magnetic tip with in-plane magnetic sensitivity, several hundred monolayers of chromium are evaporated onto

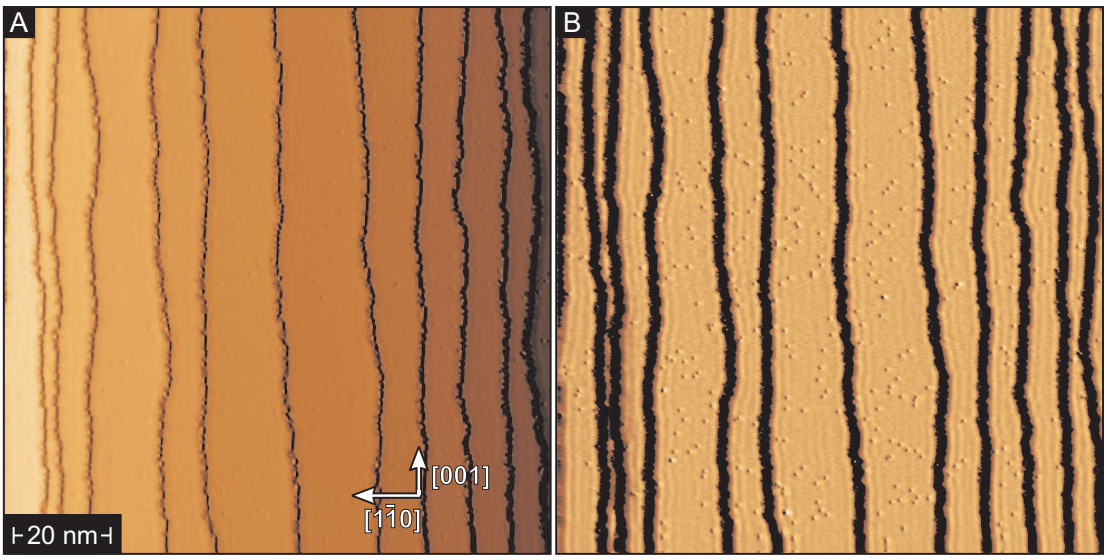

Figure 4.4: (**A**) Topography image and (**B**) dI/dU map of the bare W(110) surface after a cleaning procedure ($I = 2\,\mathrm{nA}$, $U = -200\,\mathrm{mV}$, $T = 45\,\mathrm{K}$).

the tip. Subsequently annealing for $t = 4\,\mathrm{min}$ at $T = 550\,\mathrm{K}$ leads to a stable magnetic film at the tip apex. The absence of a significant stray field due to the antiferromagnetic tip material chosen here avoids unwanted magnetic interactions of tip and sample.

Sometimes tip artifacts such as a diffuse or blurred sample surface appear on the images during the STM measurements due to a blunt tip structure. Then an additional tip preparation is necessary that preferably avoids the removal of the tip from the microscope. To modify the tip while it is in tunnel contact with the sample, short bias voltage pulses of up to 10 Volts can be applied. This leads to a rearrangement of the foremost tip atoms or the deposition of a small amount of tip material onto the sample surface. The new tip apex created can then be used for experiments on a clean sample site [49].

4.3.2 Sample preparation

The W(110) surface is a popular substrate for experiments with epitaxially grown nanostructures and thin films since intermixing is strongly reduced and evaporated metals are easy to remove after the experiment. Tungsten is a transition metal that crystallizes in a body-centered cubic (bcc) structure with a lattice constant of $a = 0.316\,\mathrm{nm}$. Among the pure metals tungsten has the highest melting point of $T_{\mathrm{melt}} = 3695\,\mathrm{K}$ at ambient pressure.

The whole substrate preparation is performed *in-situ* in the preparation chamber at a base pressure of $p \leq 1 \times 10^{-9}$ mbar. The W(110) substrate used in our experiments is cleaned by cycles of annealing in O_2 atmosphere ($T = 1500$ K for 30 minutes) and a subsequent short high temperature flash ($T = 2300$ K)[50]. A clean surface is achieved by gradually reducing the oxygen partial pressure from $p_{O_2} = 2 \times 10^{-6}$ mbar in the first annealing cycle to $p_{O_2} = 4 \times 10^{-8}$ mbar in the last cycle. During this annealing, carbon, the main impurity in tungsten, segregates inside the crystal to the surface. It reacts with the oxygen on the surface, forms CO and CO_2 and desorbs leaving a carbon depletion zone below the surface. The simultaneously oxidized tungsten surface is then cleaned by thermal desorption during the high temperature flash.

These oxygen annealing cycles are only necessary from time to time. Once the W crystal underwent this thorough cleaning procedure, high temperature flashs are for a time sufficient to remove the iron deposited for the experiments. However, over the time impurities coming from the experimental environment and segregating from the deeper crystal layers slowly accumulate again on the sample surface. Then, after 10 to 20 single-flash surface treatments, the crystal has to pass again multiple cycles of oxygen annealing.

Figure 4.4 shows STM overview images of a bare W(110) surface after a cleaning procedure. The topography image shows several tungsten terraces separated by monatomic step edges running along the [001] direction (A). Residual impurities are more apparent in the $\mathrm{d}I/\mathrm{d}U$ map (B). Approximately $N = 300$ adatoms can be identified on the tungsten surface. This is a small value in comparison with the number of W atoms forming this surface area ($N_W \approx 1.7 \cdot 10^5$). The impurity density is thus below 0.2 %. The $\mathrm{d}I/\mathrm{d}U$ map additionally reveals a spatial modulation of the local density of states at the step edges. This interference pattern appears only on a clean W(110) surface with a defect densities below 1% and originates from the reflection of electronic states at the step edges. A combined work of tunneling spectroscopy measurements and density functional theory calculations reveals that a downwards dispersing surface resonance of p_z-d_{xz}-type character is responsible for this observation [50].

Chapter 5

The sample system - Fe/W(110)

The detailed understanding of magnetism in reduced dimensions is a very active field in solid-state research. Today's preparational techniques allow the formation of nanostructures that show considerably different magnetic properties than their respective bulk counterparts.
In the research field of surfaces and thin films, the choice of the substrate and growth conditions are the main parameters to determine the properties of the resulting structure. The system of Fe on W(110) has therefore been subject of many experimental and theoretical studies in the past. Its easy preparation and rich variety of structural, electronic and magnetic properties make it a very popular sample system for SP-STM studies in particular. This chapter will give an overview of the knowledge about the growth and the magnetism of iron on tungsten so far, and focuses in the end on the structures under investigation: Fe monolayer islands on the W(110) surface.

Growth

Bulk iron and tungsten both exhibit a bcc crystal structure with lattice constants $a_{Fe} = 2.8665\,\text{Å}$ and $a_W = 3.165\,\text{Å}$, respectively, as sketched in Fig. 5.1(A). The lattice mismatch of $\frac{a_W - a_{Fe}}{a_W} = 9.4\,\%$ leads to a high strain at low coverages and essentially determines the growth of the first atomic layers of iron on tungsten. The first monolayer (ML) grows pseudomorphically on W(110), i.e. following the underlying tungsten lattice structure. The growth mode is thereby determined by the temperature during or after deposition: At room temperature iron grows as monolayer islands and as step edge decoration on the tungsten terraces. Coalescence is inhibited up to a coverage of nominally $\theta \approx 0.6\,\text{ML}$ presumably caused by the large lattice mismatch [51]. At higher coverages narrow bridges between the islands start to grow until a closed monolayer film is achieved at $\theta = 1\,\text{ML}$ [51]. At elevated temperatures, the growth of the first monolayer changes to a step-flow growth mode. Due to the enhanced surface mobility iron stripes develop along

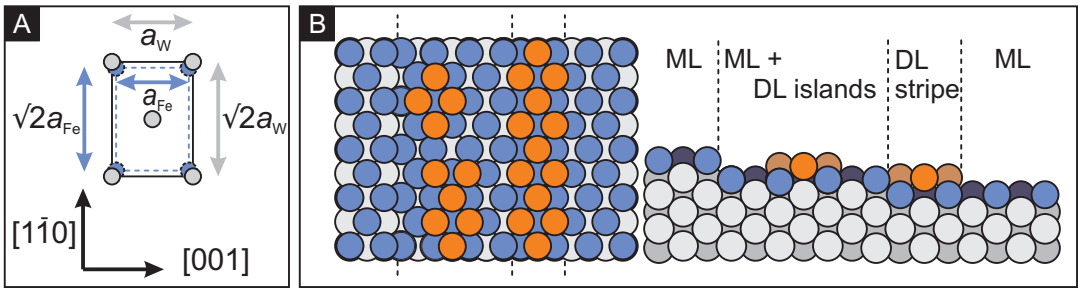

Figure 5.1: The system Fe on W(110) (**A**) Bulk lattice mismatch between the iron (blue) and the tungsten (110) surface (gray). The iron bulk exhibits a smaller lattice constant than tungsten, thus the pseudomorphic growth of the iron monolayer on a W(110) surface leads to a strained film. (**B**) Birds eye and cross sectional view on three terraces of Fe/W(110) at a coverage above one monolayer. Dependent on the substrate temperature the second layer (DL, orange) grows in form of islands, or as stripes along the terrace steps.

the step edges of the substrate [52]. For steps oriented along the [001] direction, smooth monolayer stripes evolve [53]. In contrast, for terrace edges oriented along [1$\bar{1}$0] the preferred growth along the [001] direction leads to the formation of irregular, frayed stripe rims. A wetting layer behavior, i.e. a completion of the first monolayer before the second starts to grow, is observed independent of the temperature. It is caused by the high free surface energy of tungsten ($\gamma_W = 2.9\,\mathrm{J/m^2}$) with respect to the surface energy of iron ($\gamma_{Fe} = 2.0\,\mathrm{J/m^2}$) [54]. The first Fe monolayer is stable up to a temperature of $T = 1100\,\mathrm{K}$ where the iron desorption from the tungsten surface begins [55].

A similar temperature dependent growth behavior is observed for the second monolayer of iron on W(110): At room temperature an island growth is found [56], whereas step-flow growth occurs at elevated temperatures ($T \approx 500\,\mathrm{K}$ [57]). For a visualization, both configurations are shown in Fig.5.1(B). The doublelayer (DL) additionally exhibits occasional dislocation lines along the [001] direction: the assembly of additional iron atoms allows for a relaxation of the iron film along the [1$\bar{1}$0] direction [52]. The following layers release the substrate induced stress further by forming dislocation lines along different crystallographic directions until the original Fe lattice constant is reached at higher coverages [52, 58]. An increased temperature leads, at higher coverages, to the formation of three-dimensional iron islands on top of the wetting monolayer that allows for a better lateral relaxation than the formation of a film [59, 60]. A more detailed discussion of the different growth modes of Fe on W(110) can be found in [24].

Magnetism

The iron monolayer was found to exhibit an in-plane surface anisotropy with an easy-axis along the $[1\bar{1}0]$ direction by *in situ* conversion electron Mössbauer spectroscopy (CEMS) and by spin-polarized low-energy electron diffraction (SPLEED) [61, 62]. A combined STM and SPLEED investigation of the monolayer magnetism of Fe on W(110) revealed a Curie temperature of $T_C \approx 225\,\mathrm{K}$ for the monolayer [51].
In the sub-monolayer regime, widely spaced iron stripes were found to be ferromagnetic down to a coverage of $\theta \approx 0.05\,\mathrm{ML}$. The Curie temperature T_C was shown to decrease with the coverage θ (and therefore with the finite iron stripe width W) to $T_C \approx 180\,\mathrm{K}$ near $\theta = 0.1\,\mathrm{ML}$. Interestingly, samples prepared at room temperature leading thus to the island growth mechanism show no magnetic order in the SPLEED measurements for coverages below $\theta = 0.58\,\mathrm{ML}$ and temperatures $T \geq 115\,\mathrm{K}$: The islands were determined to be superparamagnetic [51]. One striking phenomenon was the appearance of a sudden magnetic percolation at slightly higher coverages: "the steep rise in a narrow θ interval of only 2% from a completely nonmagnetic state at $\theta = 0.58$ (ML) to a magnetic state at $\theta = 0.60$ (ML)"[51] with a Curie temperature close to the extended monolayer value ($T_C(\theta \geq 0.60) \geq 190\,\mathrm{K}$). Obviously, the percolation is triggered by the coalescence occuring at $\theta \approx 0.6\,\mathrm{ML}$ where thermally switching islands merge to bigger, thermally stable structures.
A combined STM, Kerr magnetometry and Monte Carlo study on narrowly spaced monolayer iron stripes revealed dipolar interstripe coupling between adjacent stripes [53]. Iron stripes with widths W from 20 to 32 atomic rows were grown on a vicinal W(110) substrate with an average terrace width of $(9.1 \pm 0.6)\,\mathrm{nm}$, corresponding to approximately 40 atomic tungsten rows. Each iron stripe was found subdivided by domain walls into blocks of full stripe width with alternating sign of magnetization driven by exchange interactions. Dipolar interstripe coupling between adjacent stripes then occurred due to the magnetic easy anisotropy axis being in-plane but across the stripes.
In a further study the susceptibility of iron nanostripes on W(110) was investigated by Kerr magnetometry as a function of the temperature [63]. From the results obtained the domain wall energy e_{dw} per atomic row was found to be almost constant $\frac{e_{\mathrm{dw}}}{W} = (15.2 \pm 1.4)\,\mathrm{meV}$ for different stripe widths W. Additionally the domain wall width for the monolayer stripes was determined in SP-STM measurements to $w_{ML} = (0.6 \pm 0.2)\,\mathrm{nm}$. The combination of these results allowed the calculation of the exchange stiffness A and the anisotropy K for this system. The authors found $A = (3.6^{+2.2}_{-1.4}) \times 10^{-12}\,\mathrm{J/m}$ and $K = (40.6^{+26}_{-15}) \times 10^{6}\,\mathrm{J/m^3}$ (note that the values calculated in [63] are corrected in [64]).

For the second monolayer Fe on W(110) the easy axis magnetization direction is out-of-plane. Only small double layer (DL) islands below $2-3\,\mathrm{nm}$ in width are exchange coupled to the in-plane magnetized monolayer [56]. Bigger islands and stripes show a preferred magnetization direction perpendicular to the surface [56, 65, 66]. Narrow stripes therefore exhibit long out-of-plane domains that order stripewise antiparallel, i.e. adjacent stripes are magnetized alternately up and down by dipolar inter-stripe coupling [67]. In wider DL stripes, on the other hand, the magnetization was found to periodically change *within* the single stripes by introducing several domain walls [66]. The evolving magnetic pattern show in SP-STM measurements a unique sense of inhomogeneous rotation along the [001] direction. The rotational sense of this spin spiral and its type (helical or cycloidal, i.e. including Bloch- or Néel-type domain walls) remained open for a long time, since the azimuthal component of the tip magnetization was unknown in the respective SP-STM experiments. Only very recent SP-STM experiments with a triple axis vector magnet that allows the user to ascertain the probe tip magnetization in three-dimensional space could reveal the detailed structure [68]: a right rotating cycloidal spin spiral. From the comparison of the experimental results with micromagnetic and Monte Carlo simulations this spin spiral ground state was found to be a consequence of the interplay of dipolar and Dzyaloshinskii-Moriya interactions.

At higher coverages of iron on tungsten the easy axis magnetization direction turns again in the $[1\bar{1}0]$ in-plane direction. Finally, at a coverage of $\theta = 22\,\mathrm{ML}$ the easy axis performs another reorientation into the [001] direction [69]. The three-dimensional iron islands on top of the wetting monolayer exhibit either a single domain state or a magnetic vortex structure dependent on their size and shape [70].

Monolayer nanoislands Fe/W(110)

As mentioned before, the evaporation of iron on W(110) at room temperature leads to a self-organized island growth mechanism. Figure 5.2 shows SP-STM images of Fe/W(110) for a coverage of nominal $\theta = 0.14\,\mathrm{ML}$ measured in the constant current mode. The topography image shows a flat tungsten terrace decorated by several well separated iron islands of different size and shape (A). From the recorded line sections one finds that all islands exhibit the same monolayer height. The compact structures are about 2 to 7 nm in diameter corresponding to compositions of 40 to 150 iron atoms. In the simultaneously recorded magnetic $\mathrm{d}I/\mathrm{d}U$ map, each nanoisland exhibits a homogeneous $\mathrm{d}I/\mathrm{d}U$ signal. Obviously the islands are monodomain structures due to their small size. Further, a twofold magnetic contrast on the nanoislands can be observed (B). Some islands appear bright in the Figure while others appear dark. The two distinct contrast lev-

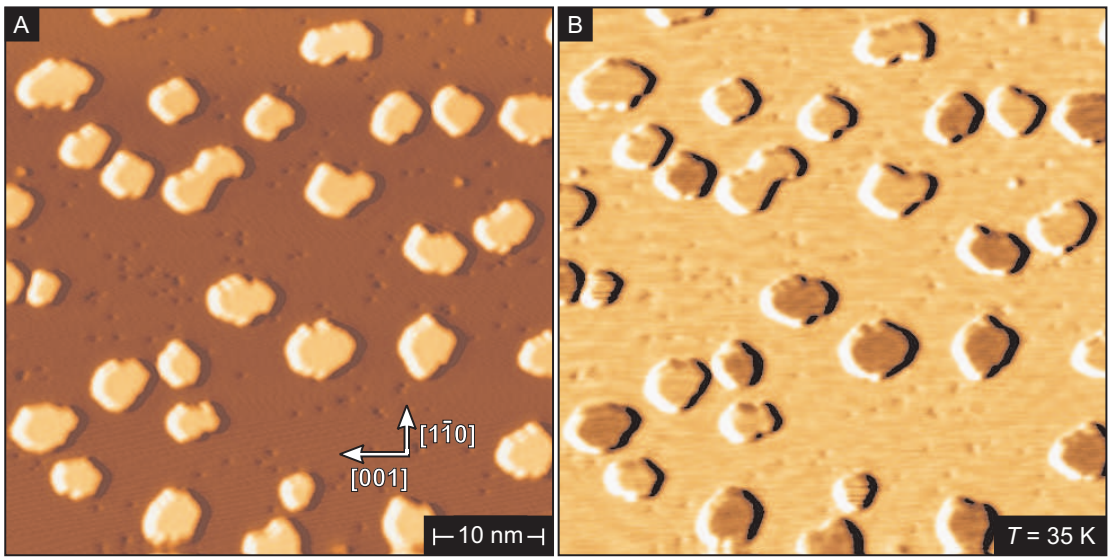

Figure 5.2: SP-STM images of Fe on W(110): (**A**) Topography image of a tungsten terrace decorated by iron islands. The preparation at room temperature leads to the growth of islands of one atomic height. Clearly spaced and mostly compact structures with a few nanometer in diameter can be recognized ($I = 2\,\mathrm{nA}$, $U = -150\,\mathrm{mV}$). (**B**) Corresponding magnetic $\mathrm{d}I/\mathrm{d}U$ map. At a temperature of $T = 35\,\mathrm{K}$ the nanoislands appear either dark or bright reflecting monodomain structures that are magnetized parallel or antiparallel with respect to the tip magnetization.

els reflect an additional magnetic property of this system: As mentioned before, the iron monolayer is a ferromagnetic and uniaxial system. Thus, the two distinct magnetic contrast levels refer to the two possible magnetization states of the nanoislands along the [1$\bar{1}$0] direction. The projection of the tip magnetization on the island magnetization is either parallel or antiparallel leading to different signals of differential conductance for the two configurations. Overview images reveal a random and balanced distribution of the two magnetization directions. Hence, the total net magnetization of the sample equals zero.
These measurements were performed at a temperature of $T = 35\,\mathrm{K}$. The consequence of an elevated temperature on this system will be the subject of the next chapter.

Chapter 6

Thermal switching behavior of nanoislands

The phenomenon of thermally activated barrier crossing has been known for a long time in many fields of physics and chemistry, as, for instance, diffusion theory and chemical kinetics. Approximately 60 years ago, Néel and Brown performed the first theoretical approaches to describe the thermally activated magnetization reversal of mono-domain particles with uniaxial anisotropy [36, 71]. The mean lifetime $\bar{\tau}$ between consecutive switching events of a particle is characterized by the thermal energy $E_{\mathrm{therm}} = k_{\mathrm{B}}T$, and an energy barrier E_{b} that has to be overcome for magnetization reversal:

$$\bar{\tau}(T) = \nu_0^{-1} \exp\left[\frac{E_{\mathrm{b}}}{k_{\mathrm{B}}T}\right] \quad . \tag{6.1}$$

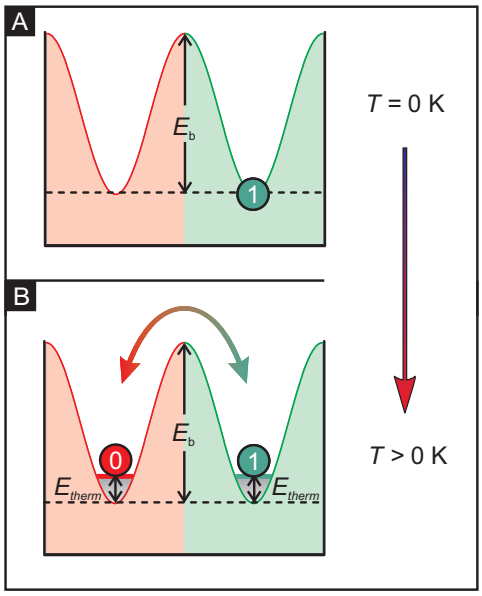

Figure 6.1: Simplified picture of thermally induced magnetization switching in an uniaxial system.
(**A**) At $T = 0\,\mathrm{K}$ the magnetization is in one of its two degenerate magnetization states (here state "1"). An energy barrier E_{b} hinders magnetization reversal.
(**B**) If the thermal energy $E_{\mathrm{therm}} = k_{\mathrm{B}}T$ is increased, the effective energy barrier is decreased and magnetization reversal becomes possible. The attempt frequency ν_0 and the ratio $\frac{E_{\mathrm{b}}}{E_{\mathrm{therm}}}$ determine the mean lifetime $\bar{\tau}$ in an Arrhenius-like dependency.

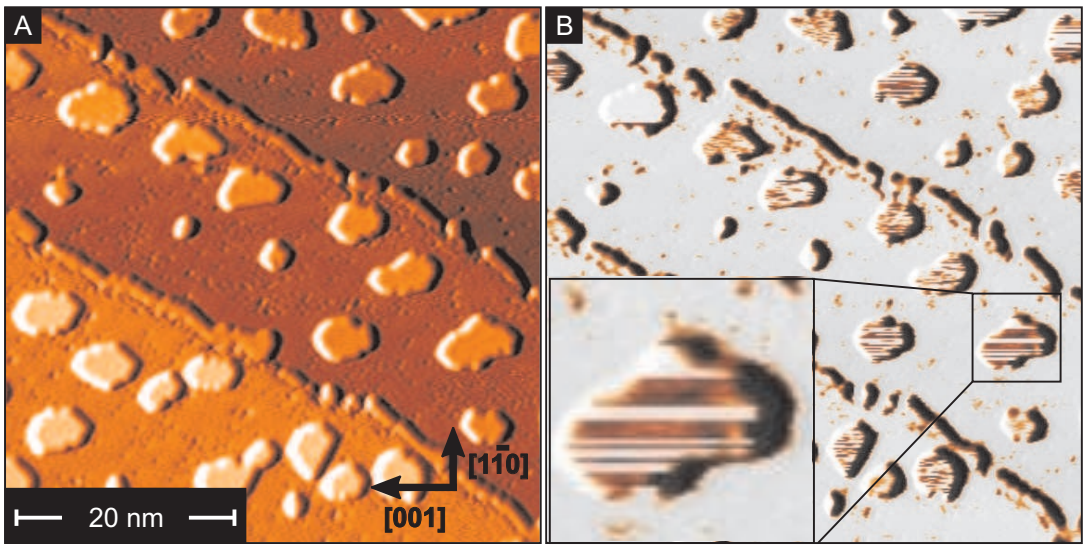

Figure 6.2: (**A**) Topography and (**B**) magnetic $\mathrm{d}I/\mathrm{d}U$ map of Fe ML islands on a W(110) substrate ($T = 56\,\mathrm{K}$, $I = 2\,\mathrm{nA}$, $U = -200\,\mathrm{mV}$). The nanoislands appear striped in the map of differential conductance because their magnetization direction is switching frequently during the scanning procedure (see inset).

Brown designates the attempt frequency ν_0 as the response time of a magnetic single-domain particle to random external forces, which is on the order of the Larmor precession $\nu_0 \approx 10^{-10}\,\mathrm{s}$ [36].

At zero temperature the magnetization is stabilized in one of its two degenerate magnetization states by the energy barrier E_b (see Fig. 6.1), but as the temperature T increases, switching due to thermal agitation will become possible and the switching rate will increase with the thermal energy provided. The energy barrier E_b for magnetization reversal depends on the switching mechanism: Whereas Néel and Brown treated this problem for particles that behave like a single macrospin and switch coherently, i.e. a parallel and collective rotation of all magnetic moments within the particle, magnetization reversal can also be achieved by the nucleation and propagation of a domain wall. Both of these mechanisms have been found experimentally for nanoscale magnetic particles [72, 73].

For a coherent switching the energy barrier is given by the total magnetic anisotropy of the particle

$$E_\mathrm{b} = E_\mathrm{coh} = VK \quad ,$$

V being the particle volume, K the anisotropy energy per unit volume. Since the volume of a circular island of one atomic height scales as $V \propto N_\oslash^2$, where the particle diameter is $N_\oslash$, the energy barrier is expected to scale with the square of the particle diameter, too: $E_\mathrm{b} \propto N_\oslash^2$.

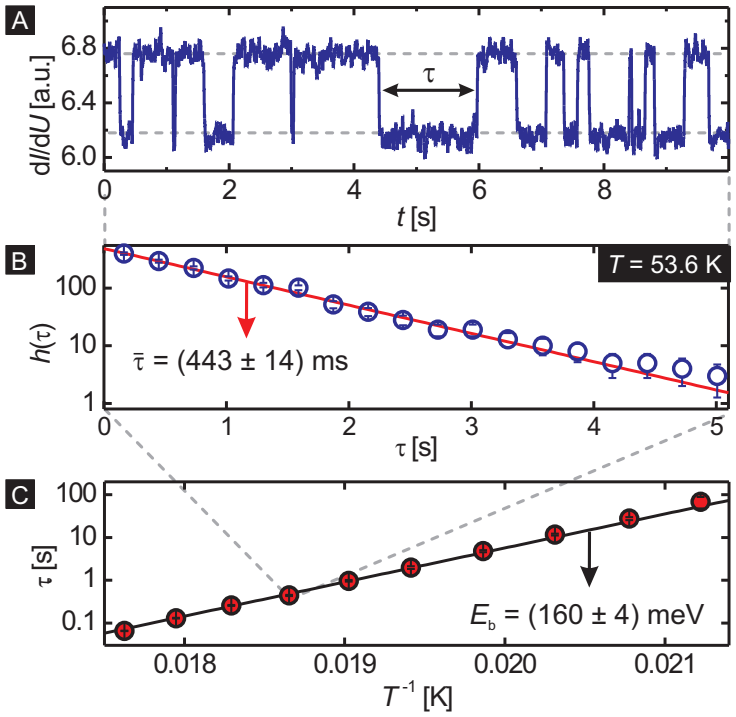

Figure 6.3: Procedure of energy barrier E_b and attempt frequency ν_0 determination. (**A**) The thermally induced magnetization switching is observed by monitoring the telegraphic $\mathrm{d}I/\mathrm{d}U$ signal as a function of time. (**B**) After the evaluation of the lifetimes τ, the results enter a histogram. Fitting with an exponential decay law gives the mean lifetime $\bar{\tau}$ of the magnetization states at the respective temperature. (**C**) Evaluating the mean lifetimes at different temperatures allows to fit an Arrhenius law to determine the energy barrier E_b and the attempt frequency ν_0.

In the case of a domain wall reversal mode the energy barrier scales linearly with the particle diameter $E_\mathrm{b} \propto N_\oslash$ determined by the energy cost of a domain wall

$$E_\mathrm{b} = E_\mathrm{dw} = 4S\sqrt{A \cdot K} \quad ,$$

where $S = N_\oslash(a/\sqrt{2})^2$ denotes the domain wall area with a as lattice constant ($N_\oslash$ given here in numbers of atomic rows (AR)), and A is the exchange stiffness [74]. Equation (6.1) holds in its Arrhenius form for both mechanisms. Many studies focus on the details of the energy barrier E_b and the microscopic processes of magnetization reversal, but the fundamental physics of the prefactor ν_0 is not yet understood: ν_0 is commonly considered to be a constant which only depends on material properties of the system. Size or shape effects have been neglected so far. Figure 6.2 shows a topography and $\mathrm{d}I/\mathrm{d}U$ map of 0.14 ML iron on W(110). Three tungsten terraces are mapped, each of them decorated by iron monolayer nanoislands of different size and shape. At a temperature of $T = 56\,\mathrm{K}$, the islands appear striped in the magnetic $\mathrm{d}I/\mathrm{d}U$ map. Recording multiple $\mathrm{d}I/\mathrm{d}U$ maps on the same site reveals that the stripe patterns are not stable as for static multi-domain structures, but rather reflect a temporal evolution: the magnetization of the islands is switching frequently during the scanning procedure between two states.

To investigate the thermal switching behavior of an individual nanoisland, the magnetic probe tip has been positioned above the center of the chosen island and the evolution of the signal of differential conductance $\mathrm{d}I/\mathrm{d}U$ recorded as function of time. Figure 6.3 (A) shows a section of the signal measured at a fixed

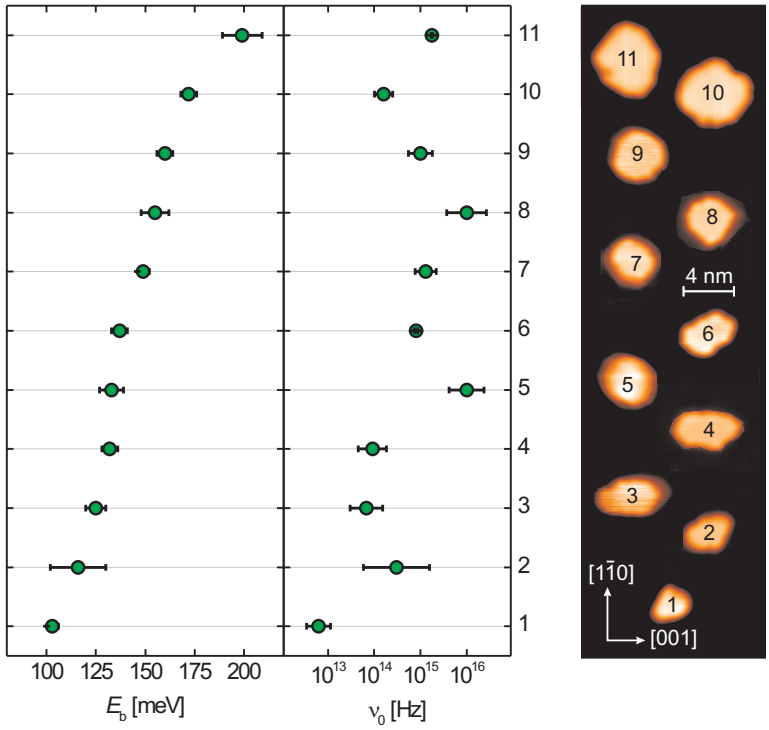

Figure 6.4: Summary of the nanoislands investigated: determined energy barriers E_b and attempt frequencies ν_0 sorted by ascending island size. Whereas E_b shows an overall tendency to increase with island size, ν_0 shows no clear scaling behavior. The patchwork on the right side shows topographic images of the eleven corresponding islands.

temperature. It changes frequently between two distinct levels, according to the magnetization switching of the underlying island that changes between its two magnetization directions along the easy axis. After recording the $\mathrm{d}I/\mathrm{d}U$ signal, the lifetimes τ, i.e. the times between two switching events, were evaluated and collected in a histogram as shown in Fig. 6.3 (B). More than 1000 switching events were recorded for a given temperature to ensure a reliable statistics. Fitting the histogram data with an exponential decay law $h(\tau) \propto \exp(-\frac{\tau}{\bar{\tau}})$ allows then the determination of the mean lifetime $\bar{\tau}(T)$ at the respective temperature T. Repeating this procedure of lifetime determination at different temperatures on the same island allows one to assign an energy barrier E_b and an attempt frequency ν_0 by fitting Eq. (6.1) to $\bar{\tau}(T)$.

6.1 Energy barrier and attempt frequency analysis

The thermal switching behavior of eleven nanoislands has been investigated as a function of temperature. The experiments have been performed at temperatures between $T = 30\,\mathrm{K}$ and $T = 80\,\mathrm{K}$, and each island was observed at two to ten different temperatures. To exclude undesired interactions that may cause devia-

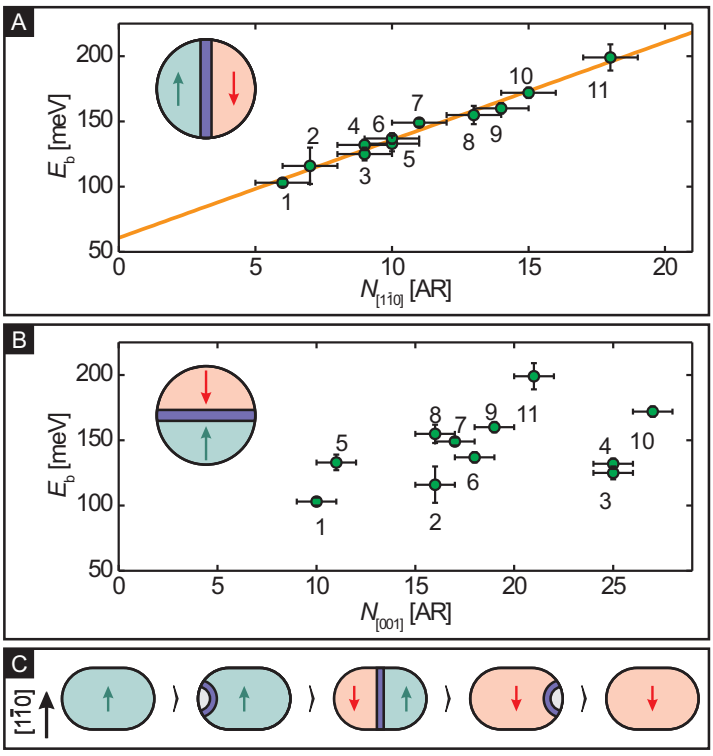

Figure 6.5: Determined energy barrier E_b as a function of island size in $[1\bar{1}0]$ (**A**) and [001] direction (**B**) in numbers of atomic row [AR]. Whereas the former shows a strict linear function, no clear characteristic function can be found regarding the [001] island size.
(**C**) Model of magnetization reversal: Initially the island is in a monodomain state. A domain wall nucleates at one island end and propagates along the [001] direction through the particle. After the domain wall has vanished, the island's magnetization is reversed.

tions from the intrinsic switching behavior, the chosen nanoislands had to fulfill several requirements: The structures had to be clean and compact (as impurities and kinks could influence the reversal mode), and they had to be placed on a spot without other islands or step edges in the proximity to avoid undesired interaction with adjacent structures. A topography patchwork of the nanoislands is shown in Fig. 6.4. The islands of different size and shape are numbered serially according to their respective area size. The figure further shows the corresponding energy barriers and attempt frequencies found. Whereas the determined barriers E_b scale overall with the island size, the attempt frequencies ν_0 show no clear dependence and vary over four orders of magnitude.

To shed light on the question of the reversal mechanism, all islands have been examined in terms of crystallographic dimensions. Figure 6.5 shows E_b as a function of the respective island dimension in $[1\bar{1}0]$ (A) and [001] direction (B). A linear dependence on the particle diameter along $[1\bar{1}0]$ can be seen, whereas for the [001] direction no direct scaling appears. Since E_b is not found to vary quadratically with the particle diameter, a coherent switching mechanism can be excluded. The linear dependence of $E_b(N_{[1\bar{1}0]})$ indicates that the reversal takes place via the nucleation and propagation of a domain wall that aligns along the $[1\bar{1}0]$ direction and moves along the [001] direction. In the first instance no energy offset is expected for this model: A vanishing domain wall length should lead to $E_b(N_{[1\bar{1}0]} = 0) = 0$. But the experimental findings clearly show an offset energy. This additional en-

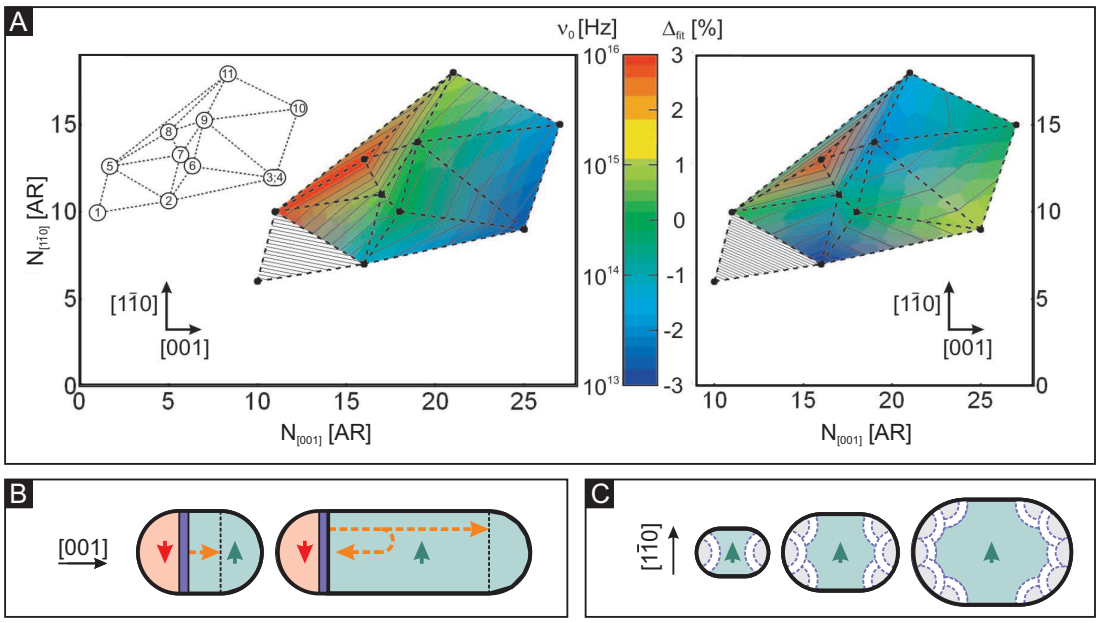

Figure 6.6: (**A**) Color-coded plot of the determined attempt frequencies ν_0 as a function of island dimension in [001] and [1$\bar{1}$0] direction. The mesh in the inset labels the data points with the corresponding island number. The graph on the right shows the relative deviation Δ_{fit} between the data points and the fitted plane. (**B**) The longer the particle size in [001] direction is, the longer is the way the domain wall has to propagate through the particle to achieve a switching event. Thus the switching probability decreases. (**C**) Elongating the particle along [1$\bar{1}$0] increases the number of possible nucleation sites and therewith the switching probability.

ergy can be assigned to the initial reversal of an activation volume.
Figure 6.5 (C) schematically depicts the process of a magnetization reversal: In the initial configuration the island resides in a mono-domain state. Then a domain wall is created at the rim of the island by a coherent magnetization reversal of several magnetic moments within an activation volume, a so-called nucleus or droplet. Then, the wall propagates along [001] direction through the particle. When it annihilates at the other particle end, the magnetization of the whole particle is changed to the reversed orientation. Its length, and therewith its energy cost increase both with particle diameter in [1$\bar{1}$0] direction. A linear fit of the form

$$E_{\text{b}}(N_{[1\bar{1}0]}) = E_0 + e_{\text{dw}} N_{[1\bar{1}0]} \tag{6.2}$$

to the experimental data yields an offset of $E_0 = (61 \pm 5)\,\text{meV}$ related to the nucleation of the domain wall, and a slope of $e_{\text{dw}} = (7.5 \pm 0.4)\,\text{meV/AR}$ giving the domain wall energy per atomic row. In combination with the domain wall width these values will allow the determination of exchange stiffness A and magnetic anisotropy K, as will be shown later.

Figure 6.6 (A) shows the experimentally determined attempt frequencies ν_0 as a function of island diameter N in [001] and $[1\bar{1}0]$ direction. The mesh in the inset allows the correlation of the determined attempt frequency to the corresponding nanoisland no. i. The contour plot with a logarithmic scale reveals that the data points span a plane in the three-dimensional ($N_{[001]}$,$N_{[1\bar{1}0]}$, $\log(\frac{\nu_0}{\nu_{\mathrm{unit}}})$)-space with $\nu_{\mathrm{unit}} = 1\,\mathrm{Hz}$. Only island no. 1 deviates. The attempt frequencies range from high values (red) in the upper left to low values (blue) in the lower right part of the graph. Fitting a plane of the form

$$\nu_{fit}(N_{[001]}, N_{[1\bar{1}0]}) = 10^{(c_{[001]}N_{[001]}+c_{[1\bar{1}0]}N_{[1\bar{1}0]}+c_0)}\mathrm{Hz} \tag{6.3}$$

to the data disregarding island no.1 leads to $c_{[001]} = -0.14 \pm 0.02$, $c_{[1\bar{1}0]} = 0.12 \pm 0.03$, and $c_0 = 16.3 \pm 0.4$. For comparison Fig. 6.6 (A) shows on the right hand side the relative deviation Δ_{fit} of the experimental data $\nu_0(i)$ from the fitted plane $\nu_{fit}(N_{[001]}, N_{[1\bar{1}0]})$

$$\Delta_{fit} = \frac{\log\left[\frac{\nu_0(i)}{\nu_{\mathrm{unit}}}\right] - \log\left[\frac{\nu_{fit}(N_{[001]}(i),N_{[1\bar{1}0]}(i))}{\nu_{\mathrm{unit}}}\right]}{\log\left[\frac{\nu_{fit}(N_{[001]}(i),N_{[1\bar{1}0]}(i))}{\nu_{\mathrm{unit}}}\right]} \quad . \tag{6.4}$$

One finds $|\Delta_{fit}| \leq 3\%$ for $i = (2, \ldots, 11)$ reflecting good accordance between the fit and the experimental data. Only island no. 1 shows a deviation of $\Delta_{fit}(1) = -18\%$. This will be discussed later.

From the analysis of the energy barrier it was shown that reversal takes place via domain wall nucleation and propagation along the [001] direction. The attempt frequency reveals a tendency to *decrease* when the island is elongated along [001] ($c_{[001]} < 0$), but to *increase* with an increasing island length in $[1\bar{1}0]$ direction ($c_{[1\bar{1}0]} > 0$). This behavior can be explained with a more detailed view on the switching process:
Once the nucleation droplet has reversed its magnetization and the domain wall is created, it diffuses through the island moving forward but also backward. The wall can then be regarded in absence of any external forces as a quasi particle performing a random walk in a one dimensional box with adsorbing walls [75]. A step towards longer domain wall length is unfavorable with respect to energy and thereby less probable than a step that shrinks its length. Therefore the domain wall is likely to annihilate (or be *adsorbed* in the frame of random walk) again, right after its nucleation. However, if the thermal energy is high enough, some of the created walls will succeed to increase their length stepwise to the maximum length which occurs at the particle's largest width along the $[1\bar{1}0]$ direction. Moving forward and backward is then equally probable since the domain wall movement itself does not cost energy. Note that these microscopic processes occur on a much shorter timescale than our experimental time resolution of some

milliseconds [76, 77]. We therefore record only successful switching events, that are very seldom in comparison to the attempt frequency. These views explain the observation of decreasing attempt frequency at increasing island length in [001] direction (see Fig. 6.6 (B)): A successful diffusion process of the domain wall through the whole particle, and therewith magnetization reversal, becomes less probable with increasing island size in the [001] direction. The wall may revert its direction of movement on the way and vanish at its nucleation site, thereby restoring the original configuration without magnetization reversal. Increasing the particle length in $[1\bar{1}0]$ direction has the opposite effect: As it is sketched in Fig. 6.6 (C) the number of possible nucleation sites increases with increasing particle diameter along the $[1\bar{1}0]$ direction. This elevates the switching probability and therefore $\nu_0(N_{[1\bar{1}0]})$. The factor 10^{c_0} Hz in Eq. (6.3) can be assigned to be the attempt frequency of the droplet nucleation, that is the same for all islands.

Island no. 1 does not fit well into this picture: Its determined attempt frequency of $\nu_0(1) \approx 6 \cdot 10^{12}$ Hz is orders of magnitude lower than the values found for all other islands. This indicates that the reversal process in this case deviates from the other. Reversal might be realized by coherent rotation, due to the small particle size. Brown calculated for a single-domain Stoner-Wohlfarth particle $\nu_0 \approx 10^{10}$ Hz [36], and experimental investigations found values of comparable order [78, 79] being therewith slightly lower than those found here. Island no. 1 might also mark a crossover regime between domain wall and coherent reversal, such as found for the transition between single- and multi-domain nucleation [80, 81]. However, since the magnitude of the attempt frequency not only depends on particle size and shape as shown here, but also on parameters such as the damping of the magnetic moment(s), the potential landscape, and others [82], no final conclusions can be drawn. Detailed investigations on islands consisting of 30 atoms and less are required to reveal which switching mechanism occurs in smaller islands.

6.2 Anisotropy and exchange stiffness

The knowledge of domain wall energy $E_{\mathrm{dw}} \propto \sqrt{AK}$ and width $w \propto \sqrt{A/K}$ allows for a determination of exchange stiffness A and magnetic anisotropy K of a system. Since the magnetization reversal process is too fast to detect the propagating domain wall in our experimental setup, static domain wall configurations must be created to enable for a domain wall width determination. Therefore monolayer stripes of Fe on W(110) have been prepared and several static domain walls investigated. Figure 6.7 (A) shows a magnetic $\mathrm{d}I/\mathrm{d}U$ map of nearly one ML Fe on W(110). Several terraces with alternating magnetic contrast can be recognized, including one stripe containing a domain wall. Figure 6.7 (B) shows a tilted zoom

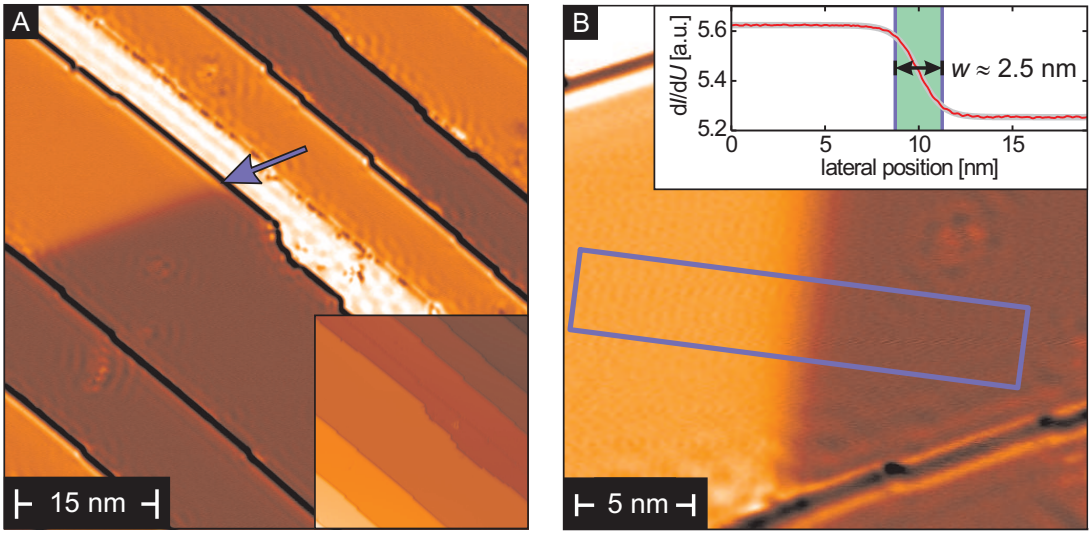

Figure 6.7: (**A**) $\mathrm{d}I/\mathrm{d}U$ map of nearly 1 ML Fe on W(110). One iron stripe contains a domain wall (see arrow). The corresponding topography image is shown in the inset. (**B**) Magnetic map around the domain wall shown in (A). The area in the box is used for an averaged line profile, shown as red curve in the inset. Fitting a domain wall profile yields $w = (2.51 \pm 0.01)\,\mathrm{nm}$ (gray curve).

in at that position. The box marks the area taken for an averaged line profile shown in the inset. Fitting this profile with

$$y(x) = y_0 + y_{sp} \cos\left[\arccos\left(\tanh\left(\frac{x - x_0}{w/2}\right)\right) + \phi\right] \quad , \tag{6.5}$$

where $y(x)$ denotes the magnetic $\mathrm{d}I/\mathrm{d}U$ signal at position x, $y_0(y_{sp})$ the spin-averaged (spin-polarized) contribution to the $\mathrm{d}I/\mathrm{d}U$ signal, x_0 the position of the wall center, and ϕ the angle between tip and sample magnetization [83], results in the gray curve in the inset of Fig. 6.7 (B). It shows good agreement with the data and yields a domain wall width of $w = (2.51 \pm 0.01)\,\mathrm{nm}$. This procedure was applied to different static domain walls found. An averaged domain wall width of $w_{av} = (2.15 \pm 0.35)\,\mathrm{nm}$ was determined.

This result deviates from earlier studies on this sample system. Pratzer *et al.* investigated the monolayer and doublelayer system Fe/W(110) [63, 64]. Samples of 1.5 ML Fe/W(110) were examined and a domain wall energy of $e_{\mathrm{dw}} = (15.2 \pm 1.4)\,\mathrm{meV}$ per atomic row was determined for the monolayer by Kerr magnetometry as well as a domain wall width of $w = (0.6 \pm 0.2)\,\mathrm{nm}$ by means of SP-STM [63, 64]. We dedicate the different findings to the different sample quality: The surface images of Fig. 2 in [63] show an elevated impurity contamination

in the iron monolayer in comparison to our samples where the monolayer shows almost no impurity (see Fig. 6.7). It is frequently observed with SP-STM for samples of coexisting monolayer and doublelayer iron stripes on W(110), that the vast number of impurities resides in the first monolayer, whereas the second layer is very clean. However, a large number of imperfections affects the magnetic properties of a system by decoupling neighboring iron atoms from another and changing the coordination of the pure material. Non-magnetic impurities thereby affect the effective exchange stiffness as well as the effective anisotropy, leading to other values for e_{dw} and w.

As mentioned before, the domain wall energy in a three-dimensional system is given by $E_{\mathrm{dw}} = 4S\sqrt{A \cdot K}$, the exchange stiffness A in units of $\left[\frac{J}{m}\right]$ and the anisotropy energy in $\left[\frac{J}{m^3}\right]$. For a two-dimensional system this equation changes to

$$E_{\mathrm{dw,2d}} = 4L\sqrt{A_{2d} \cdot K_{2d}} \quad . \tag{6.6}$$

The wall area S is replaced by the domain wall length L. A_{2d} is given now in $[J]$, and K_{2d} in $\left[\frac{J}{m^2}\right]$. Since the measured energy barriers reveal domain walls lying in $[1\bar{1}0]$ direction, L may be expressed by the particle length $N_{[1\bar{1}0]}$ in number of atomic rows via $L = N_{[1\bar{1}0]}a/\sqrt{2}$. Due to the pseudomorphic growth of the first layer iron on W(110) the lattice constant $a = 0.316\,\mathrm{nm}$ is set to the value for tungsten. Inserting this into Eq.(6.6) gives as energy per atomic row

$$e_{\mathrm{dw}} = 2^{\frac{3}{2}}a\sqrt{A_{2d} \cdot K_{2d}} \quad .$$

By combining with $w = \sqrt{\frac{A_{2d}}{K_{2d}}}$ one finds

$$A_{2d} = (1.45 \pm 0.07) \cdot 10^{-21}\mathrm{J}$$

and

$$K_{2d} = (1.25 \pm 0.07) \cdot 10^{-3}\frac{\mathrm{J}}{\mathrm{m}^2} \quad .$$

Including the domain wall height $h = a/\sqrt{2}$ by $S = L \cdot h$ gives the parameters in the accustomed units for bulk systems:

$$A = (6.5 \pm 0.3) \cdot 10^{-12}\frac{\mathrm{J}}{\mathrm{m}}$$

and

$$K = (5.6 \pm 0.3) \cdot 10^{6}\frac{\mathrm{J}}{\mathrm{m}^3} = (0.55 \pm 0.03)\frac{\mathrm{meV}}{\mathrm{atom}} \quad .$$

To determine the energy barrier E_{nuc} for the droplet nucleation, possible rim effects have to be considered. Perimeter atoms may make a significantly different

contribution to the magnetic anisotropy due to their reduced coordination number, as was recently shown for two-dimensional Co nanostructures on Pt(111) surfaces [84]. Assuming that island no. 1 is switching purely coherently, we can estimate the anisotropy for the rim atoms by examination of the island topography in terms of inner and rim atoms. Starting from

$$E_{\mathrm{b}}(1) = (103 \pm 3)\mathrm{meV} = E_{\mathrm{coh}} = N_{\mathrm{rim}} \cdot K_{\mathrm{rim}} + N_{\mathrm{inner}} \cdot K$$

one finds with $N_{\mathrm{rim}} = 17\,\mathrm{atoms}$, $N_{\mathrm{inner}} = 14\,\mathrm{atoms}$

$$K_{\mathrm{rim}} \approx 5.6 \frac{\mathrm{meV}}{\mathrm{atom}} \quad .$$

Due to the reduced number of nearest neighbors at the rim (two neighbors instead of four), the effective exchange stiffness A_{rim} of perimeter atoms reduces to $A_{\mathrm{rim}} = A/2$. Thus, the energy for a domain wall with the length $L = 2\,\mathrm{AR}$ (consisting of two *rim* atoms) should be $E_{\mathrm{dw}} = 2^{\frac{3}{2}} a \sqrt{A_{\mathrm{rim}} \cdot K_{\mathrm{rim}}} = 33.9\,\mathrm{meV}$. Since the experiment yields $E_{\mathrm{b}}(N_{[1\bar{1}0]} = 2) = 76\,\mathrm{meV}$, the difference can be attributed to the energy necessary to reverse a nucleation volume:

$$E_{\mathrm{nuc}} = E_{\mathrm{b}}(N_{[1\bar{1}0]} = 2) - E_{\mathrm{dw}} \approx 42\,\mathrm{meV} \quad .$$

To summarize, the thermal switching behavior of eleven Fe nanoislands on W(110) was investigated at different temperatures. An Arrhenius-like dependency of the lifetimes on the experiment temperature was observed, allowing to determine for each island an energy barrier E_b and an attempt frequency ν_0 for the magnetization reversal. The detailed analysis of these parameters as a function of the respective island dimension in the two distinct crystallographic directions [001] and $[1\bar{1}0]$ reveals that magnetization reversal is achieved by domain wall nucleation and propagation. From the linear dependence of E_b on the island size in $[1\bar{1}0]$ direction one concludes that the domain wall lies along $[1\bar{1}0]$ and propagates along [001] through the nanostructure. The investigation of the attempt frequencies for the different islands gives new insights into the size and shape dependency of the Arrhenius prefactor. Since the way the domain wall needs to diffuse for magnetization reversal increases with particle size in [001] dimension, a decreased attempt frequency was found for particles elongated along [001]. In contrast, a particle elongated along the $[1\bar{1}0]$ direction shows more possible nucleation sites at its rim, thus, increasing the attempt frequency. Finally, additional measurements on static domain wall widths w on iron monolayer stripes allowed the determination of the exchange stiffness A and the anisotropy K for inner and perimeter island atoms. The comparison with earlier investigations on this system yields a discrepancy in the determined domain wall energy and width that is ascribed to a considerable difference in sample cleanliness.

Chapter 7

Magnetization manipulation in the thermally activated regime

This section is dedicated to the effects of an elevated spin-polarized current on the intrinsic thermal switching behavior of nanostructures. The microscope's tip is positioned above the center of a nanoisland, and the switching is observed under the influence of high tunnel currents that are achieved by decreasing the tip-sample distance with a closed feedback loop.
Figure 7.1 (A) shows three $\mathrm{d}I/\mathrm{d}U$ (t) trace sections recorded on one particular nanoisland at different tunnel currents I. In order to draw amplitude histograms as depicted in Fig. 7.1 (B), the respective signals were recorded over a long time period ($t = 700\,\mathrm{s}$). At a low tunnel current of $I = 2\,\mathrm{nA}$, the magnetic $\mathrm{d}I/\mathrm{d}U$ signal frequently changes between two signal levels, that correspond to the two possible magnetization states "0" and "1" of the island. As a convention, a low (high) signal is defined as state "0" ("1"). This intrinsic switching is due to thermal agitation as shown in chapter 6, and the respective histogram reveals that both states "0" and "1" occur on the long timescale with equal probability, as expected for an uniaxial system. When the tunnel current is increased to $I = 800\,\mathrm{nA}$, an imbalance of the two states evolves. The trace section of the $\mathrm{d}I/\mathrm{d}U$ signal shows that state "0" is favored in comparison to state "1". The asymmetry becomes even more clearly visible at $I = 2000\,\mathrm{nA}$, where the island remains in state "0" most of the time and populates state "1" only for short times (A), as confirmed by the respective histogram (B).
Fitting the histogram peaks by Gaussians with areas A_0 and A_1, respectively, allows the quantification of the imbalance between state "0" and state "1". Therefore, a histogram asymmetry a_H is introduced:

$$a_\mathrm{H} = \frac{A_1 - A_0}{A_1 + A_0} \quad . \tag{7.1}$$

For $I = 2\,\mathrm{nA}$ one finds $a_\mathrm{H} = (-0.7 \pm 0.5)\,\%$, for $I = 800\,\mathrm{nA}$ $a_\mathrm{H} = (-39.4 \pm 0.7)\,\%$, and for $I = 2000\,\mathrm{nA}$ the asymmetry becomes $a_\mathrm{H} = (-74 \pm 1)\,\%$.

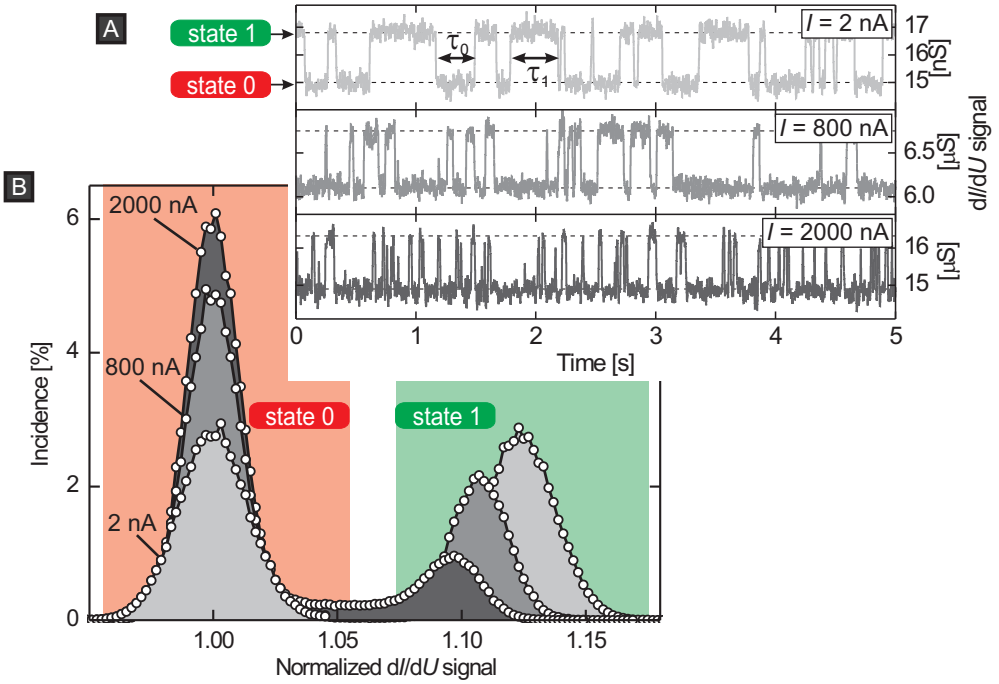

Figure 7.1: Thermal magnetization switching of a nanoisland under influence of elevated tunnel currents. (**A**) Trace sections of the telegraphic $\mathrm{d}I/\mathrm{d}U$ signal of one particular nanoisland recorded at different tunnel currents I. With increasing current, an imbalance between the lifetimes τ_0 and τ_1 for the two states evolves ($T = 48.4\,\mathrm{K}$, $U = -200\,\mathrm{mV}$, $E_\mathrm{b} = (138 \pm 4)\,\mathrm{meV}$, island area: $(5.7 \pm 0.4)\mathrm{nm}^2$). (**B**) Histogram of the respective magnetic $\mathrm{d}I/\mathrm{d}U$ signal recorded over $t = 700\,\mathrm{s}$ and normalized with respect to the state "0" level at different tunnel currents. Whereas both states are equally populated at low currents, an asymmetry toward state "0" evolves with increasing current.

In contrast to the measurements shown before in which the intrinsic switching behavior was *observed* at low tunnel currents, an elevated, spin-polarized tunnel current obviously *affects* the switching behavior and *changes* the effective energy barrier separating the two magnetization states. Obviously a spin-torque is acting. As a result, an imbalance between the two possible magnetization states evolves with increasing tunnel current and the island favors one of the two magnetic states over the other.

7.1 Polarity dependence

In his theoretical work Slonczewski [85] predicted a spin torque inversion when changing the current direction (see chapter 3). Whereas this has been verified in experiments with layered devices in which the tunnel barrier is realized by uti-

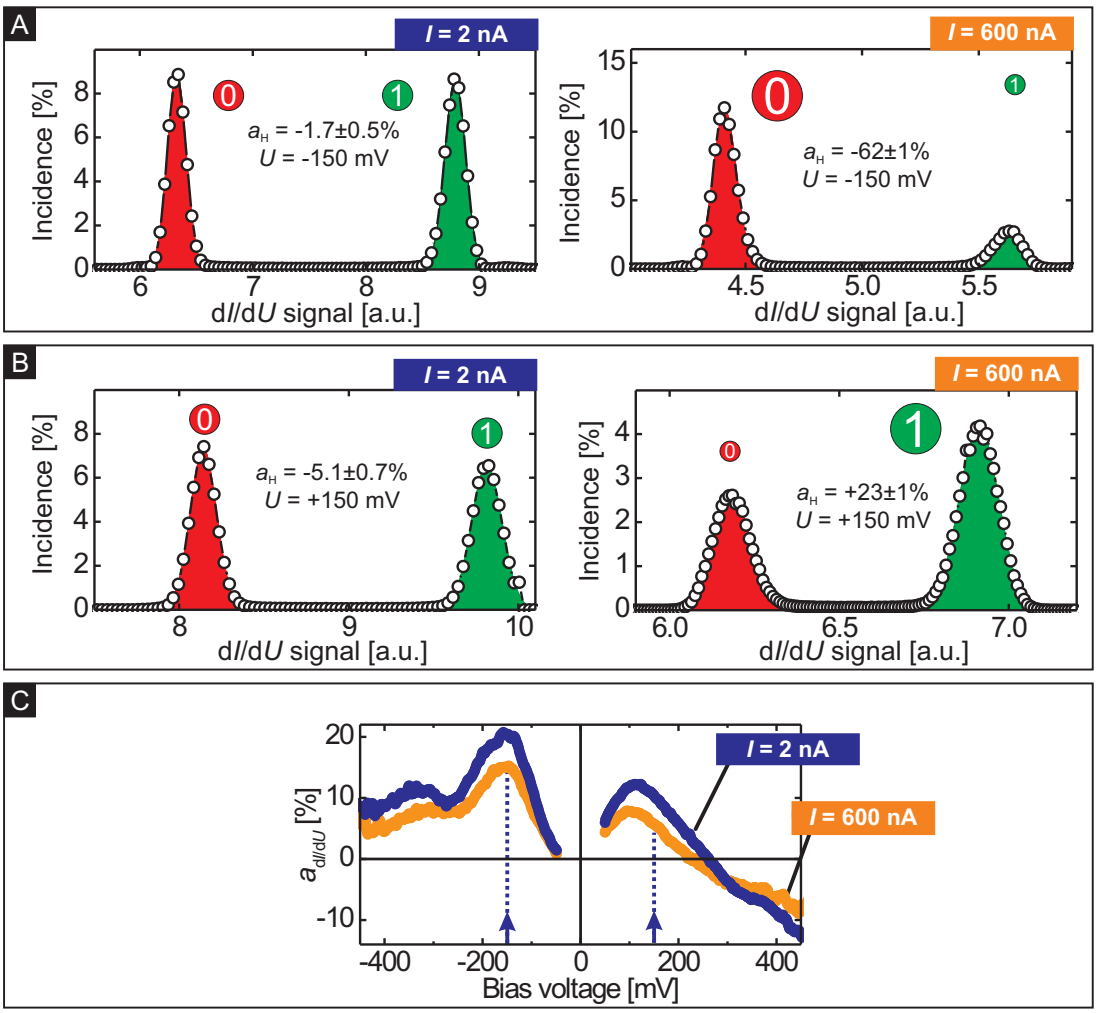

Figure 7.2: (**A**) $\mathrm{d}I/\mathrm{d}U$ asymmetry $a_{\mathrm{d}I/\mathrm{d}U}$ as function of bias U at a low ($I = 2\,\mathrm{nA}$) and a high tunnel current ($I = 600\,\mathrm{nA}$). The asymmetry is positive for both $U = \pm 150\,\mathrm{mV}$. (**B**) and (**C**) Histogram of the magnetic $\mathrm{d}I/\mathrm{d}U$ signal recorded with the same tip on a frequently switching island ($U = \pm 150\,\mathrm{mV}$). At a low current only small asymmetries are observable (B) whereas high asymmetries are found at a high tunnel current (C). The favored magnetization state therefore depends on the current polarity (island area: $(8.6 \pm 0.5)\,\mathrm{nm}^2$, $T = 55.9\,\mathrm{K}$).

lizing insulating materials [9], experimental proof of whether this also holds for vacuum barriers is still lacking. To verify this proposition, the effect of elevated currents on the switching behavior was investigated as a function of bias polarity.

The tip was positioned above a frequently switching island and the magnetic $\mathrm{d}I/\mathrm{d}U$ (t) signal recorded at a low and a high tunnel current for different polarities. Figure 7.2 shows the resulting amplitude histograms for a negative (A) and a positive (B) bias polarity. At the negative bias and a low tunnel current

a small negative histogram asymmetry is observable. When increasing the current to $I = 600\,\mathrm{nA}$, an imbalance towards state "0" evolves and the histogram asymmetry rises to $a_\mathrm{H} = -(62 \pm 1)\%$ (A). Reversing the bias polarity at a low tunnel current again leads to a small negative histogram asymmetry. In contrast, an increase of the tunnel current now leads to an imbalance towards state "1" with an asymmetry of $a_\mathrm{H} = +(23 \pm 1)\%$. To exclude the possibility that tip changes cause these results, the tunnel current and the polarity were repeatedly changed. The results remained the same as shown.
The small negative asymmetries found at low tunnel current, irrespective of the current direction, are probably caused by a residual magnetic stray field of the tip. However, at a high tunnel current the asymmetry sign is dependent on the current direction: For the electrons tunneling from tip to sample, state "1" is favored, and for the electrons tunneling from the sample into the tip, the asymmetry evolves towards state "0".

The question arises, whether indeed two *different* magnetization states are favored at different polarities: a magnetic contrast reversal might occur when going from one bias polarity to the other. State "1" could, for instance, appear bright at one bias voltage but dark at the other, leading to a misinterpretation of the histogram asymmetries shown above. To check for a possible contrast reversal, spin-polarized spectroscopy measurements have been performed at a closed feedback loop on a nanoisland exhibiting a very long lifetime $\tau > 1\,\mathrm{min}$. The magnetic state of the island was recorded before and after each spectrum to assign the respective data to one of the two magnetic configurations. Monitoring the $\mathrm{d}I/\mathrm{d}U$ signal on the same nanostructure for both configurations as done here allows us to directly assign differences in the spectra to the respective magnetic configurations.
A measure of the magnetic contrast is the $\mathrm{d}I/\mathrm{d}U$ asymmetry $a_{\mathrm{d}I/\mathrm{d}U}$, defined by

$$a_{\mathrm{d}I/\mathrm{d}U} = \frac{\mathrm{d}I/\mathrm{d}U_1 - \mathrm{d}I/\mathrm{d}U_0}{\mathrm{d}I/\mathrm{d}U_1 + \mathrm{d}I/\mathrm{d}U_0} \quad , \tag{7.2}$$

where $\mathrm{d}I/\mathrm{d}U_1$ ($(\mathrm{d}I/\mathrm{d}U_0)$) is the intensity of the $\mathrm{d}I/\mathrm{d}U$ signal measured for state "1" ("0"). Figure 7.2 (C) shows the asymmetry $a_{\mathrm{d}I/\mathrm{d}U}$ as a function of bias voltage for $I = 2\,\mathrm{nA}$ (blue) and $I = 600\,\mathrm{nA}$ (orange). Quantitatively, both curves exhibit the same features and show positive asymmetries from $U = -500\,\mathrm{mV}$ up to voltages of $U = +250\,\mathrm{mV}$. Therefore no $\mathrm{d}I/\mathrm{d}U$ contrast inversion is expected when changing the current polarity at $U = \pm 150\,\mathrm{mV}$: an island appearing at $U = +150\,\mathrm{mV}$ in state "0" (low $\mathrm{d}I/\mathrm{d}U$ signal) also appears at $U = -150\,\mathrm{mV}$ in state "0". This confirms the previous conclusion: The favored magnetization direction switches back and forth by reversing the current direction.

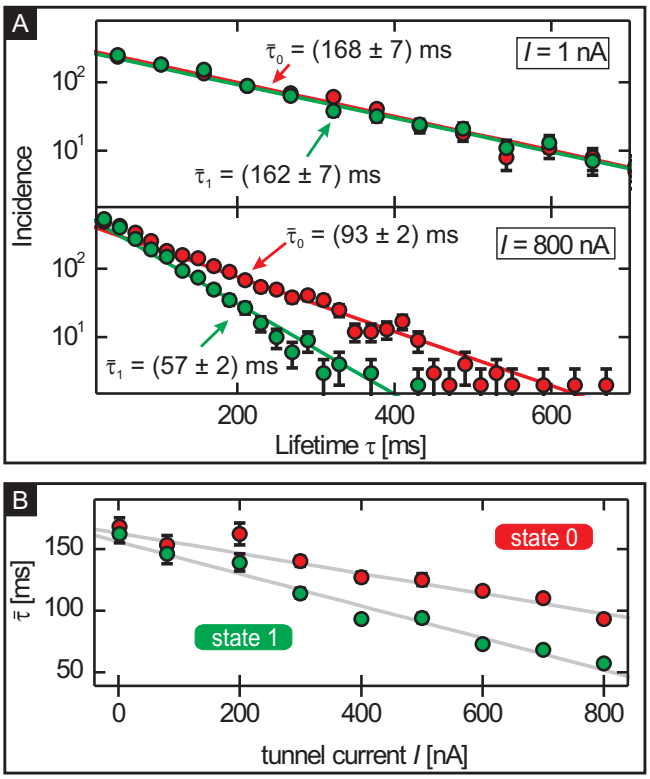

Figure 7.3: (**A**) Lifetime histograms for both states measured at $I = 1\,\mathrm{nA}$ (top) and $I = 800\,\mathrm{nA}$ (bottom). The mean lifetimes $\bar{\tau}_{0,1}$ are determined by fitting exponential decay functions to the experimental data (red and green lines).
(**B**) Resulting mean lifetimes $\bar{\tau}_{0,1}$ as a function of the tunnel current I ($U = -200\,\mathrm{mV}$, $T = 50.6\,\mathrm{K}$, $E_\mathrm{b} = (133 \pm 4)\,\mathrm{meV}$, island size $(5.5 \pm 0.4)\,\mathrm{nm}^2$).

7.2 Separation of microscopic processes

To get a detailed insight into the different microscopic processes caused by the elevated tunnel current, a statistical analysis of the lifetimes as a function of the current was performed. As shown in Chapter 6 for the thermally activated switching, the times between two switching events were evaluated and collected in a histogram. However, this time, the lifetimes for the two states, τ_0 and τ_1, are evaluated separately (see Fig. 7.1 (A)). A low (high) signal is thereby related to state "0" ("1"). Figure 7.3 (A) shows lifetime histograms $h(\tau)$ for both magnetization states of one particular nanoisland measured with the same tip at $I = 1\,\mathrm{nA}$ and $I = 800\,\mathrm{nA}$. The respective mean lifetimes $\bar{\tau}_0$ and $\bar{\tau}_1$ are found by fitting with an exponential decay law of the form $h(\tau) \propto \exp\left(-\frac{\tau}{\bar{\tau}}\right)$. At low tunnel current, both lifetimes are equal within the errors of the measurement. This finding is expected, since the switching observed at low tunnel currents is the unaffected, purely thermally driven magnetization reversal, as shown before. At high tunnel current the mean lifetimes exhibit an asymmetry, and state "0" has a much longer mean lifetime $\bar{\tau}_0$ than state "1". Evaluating $\bar{\tau}_0$ and $\bar{\tau}_1$ for different tunnel currents reveals two contributions to the current-induced magnetization switching (Fig. 7.3 (B)):

1. The mean lifetime decreases for both configurations as a function of the

tunnel current I. An increasing switching frequency is consistent with an effective increase in temperature, as shown in the last chapter. This effect is attributed to Joule heating due to the elevated current:

$$T \to T + \Delta T_{\mathrm{JH}} \quad .$$

2. A lifetime asymmetry evolves with increasing current. This imbalance modifies the effective energy barrier E_{b} depending on the respective magnetization state and is attributed to a spin torque:

$$E_{\mathrm{b}} \to E_{\mathrm{b}} \pm \Delta E_{\mathrm{ST}} \quad .$$

Taking both effects into account, the intrinsic mean lifetimes are modified to

$$\bar{\tau}_{0,1}(I) = \nu_0^{-1} \cdot \exp\left[\frac{E_{\mathrm{b}} \pm \Delta E_{\mathrm{ST}}(I)}{k_{\mathrm{B}}(T + \Delta T_{\mathrm{JH}}(I))}\right] \quad . \tag{7.3}$$

The mean lifetimes for both magnetization states as function of I, $\bar{\tau}_0$ and $\bar{\tau}_1$, allow for a quantitative determination of $\Delta E_{\mathrm{ST}}(I)$ and $\Delta T_{\mathrm{JH}}(I)$ as will be shown in the following.

ΔT_{JH} - Temperature elevation due to Joule heating

The energy barrier $E_{\mathrm{b}} = (133 \pm 4)\,\mathrm{meV}$ was determined by a variation of the temperature T from 50.6 to 48.5 K and derivation of the respective mean lifetimes $\bar{\tau}_{0,1}(I = 1\mathrm{nA}) := \bar{\tau}$ at low tunnel current I. To find the temperature elevation due to Joule heating one calculates

$$\frac{\bar{\tau}_0(I) \cdot \bar{\tau}_1(I)}{\bar{\tau}^2} = \exp\left[\frac{2E_{\mathrm{b}}}{k_{\mathrm{B}}(T + \Delta T_{\mathrm{JH}}(I))} - \frac{2E_{\mathrm{b}}}{k_{\mathrm{B}}T}\right] \tag{7.4}$$

$$\Rightarrow \Delta T_{\mathrm{JH}}(I) = T\left[\left(1 + \frac{k_{\mathrm{B}}T}{2E_{\mathrm{b}}} \ln\left(\frac{\bar{\tau}_0(I) \cdot \bar{\tau}_1(I)}{\bar{\tau}^2}\right)\right)^{-1} - 1\right] \quad . \tag{7.5}$$

The resulting values for $\Delta T_{\mathrm{JH}}(I)$ are plotted in Fig. 7.4 (A). ΔT_{JH} rises with increasing current and reaches at $I = 800\,\mathrm{nA}$ a value of $\Delta T_{\mathrm{JH}} = (1.39 \pm 0.01)\,\mathrm{K}$. An experimental study of the process of heat generation in metal electrodes of a vacuum-barrier tunnel junction [86] shows a linear dependence of the dissipated heat power on the tunnel current at constant bias. Introducing c_{JH} as Joule heating coefficient giving the temperature change per injected current,

$$c_{\mathrm{JH}} = \frac{\mathrm{d}\Delta T_{\mathrm{JH}}}{\mathrm{d}I} \quad , \tag{7.6}$$

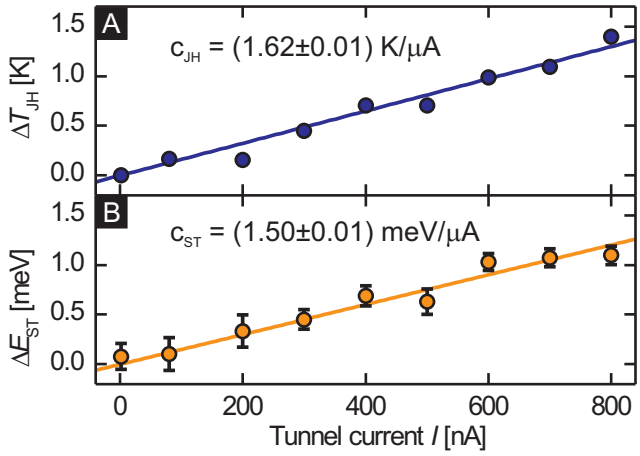

Figure 7.4: (**A**) Effective temperature increase due to Joule heating ΔT_{JH} and (**B**) effective energy barrier change due to spin torque ΔE_{ST} as function of the tunnel current I. Both quantities increase with increasing tunnel current. The coefficients c_{JH} and c_{ST} are found by linear fits.

we can apply the linear fit $\Delta T_{\mathrm{JH}} = c_{\mathrm{JH}} I$. As can be seen in the graph, it shows good agreement with the experimental data. The determined prefactor is $c_{\mathrm{JH}} = (1.62 \pm 0.01)\,\mathrm{K}/\mu\mathrm{A}$.

To theoretically estimate the temperature rise by Joule heating, a model developed by Goldenberg [87] is applied. Consider an energy dissipation $E = UIt$ within a homogeneous half sphere (initially at zero temperature) with the radius r at a constant rate A per unit time t and unit volume V:

$$A = \frac{E}{Vt} = \frac{3}{2}\frac{UI}{\pi r^3} \quad . \tag{7.7}$$

Then the temperature T inside the half sphere will stabilize at

$$T = \frac{r^2 A}{\lambda} = \frac{3}{2}\frac{UI}{\pi r \lambda} \quad , \tag{7.8}$$

where λ denotes the thermal conductance of the sphere. The energy of the tunneling electrons is assumed to be dissipated within 1 to 2 nm. This is about the inelastic mean free path of electrons [88]. With the thermal conductivity of tungsten being $\lambda_{\mathrm{W}} = 427\,\mathrm{J}/(\mathrm{m}\cdot\mathrm{K})$ at $T = 50\,\mathrm{K}$ one finds a temperature change of $T/I \approx 0.15\,\mathrm{K}/\mu\mathrm{A}$ within this model. This value is about one order of magnitude smaller than determined in our experiment. Nevertheless, it also shows a linear dependence of the heat dissipation on the current, in agreement with our findings. Note that the temperature elevation ΔT_{JH} can be expressed as an effective energy barrier modification by rewriting the Boltzmann exponent in Equation (7.3) to

$$\frac{E_{\mathrm{b}}}{k_{\mathrm{B}}(T + \Delta T_{\mathrm{JH}})} = \frac{E_{\mathrm{b}}}{k_{\mathrm{B}} T} \cdot \left(1 + \frac{\Delta T_{\mathrm{JH}}}{T}\right)^{-1} = \frac{E_{\mathrm{b}}\left(1 - \frac{\Delta T_{\mathrm{JH}}}{T + \Delta T_{\mathrm{JH}}}\right)}{k_{\mathrm{B}} T} = \frac{E_{\mathrm{b}} - \Delta E_{\mathrm{JH}}}{k_{\mathrm{B}} T}.$$

The original energy barrier E_b is therefore reduced by

$$\Delta E_\mathrm{JH}(I) = \left(\frac{\Delta T_\mathrm{JH}}{T + \Delta T_\mathrm{JH}}\right) E_\mathrm{b}$$

due to the Joule heating delivered by the elevated current. Hence, the temperature elevation of $\Delta T_\mathrm{JH}(I = 800\,\mathrm{nA}) = 1.39\,\mathrm{K}$ corresponds to an energy barrier reduction of $\Delta E_\mathrm{JH} = 0.027 E_\mathrm{b} \approx 3.6\,\mathrm{meV}$.

ΔE_ST - Energy barrier modification due to spin torque

The second effect observed with increasing current was an evolving lifetime asymmetry. To determine the effective energy barrier modification due to spin torque one calculates

$$\frac{\bar{\tau}_1(I)}{\bar{\tau}_0(I)} = \exp\left[\frac{2\Delta E_\mathrm{ST}(I)}{k_\mathrm{B}(T + \Delta T_\mathrm{JH}(I))}\right] \tag{7.9}$$

$$\Rightarrow \Delta E_\mathrm{ST}(I) = \frac{k_\mathrm{B}(T + \Delta T_\mathrm{JH}(I))}{2} \ln\left(\frac{\bar{\tau}_1(I)}{\bar{\tau}_0(I)}\right) \quad . \tag{7.10}$$

The resulting data for $\Delta E_\mathrm{ST}(I)$ is shown in Fig. 7.4 (B). It obviously rises linearly with the tunnel current, and reaches $\Delta E_\mathrm{ST} = (1.1 \pm 0.1)\,\mathrm{meV}$ at $I = 800\,\mathrm{nA}$. A linear dependence of ΔE_ST on the current is expected from the macrospin model (see chapter 3). Defining c_ST as a spin torque coefficient giving the effective energy barrier change per injected current,

$$c_\mathrm{ST} = \frac{\mathrm{d}\Delta E_\mathrm{ST}}{\mathrm{d}I} \quad , \tag{7.11}$$

we can apply the linear fit $\Delta E_\mathrm{ST} = c_\mathrm{ST} I$ and find $c_\mathrm{ST} = (1.50 \pm 0.01)\,\mathrm{meV}/\mu\mathrm{A}$. If Joule heating is neglected, the mean lifetimes can be expressed by [34, 89]

$$\bar{\tau}_{0,1} = \nu_0^{-1} \cdot \exp\left[\frac{E_\mathrm{b}}{k_\mathrm{B}T}\left(1 - \frac{I}{I_\mathrm{crit}}\right)\right] \quad . \tag{7.12}$$

I_crit denotes the critical current necessary to switch the magnetization at $T = 0\,\mathrm{K}$. Here we find $I_\mathrm{crit} = (89 \pm 4)\,\mu\mathrm{A}$ for a switching due to a pure spin torque without any Joule heating. Such a current is far too high to be realized within the tunnel regime. This demonstrates the importance of the Joule heating: whereas in most other experiments it is neglected or undesired, here it plays an important role and essentially assists the magnetization reversal by lowering the effective barrier.

Assuming an effective tunneling area given by the lateral STM resolution of 5 Å [90], the threshold current density corresponding to I_crit is $j \approx 10^{10}\mathrm{A/cm^2}$.

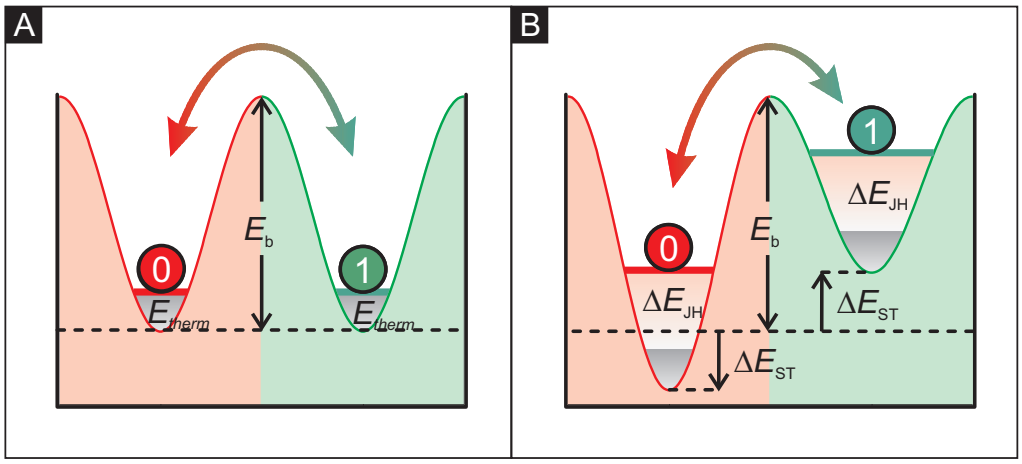

Figure 7.5: Manipulation of the intrinsic switching behavior of a nanoisland. (**A**) Low tunnel current: Due to the thermal energy $E_{\mathrm{therm}} = k_{\mathrm{B}}T$ of the system, the magnetization is switching frequently between the two degenerate states "0" and "1". Both states are therefore equally probable. (**B**) Manipulation at high tunnel current: An elevated spin-polarized current I changes the switching behavior by Joule heating and spin torque. The former gives rise to a temperature elevation ΔT_{JH} lowering the effective barrier height on both sides by ΔE_{JH}. The latter lifts the degeneracy of the two magnetization states by in- or decreasing the barrier by $\pm\Delta E_{\mathrm{ST}}$. Therefore one state (here state "0") is favored against the other.

This value is three orders of magnitude higher than the current density used in similar experiments based on TMR devices [9]. In these planar junctions the current is assumed to flow homogeneously through the whole sample plane, but in fact the metal-insulator interfaces are buried within the device, and interface roughness as well as leakage channels causing an inhomogeneous current distribution (and therefore locally higher current densities) cannot be excluded. In our case however, the current density is distributed inhomogeneously over the magnetic island and therefore acts very locally.

To summarize, Figure 7.5 illustrates how spin torque and Joule heating affect the effective energy barrier: at low currents the magnetization switches between the two degenerate magnetization states. The energy barrier E_{b} between the two states can be overcome by the thermal energy E_{therm} of the system and both states occur with the same probability (A). High tunnel currents give rise to Joule heating affecting the temperature of the system, thereby decreasing the effective energy barrier for both states symmetrically by ΔE_{JH} (B). Spin torque additionally lifts the degeneracy of the two magnetization states by increasing or decreasing the effective energy barrier by ΔE_{ST}. Consequently, one of the two states is favored and exhibits a longer lifetime than the other.

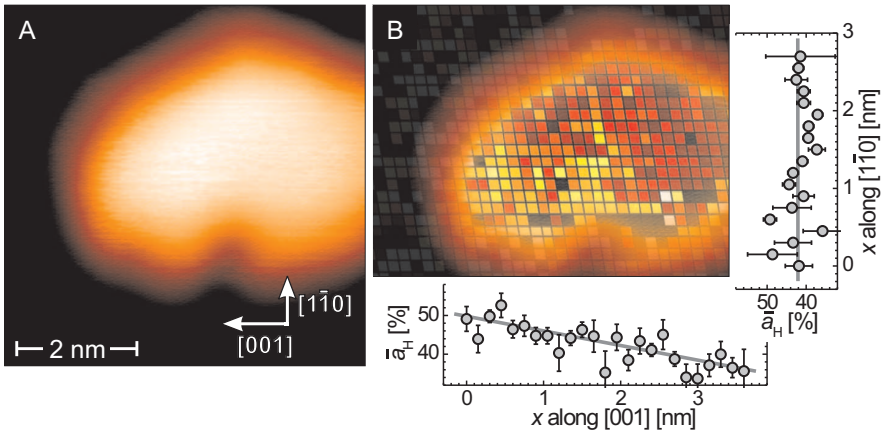

Figure 7.6: (**A**) Topography and (**B**) map of the current-induced asymmetry a_H ($I = 600\,\mathrm{nA}$, $U = +200\,\mathrm{mV}$, island area: $(6.7 \pm 0.6)\mathrm{nm}^2$, $T = 55.0\,\mathrm{K}$). The graphs in the inset depict a_H averaged in rows (along the $[1\bar{1}0]$ direction) and columns (along the [001] direction), respectively. Along the $[1\bar{1}0]$ direction $\bar{a}_H$ is constant within the error bars, but it decreases by about 16% from the left to the right side of the island (gray lines are guides to the eye).

7.3 Spatially resolved measurements

One important advantage of the SP-STM measurement technique is the possibility to move the probe tip, acting as an electron source or drain, with a high precision over a sample surface. In combination with its lateral resolution, it enables the performance of spatially resolved measurements on different sites of one particular nanostructure, giving insights that are inaccessible with lateral averaging techniques.

A frequently switching nanoisland consisting of about 100 atoms was chosen for spatially resolved measurements at high currents. The topography is shown in Fig. 7.6 (A). Figure 7.6 (B) shows a spatially resolved, color-coded map of histogram asymmetry a_H at a tunnel current of $I = 600\,\mathrm{nA}$: At every pixel the magnetic $\mathrm{d}I/\mathrm{d}U$ signal was recorded for a duration of $t = 12\,\mathrm{s}$ to allow for the evaluation of the corresponding $\mathrm{d}I/\mathrm{d}U$ histograms.
A gradient from bright, yellow pixels to red, dark ones can be found along the [001] direction. Averaging a_H column- and row-wise, i.e. along [001] and $[1\bar{1}0]$, enables for a quantitative analysis: Whereas the asymmetry remains more or less constant along $[1\bar{1}0]$, $\bar{a}_H$ decreases from about $\bar{a}_H^{\mathrm{le}} = 50\%$ at the left island end to roughly $\bar{a}_H^{\mathrm{ri}} = 34\%$ at the right island side (see insets of Fig. 7.6 (B)). The switching behavior is obviously dependent on the lateral tip position along the [001] direction. In other words: The effect of the elevated tunnel current on the switching behavior turns out to have an additional character that depends on the

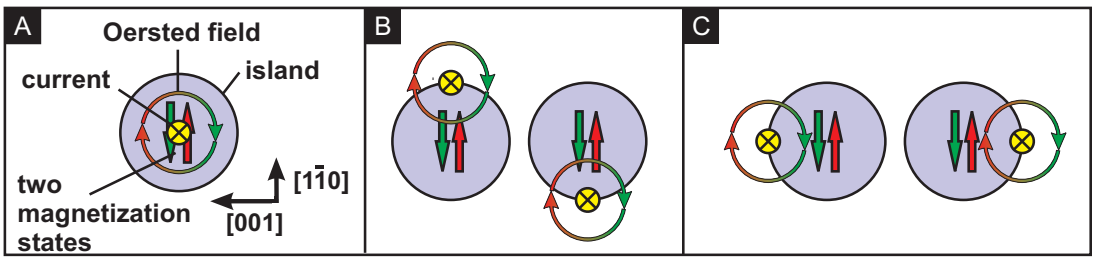

Figure 7.7: Schematic to illustrate the influence of the Oersted field with the tip positioned (**A**) in the center, (**B**) at the magnetic poles or (**C**) at the charge-free sides of the nanoisland.

lateral current injection site.
Every electron current is accompanied by an Oersted field surrounding it, with distance-dependent amplitude and direction. Figure 7.7 schematically compares the configuration of the Oersted field and island magnetization when the current injection is carried out at different lateral sites on the island. If the tip is positioned above the island's center (A), the Oersted field cancels out and no influence is expected. Switching is now only affected by Joule heating and spin torque. Moving the tip along [1$\bar{1}$0] (B) also leads to no effect: the field portion acting on the island is effectively oriented along [001], thus perpendicular to the easy magnetization axis of the island along [1$\bar{1}$0]. Only a tip displacement along [001] direction (C) leads to an effect: the Oersted field affecting the island is now effectively pointing along [1$\bar{1}$0], parallel to one, and antiparallel to the other magnetization state of the island, depending on the site of current injection ("left" or "right" island end), thereby favoring one of the two magnetization states against the other.

The mean lifetimes are now modified by an additional site-dependent energy ΔE_{OE} due to the Oersted field

$$\bar{\tau}_{1,0}(I,\vec{r}_{\mathrm{tip}}) = \nu_0^{-1} \cdot \exp\left[\frac{E_{\mathrm{b}} \pm \Delta E_{\mathrm{ST}}(I) + \Delta E_{\mathrm{OE}}(I,\vec{r}_{\mathrm{tip}})}{k_{\mathrm{B}}(T + \Delta T_{\mathrm{JH}}(I))}\right] \quad . \tag{7.13}$$

A maximum energy splitting due to the Oersted field $\Delta E_{\mathrm{OE,max}}$ is achieved when the tip is positioned at the leftmost or rightmost point on the island. To find this maximum from the site-dependent histogram asymmetries $\bar{a}_{\mathrm{H}}$ one calculates the ratio of the energy splitting on the left/right island edge $\Delta E^{\mathrm{le,ri}} = \Delta E_{\mathrm{ST}} \pm \Delta E_{\mathrm{OE,max}}$ and the pure spin torque splitting at the island's center $\Delta E^{c} = \Delta E_{\mathrm{ST}}$. With the help of Eq. (7.10) and making usage of $\frac{\bar{\tau}_1}{\bar{\tau}_0} = \frac{1+a_{\mathrm{H}}}{1-a_{\mathrm{H}}}$, one finds

$$\frac{\Delta E^{\mathrm{le,ri}}}{\Delta E^{c}} = 1 \pm \frac{\Delta E_{\mathrm{OE,max}}}{\Delta E_{\mathrm{ST}}} = \frac{\ln\left[\frac{1+\bar{a}_{\mathrm{H}}^{\mathrm{le,ri}}}{1-\bar{a}_{\mathrm{H}}^{\mathrm{le,ri}}}\right]}{\ln\left[\frac{1+\bar{a}_{\mathrm{H}}^{c}}{1-\bar{a}_{\mathrm{H}}^{c}}\right]} \quad . \tag{7.14}$$

$\bar{a}_{\mathrm{H}}^{c}$ denotes the asymmetries found at the island center where the asymmetry is exclusively caused by spin torque. Inserting the asymmetries found on the different

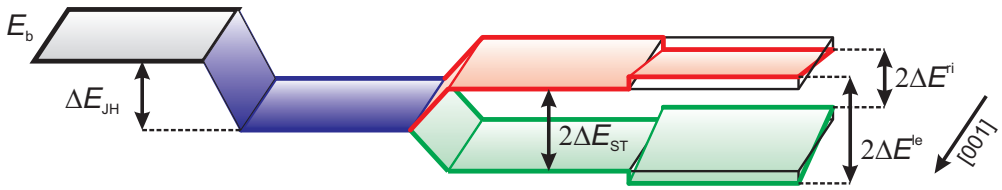

Figure 7.8: Schematic to illustrate the effective energy barrier modification due to combined action of the Joule heating, the spin-torque and the Oersted field. The original energy barrier E_b is effectively lowered by ΔE_{JH} due to Joule heating. Additionally, an energy splitting ΔE_{ST} due to spin torque occurs. This is further in- or decreased by $\Delta E_{OE,max}$ to $\Delta E^{le,ri}$ when the tip is positioned at the leftmost or rightmost on the nanoisland.

island sites gives $\Delta E_{OE,max} \approx 0.22 \cdot \Delta E_{ST}$, showing that the effect of Oersted field is approximately one order of magnitude smaller than the spin torque energy splitting. Using the spin torque coefficient found before ($c_{ST} = (1.50 \pm 0.01)\,\mathrm{meV}/\mu\mathrm{A}$), one finds an effective activation barrier splitting due to spin torque of $\Delta E_{ST} \approx 1\,\mathrm{meV}$ at $I = 600\,\mathrm{nA}$. This splitting is increased or decreased further due to the Oersted field by $\Delta E_{OE,max} \approx 0.22\,\mathrm{meV}$ towards the island ends along the [001] direction, as shown in Fig. 7.8. Note that this number cannot be easily interpreted, as, for instance, a Zeeman splitting in an homogeneous external field, but is rather a measure for the effective impact on the switching in comparison to the spin torque.

To summarize, the main effects achieved by a spin-polarized current are found to be Joule heating and spin torque, whereas the impact of the Oersted field is rather small.

Chapter 8

Controlling the magnetization of quasistable nanoislands

In the last section the manipulation of the thermally-activated magnetization reversal of ferromagnetic nanostructures by injecting elevated tunnel currents was demonstrated. Three fundamental effects of the elevated spin-polarized current were identified and quantified, specifically spin torque, Joule heating and the Oersted field. However, the question arises whether it is also possible to manipulate thermally stable nanostructures by SP-STM. To answer this question, individual thermally quasistable nanoislands were addressed in experiments at elevated currents, either in form of current pulse injection or current ramps. Quasistable is defined as exhibiting lifetimes on the order of minutes and hours, therefore being some orders of magnitudes higher than in the unstable case with lifetimes of seconds or less.

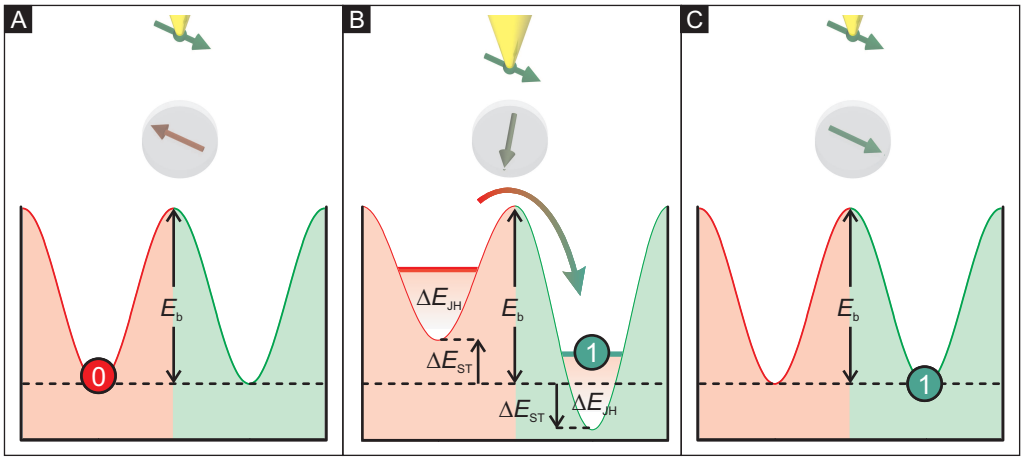

Figure 8.1: Basic principle of switching the magnetization of a nanoisland by applying a short current pulse. (**A**) Initial state: The nanoisland's magnetization is in the state "0". The effective activation barrier E_b prevents the nanoisland from switching. (**B**) Application of a high spin-polarized current pulse originating from a STM tip. The temperature increase due to Joule heating lowers the effective barrier height by ΔE_{JH}. The spin torque exerted on the magnetic structure lifts the degeneracy of the two magnetization states. Decreasing the barrier height for state "0" further by ΔE_{ST}, a magnetization reversal from state "0" to "1" is induced. The barrier height for state "1" is increased, respectively. (**C**) Final state. The magnetization has switched to state "1", and magnetization reversal is hindered again by E_b.

8.1 Current pulses at fixed polarity

Figure 8.1 illustrates the basic idea of triggering magnetization switching by current pulses: In the initial configuration the nanoisland's magnetization is in one of its two stable magnetic states, here the state "0". In contrast to the cases discussed before, the ratio between effective activation energy barrier E_b and thermal energy is small, so thermal switching between these two states is hindered. In order to reverse the magnetization to state "1", the SP-STM tip is brought closer to the nanoisland for a short time (Fig. 8.1 (B)), leading to a spin-polarized tunnel current pulse. During the pulse, Joule heating drastically lowers E_b for both states by ΔE_{JH} and consequently decreases the lifetime of both states. Additionally, the spin torque lowers or elevates E_b by ΔE_{ST}, depending on the state. Here, this results in a further lifetime decrease for state "0" but in an increase for state "1". If the pulse length is on the order of the modified lifetime of state "0", the nanoisland's magnetization is likely to be reversed to state "1". Figure 8.1 (C) shows the final configuration: The magnetization direction is reversed and E_b again prevents switching.

For the experiment the thermally quasistable nanoisland α shown in Fig. 8.2 was chosen. The island consists of 42 ± 5 atoms, and a sequence of $\mathrm{d}I/\mathrm{d}U$ maps, which very seldom showed switching events, allowed the estimation of its lifetime

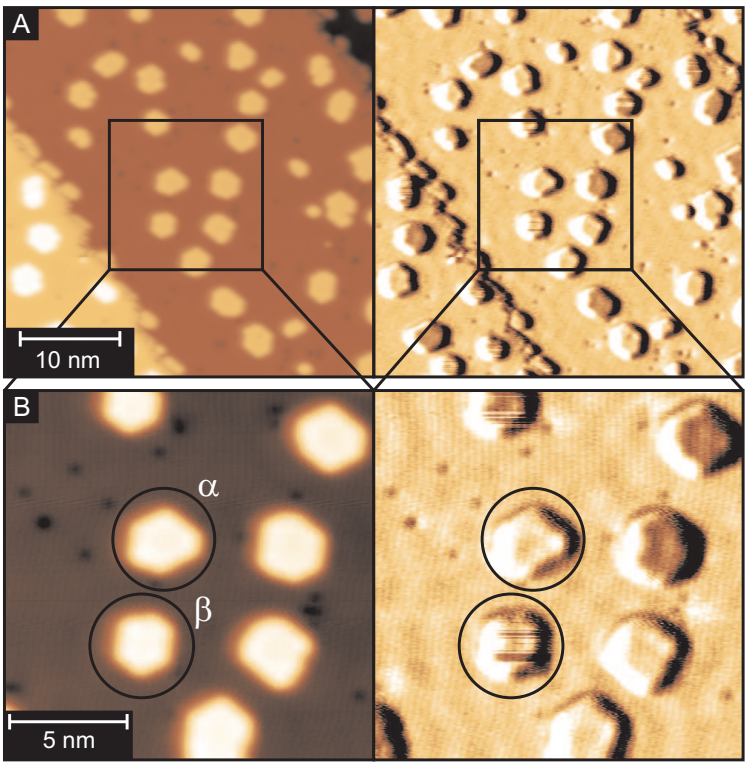

Figure 8.2: Topography and $\mathrm{d}I/\mathrm{d}U$ images of Fe islands on the W(110) surface. (**A**) $(36.8\,\mathrm{nm})^2$ overview and (**B**) $(15.52\,\mathrm{nm})^2$ zoom in. Island α exhibits a lifetime of $\tau \approx 30\,\mathrm{minutes}$, island β is frequently switching during the measurement ($I = 20\,\mathrm{nA}$, $U_{\mathrm{bias}} = -200\,\mathrm{mV}$, $T = 31.5\,\mathrm{K}$).

to $\tau \approx 30\,\mathrm{minutes}$. To apply current pulses, the STM tip is stabilized in point mode above the center of the nanoisland. The short pulses are then carried out by means of programmed command sequences that can be executed automatically or on the push of a button during the experiment. The running data acquisition is then interrupted, the command sequence executed, and the measurement is resumed. For the experiments shown in this section, a script for a short current pulse application including the pulse parameters is programmed and then automatically applied every five seconds.

Figure 8.3 shows a typical current pulse application: Differential conductance $\mathrm{d}I/\mathrm{d}U$ and height z are shown as function of time. At $t = 0\,\mathrm{s}$ the tip is stabilized at a low tunnel current $I_{\mathrm{obs}} = 20\,\mathrm{nA}$ above the chosen nanoislands center to determine its initial state from the $\mathrm{d}I/\mathrm{d}U$ signal level. As before, a low (high) signal is related to state "0" ("1"). Here, the island's magnetization is in state "1". A current pulse is generated at $t = 1\,\mathrm{s}$ by setting the current feedback to $I_{\mathrm{pulse}} = 1.6\,\mu\mathrm{A}$ for a duration of $\tau_{\mathrm{pulse}} = 100\,\mathrm{ms}$, as shown in the inset of Fig. 8.3. Since the lock-in sensitivity is adjusted to the low current regime at an integrating constant of 100 ms to optimize the signal-to-noise ratio, the $\mathrm{d}I/\mathrm{d}U$ signal saturates during the pulse and exhibits a delayed return to its actual value of state "1" or "0". The $\mathrm{d}I/\mathrm{d}U$ signal stabilizes after this pulse application at the lower level, indicating that the island is now in state "0", and the z distance is stabilized by the

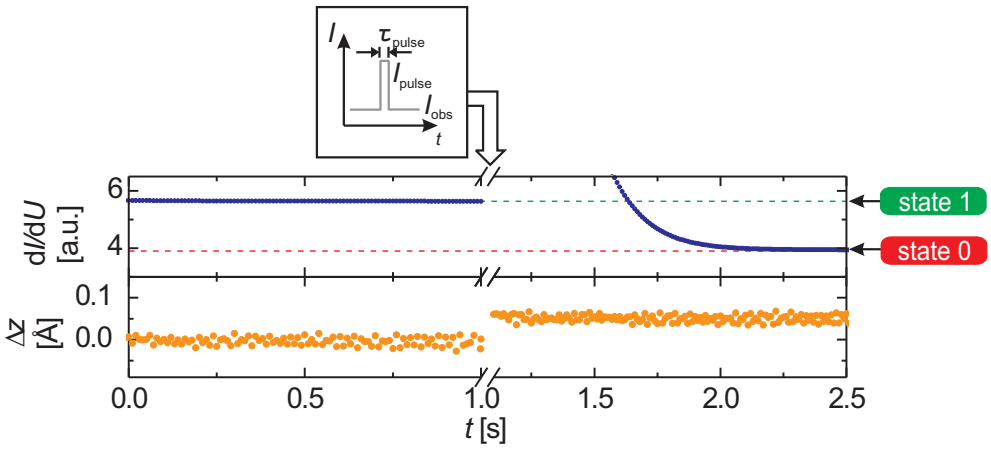

Figure 8.3: Differential conductance $\mathrm{d}I/\mathrm{d}U$ and tip height Δz as function of time for an exemplary pulse application ($U_{\mathrm{bias}} = -200\,\mathrm{mV}$, $I_{\mathrm{obs}} = 20\,\mathrm{nA}$). Initially the island is in its stable magnetic state "1" (high $\mathrm{d}I/\mathrm{d}U$ signal level). At $t = 1\mathrm{s}$ a current pulse is applied, the current is raised for a time $\tau_{\mathrm{pulse}} = 100\,\mathrm{ms}$ to $I_{\mathrm{pulse}} = 1.6\,\mu\mathrm{A}$ (see inset). The $\mathrm{d}I/\mathrm{d}U$ signal at first is saturated before it returns to its actual value (state "0"). The distance z is at its new equilibrium value right after the pulse.

feedback loop to its new position. Thus a current pulse-triggered magnetization reversal in the nanostructure is achieved: the applied current pulse has switched the magnetization of the nanoisland from state "1" to state "0".

Data illustration and analysis

In the experiment several pulse applications are performed with a given parameter-set to allow for a statistical analysis. Figure 8.4 (A) shows the $\mathrm{d}I/\mathrm{d}U$ signal for five subsequent pulse applications in a 3-dimensional view. Prior to each line the command script is executed and a current pulse applied. Then the $\mathrm{d}I/\mathrm{d}U$ signal is recorded for five seconds to determine the magnetization state of the island. Figure 8.4 (B) shows the color-coded $\mathrm{d}I/\mathrm{d}U$ signal recorded for a set of 100 subsequent current pulses. Each of the lines stands for one pulse application. At the beginning of each line the $\mathrm{d}I/\mathrm{d}U$ signal is saturated (colored white) due to the prior current pulse before it sinks to one of the two levels reflecting the island's magnetization state after the respective pulse. The read out of the state is done at the end of each line, prior to the following pulse. Therefore, a cross sectional view of the recorded data was used: Cutting the dataset of Fig. 8.4 (B) along $t = 5\,\mathrm{s}$ results in a bar diagram as can be seen in Fig. 8.4 (C). Two distinct signal levels reflecting the respective magnetization state of the island are clearly distinguishable. The resulting magnetization state of each experiment is shown here color-coded beneath each bar. Red represents state "0" and green state "1". If every pulse application leads to a magnetization reversal, the bar diagram shows

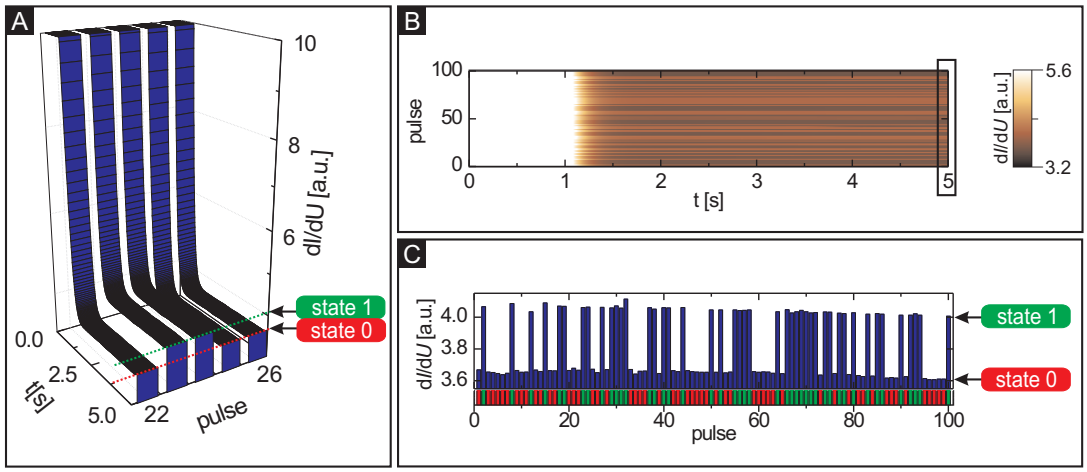

Figure 8.4: (**A**) 3D illustration of the $\mathrm{d}I/\mathrm{d}U$ signal for 5 consecutive current pulse applications ($I_{\mathrm{pulse}} = 2\,\mu\mathrm{A}$, $\tau_{\mathrm{pulse}} = 1\,\mathrm{s}$, $U_{\mathrm{bias}} = -200\,\mathrm{mV}$, $I_{\mathrm{obs}} = 20\,\mathrm{nA}$). A pulse is applied prior to each line. The respective magnetization state of the nanoisland is read out at $t = 5\,\mathrm{s}$: Two $\mathrm{d}I/\mathrm{d}U$ signal levels can be clearly distinguished that correspond to the two possible magnetization states of the islands. (**B**) Color-coded $\mathrm{d}I/\mathrm{d}U$ signal for 100 current pulse applications. The black box marks the cross sectional view in (**C**): the $\mathrm{d}I/\mathrm{d}U$ signal for each line at $t = 5\,\mathrm{s}$ is displayed in a bar diagram for clearer visibility. Red and green color bars beneath the measured $\mathrm{d}I/\mathrm{d}U$ signal indicate the respective magnetization state.

a regular comb-like pattern of alternating high and low $\mathrm{d}I/\mathrm{d}U$ signal levels and in the color-coded read out beneath green and red bars alternate with every pulse. Thus subsequent bars of the same color indicate unsuccessful switching attempts. The probability p to switch the magnetization with one pulse is defined as the number of pulse-triggered events divided by the total number of applied pulses:

$$p = \frac{n_{\mathrm{switch}}}{n_{\mathrm{pulse}}} \quad . \tag{8.1}$$

From the experiments the switching probability p for both switching directions will be calculated for each parameter set independently. Switching the island from state "0" to state "1" is abbreviated with "↑" and switching from state "1" to state "0" with "↓".

Experimental results

To investigate the impact of pulse parameters, experiments at different pulse lengths and amplitudes have been carried out. First, 100 pulses with a pulse amplitude of $I_{\mathrm{pulse}} = 1\,\mu\mathrm{A}$ and a pulse length $\tau_{\mathrm{pulse}} = 100\,\mathrm{ms}$ were applied. The

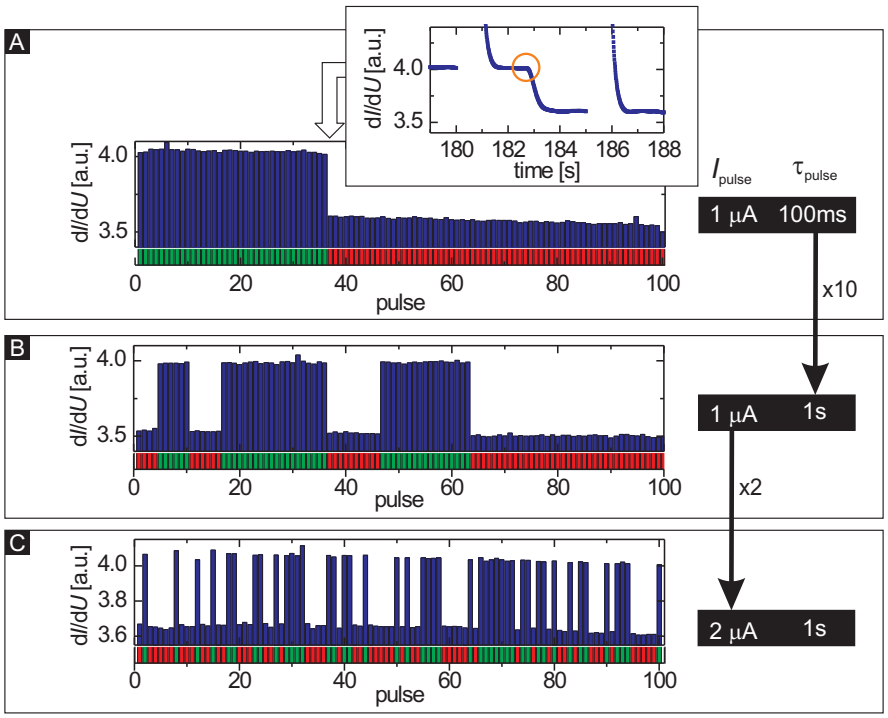

Figure 8.5: Current pulse experiments on island α with variation in pulse length τ_{pulse} and pulse height I_{pulse} ($U_{\mathrm{bias}} = -200\,\mathrm{mV}$, $I_{\mathrm{obs}} = 20\,\mathrm{nA}$). (**A**) Cross sectional view of $\mathrm{d}I/\mathrm{d}U$ signal $t = 5\,\mathrm{s}$ after pulse applications with $I_{\mathrm{pulse}} = 1\,\mu\mathrm{A}$ and $\tau_{\mathrm{pulse}} = 100\,\mathrm{ms}$. The resulting magnetization states are marked by red and green bars beneath. The only switching event observed occurred in-between two pulse applications (marked by the orange circle). (**B**) Enlarging the pulse length to $\tau_{\mathrm{pulse}} = 1\,\mathrm{s}$ led to six pulse triggered switching events. (**C**) Increasing the pulse height to $I_{\mathrm{pulse}} = 2\,\mu\mathrm{A}$ led to a significant rise in switching events.

result can be seen in Fig. 8.5 (A). The magnetization direction changed only once. A closer look reveals that this switching event occurred *in between* two pulse applications. Since the tunnel current was at a low value during this event ($I_{\mathrm{obs}} = 20\,\mathrm{nA}$), effects of spin torque and Joule heating can be neglected and this switching is one of the seldom occurring, purely thermally activated ones. Thus no pulse triggered switching event is observed ($p = 0$). Obviously, the effective energy barrier modification at these pulse parameters is not sufficient to achieve magnetization reversal.

In a second experiment, the pulse length was increased to $\tau_{\mathrm{pulse}} = 1\,\mathrm{s}$ (Fig. 8.5 (B)). Now six switching events are recorded. A cross-check of the data reveals that these events were not thermally induced as seen before. Six pulse applications led to magnetization reversal, and a statistical analysis of the switching probabilities yields $p_{\downarrow} = 0.07$ and $p_{\uparrow} = 0.15$. The mean lifetime of the otherwise quasistable states is reduced by the pulse triggered energy barrier modification to the order of seconds.

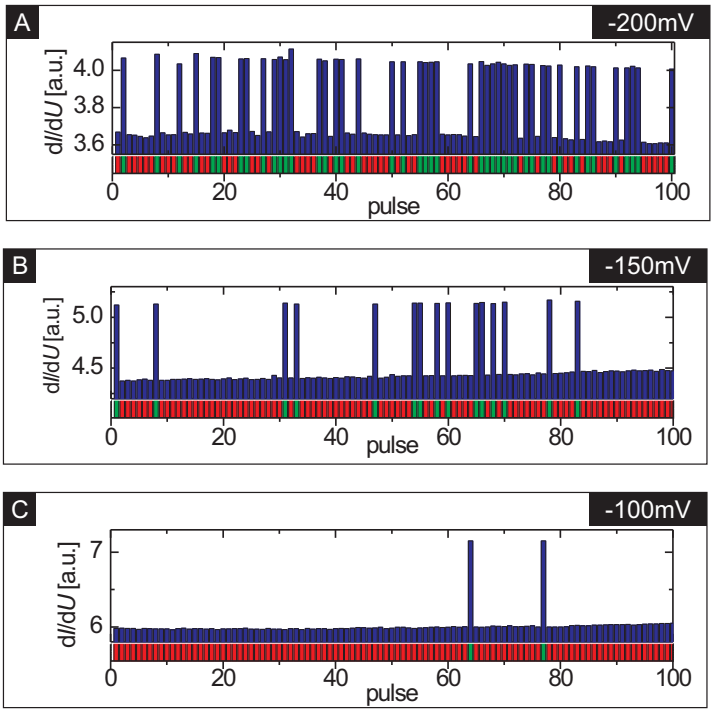

Figure 8.6: Current pulse experiments on island α with variation in bias voltage U_{bias} ($I_{\mathrm{obs}} = 20\,\mathrm{nA}$, $I_{\mathrm{pulse}} = 2\,\mu\mathrm{A}$, $\tau_{\mathrm{pulse}} = 1\,\mathrm{s}$). (**A**) Switching events between both magnetization states are observed frequently for $U_{\mathrm{bias}} = -200\,\mathrm{mV}$. An imbalance evolves going over $U_{\mathrm{bias}} = -150\,\mathrm{mV}$ (**B**) to $U_{\mathrm{bias}} = -100\,\mathrm{mV}$ (**C**): pulses to switch from state "1" to "0" become more efficient than before whereas switching attempts from "0" to "1" become less efficient.

Since spin torque and Joule heating have been shown to scale with the current, the pulse amplitude was doubled to $I_{\mathrm{pulse}} = 2\,\mu\mathrm{A}$ in the next step to increase the number of switching events (Fig. 8.5 (C)). This time an even more distinct change is observed: for 100 pulse applications 47 switching events can be observed in total with $p_{\downarrow} = 0.52$ and $p_{\uparrow} = 0.44$. This parameter combination works very reliably in comparison to the two before - in average nearly every second pulse application successfully led to magnetization reversal. Pulse length and amplitude are obviously crucial parameters to achieve pulse triggered switching events and an appropriate combination of both is essential for success.

In the experiments shown so far pulse length and height were varied at a constant bias voltage. To investigate the role of bias voltage, additional pulse experiments were performed keeping pulse height and length constant at $I_{\mathrm{pulse}} = 2\,\mu\mathrm{A}$ and $\tau_{\mathrm{pulse}} = 1\,\mathrm{s}$ and varying the bias voltage U_{bias} between $-200\,\mathrm{mV}$ and $-100\,\mathrm{mV}$. For a direct comparison Fig. 8.6 (A) again shows the results obtained for $U_{\mathrm{bias}} = -200\,\mathrm{mV}$ (same as Fig. 8.5 (C)). The magnetization is frequently switched between the two states and for both switching directions a high switching probability is observed ($p_{\downarrow} = 0.52$ and $p_{\uparrow} = 0.44$). Lowering the bias voltage to $U_{\mathrm{bias}} = -150\,\mathrm{mV}$ leads to fewer switching events (Fig. 8.6 (B)). In total 25 magnetization reversals are recorded. In contrast to the previous case, an imbalance for the two switching directions is observed: Whereas on average six pulse

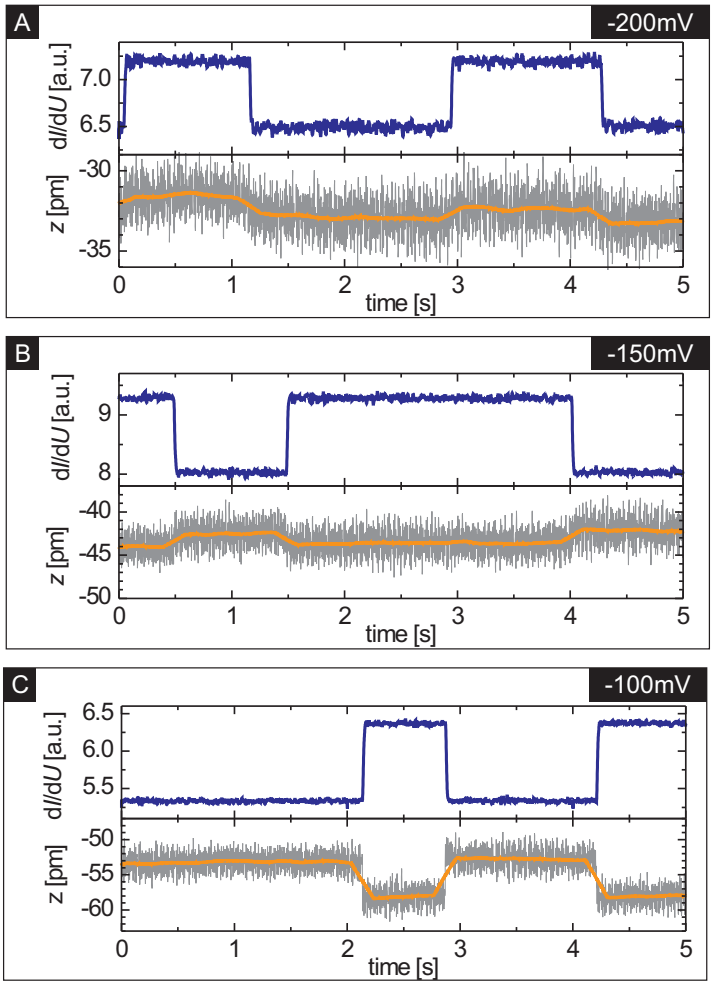

Figure 8.7: $\mathrm{d}I/\mathrm{d}U$ and z signal at different bias voltages U_{bias} recorded on the thermally switching island β (see Fig. 8.2(B)) as a function of time ($I = 2\,\mathrm{nA}$).
(**A**) With $U_{\mathrm{bias}} = 200\,\mathrm{mV}$ the z signal is switching with $\Delta z \approx 1\,\mathrm{pm}$.
(**B**) At $U_{\mathrm{bias}} = 150\,\mathrm{mV}$ Δz increases slightly to $\Delta z \approx 2\,\mathrm{pm}$.
(**C**) At $U_{\mathrm{bias}} = 100\,\mathrm{mV}$ Δz has reached $\Delta z \approx 5\,\mathrm{pm}$.

applications are necessary to switch the island $\uparrow$ ($p_\uparrow = 0.17$), only one to two pulses are sufficient to revert the island's magnetization again $\downarrow$ ($p_\downarrow = 0.87$). This imbalance becomes even stronger when decreasing the bias voltage further to $U_{\mathrm{bias}} = -100\,\mathrm{mV}$ (Fig. 8.6 (C)): Only two of the 98 pulses applied to switch the island $\uparrow$ were successful ($p_\uparrow = 0.02$). In both cases the magnetization was immediately switched back $\downarrow$ by the subsequent pulse ($p_\downarrow = 1$). Apparently the bias voltage chosen for pulse application plays a crucial role and determines whether the switching efficiency for both switching directions is balanced, i.e. equally probable, or not.

The fact that an increase in pulse length τ_{pulse} and pulse height I_{pulse} leads to a general increase of the switching probability is already quite intuitive: To achieve pulse-triggered switching events, the pulse length τ_{pulse} has to reach the order of the lifetime, that is drastically shortened during the high current injection. This

threshold is reached for the given island when setting the pulse length to 1 s. Further, in the last section it was shown that the spin torque scales linearly with the tunnel current. Therefore, an efficiency increase with pulse amplitude I_{pulse} is expected, too. But how is the bias-dependency explained?
To answer this question, the same tip was positioned on the neighboring, thermally switching island (island β in Fig. 8.2). The same bias voltages as before were chosen, and $\mathrm{d}I/\mathrm{d}U$ and z signal were recorded simultaneously at a low tunnel current $I = 2\,\mathrm{nA}$. Figure 8.7 shows sections of the telegraph noise traces recorded at the respective bias voltages. The recorded z signal exhibits the same telegraphic changes as the corresponding $\mathrm{d}I/\mathrm{d}U$ trace. Furthermore, the jump heights Δz in the z signal change with applied bias voltage: Whereas $\Delta z \approx 1\,\mathrm{pm}$ at $U_{\mathrm{bias}} = -200\,\mathrm{mV}$ (A), it increases slightly to $\Delta z \approx 2\,\mathrm{pm}$ at $U_{\mathrm{bias}} = -150\,\mathrm{mV}$ (B) and exhibits a value of $\Delta z \approx 5\,\mathrm{pm}$ at $U_{\mathrm{bias}} = -100\,\mathrm{mV}$ (C). This finding reflects a considerable difference in the total current polarization at the three bias voltages (see chapter 2.4) and explains the results from the bias dependent current pulse experiments performed on island α. The spin-transfer torque depends on the total current polarization (see chapter 3.3) that is changed with bias voltage. The higher Δz, the higher the total current polarization that gives rise to an elevated spin-transfer torque favoring one switching direction. Since the total polarization is small at $U_{\mathrm{bias}} = -200\,\mathrm{mV}$, the switching events observed here are taken to be mostly driven by Joule heating. This is in accordance with the nearly equal switching probabilities p for the two switching directions in the experiments performed at $U_{\mathrm{bias}} = -200\,\mathrm{mV}$. The effective energy barrier modification by the exerted spin torque ΔE_{ST} is small at this voltage, but the Joule heating is sufficiently high to overcome the effective energy barrier for switching in both directions. Increasing the polarization when going to $U_{\mathrm{bias}} = -100\,\mathrm{mV}$ leads to an elevated spin torque favoring one switching direction against the other, thereby splitting the switching efficiency for switching $\uparrow$ and $\downarrow$.

Summary

The switching probabilities found for the different pulse parameters are summarized in Fig. 8.8. The following trends can be observed: Starting with a pulse amplitude $I_{\mathrm{pulse}} = 1\,\mu\mathrm{A}$ at pulse length of $\tau_{\mathrm{pulse}} = 100\,\mathrm{ms}$ ($U_{\mathrm{bias}} = -200\,\mathrm{mV}$), no pulse-triggered event is found. Increasing the pulse length to $\tau_{\mathrm{pulse}} = 1\,\mathrm{s}$ leads to first pulse-triggered switching events (region I). The pulse length τ_{pulse} has reached the order of the shortened lifetime of the island's magnetization. When doubling the pulse amplitude to $I_{\mathrm{pulse}} = 2\,\mu\mathrm{A}$ the switching probability p drastically increases for both the $\uparrow$ and $\downarrow$ direction (region II) and achieves values around $p \approx 0.5$. This finding qualitatively fits into the results found before: spin torque and Joule heating acting on one island both increase with the injected current amplitude (chapter 7). Since switching occurs in both directions with

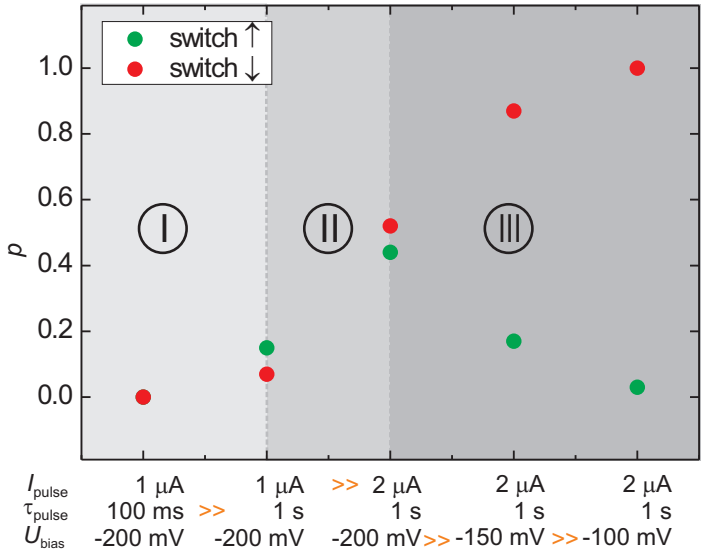

Figure 8.8: Switching probability p as a function of current pulse parameters. An increase in pulse length τ_{pulse} (I) and pulse height I_{pulse} (II) leads to a general increase in switching probability. The balance between the two switching directions ↑ and ↓ changes with the applied bias voltage U_{bias} (III).

nearly equal probability, Joule heating is taken to be the predominant driving force for magnetization reversal here. Changing the bias voltage U_{bias} affects the switching probability, too: Decreasing the bias voltage from $U_{\mathrm{bias}} = -200\,\mathrm{mV}$ to $U_{\mathrm{bias}} = -100\,\mathrm{mV}$ (region III) results in a considerable splitting of the switching probability for the two directions. Whereas the switching efficiency for switching ↓ increases further and reaches $p_{\downarrow} = 1$ at $U_{\mathrm{bias}} = -100\,\mathrm{mV}$, the efficiency for the other switching direction drastically decreases to $p_{\uparrow} = 0.02$. Characterizing the total current polarization as a function of bias voltage for this particular tip by monitoring the Δz signal changes of thermally induced switching events reveals that the polarization decreases when decreasing the bias voltage from $U_{\mathrm{bias}} = -200\,\mathrm{mV}$ to $U_{\mathrm{bias}} = -100\,\mathrm{mV}$. The total polarization at the applied bias voltage is found to be a measure for the spin torque acting during the pulse: The bigger the polarization of the current, the bigger the spin torque becomes, and the more one switching direction is preferred against the other.

8.2 Current pulses at alternating polarity

The current pulse experiments presented so far were realized at fixed bias polarity. In the previously described experiments on thermally activated islands, it was shown that the spin torque changes its sign when reversing the bias polarity. The question arises whether this can be utilized to achieve reversible magnetization switching by alternating pulse polarity, i.e. one pulse polarity should switch forward and the other one switch back.

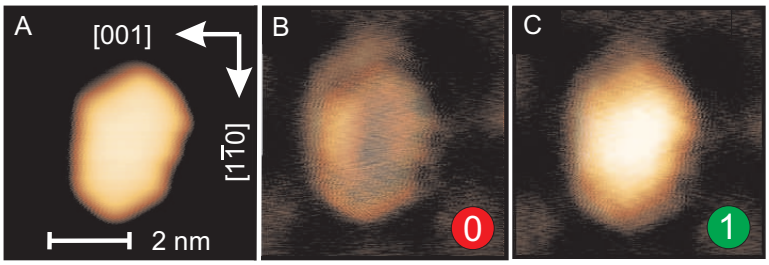

Figure 8.9: Current pulse experiments on a Fe ML nanoisland on W(110). (**A**) A topography image of the nanoisland under investigation ($I_{\mathrm{obs}} = 20\,\mathrm{nA}$, $U_{\mathrm{bias}} = +180\,\mathrm{mV}$, $T = 30.9\,\mathrm{K}$). The two $\mathrm{d}I/\mathrm{d}U$ maps show the two stable magnetic states of the nanoisland, state "0" (**B**) and "1" (**C**).

Concept

For these experiments, a quasistable nanoisland with a mean lifetime of $\bar{\tau} \approx 30$ minutes was chosen. Figure 8.9 shows a topography image of the island under investigation and two $\mathrm{d}I/\mathrm{d}U$ maps of its two magnetization states "0" and "1", respectively. The procedural methods as described in section 8.1 were applied: The tip is stabilized at a low tunnel current above the island's center, and high current pulses are applied by means of programmed command sequences. To switch the magnetization controllably and reversibly back and forth, the current polarity is chosen depending on the respective state of the nanoisland. Figure 8.10 shows the $\mathrm{d}I/\mathrm{d}U$ signal as a function of time t for two pulse applications. For the nanoisland in state "0" a pulse at $U_{\mathrm{bias}} = +180\,\mathrm{mV}$ is applied (A). The $\mathrm{d}I/\mathrm{d}U$ signal returns after the pulse application to a high signal level: the magnetization direction has changed pulse-triggered to state "1". For the island being in magnetization state "1", the current pulse direction is reversed by choosing a bias of $U_{\mathrm{bias}} = -180\,\mathrm{mV}$ for the pulse application (B). This current pulse leads to an inverted switching event: The magnetization changes now pulse-triggered from state "1" back to state "0". Thus the concept of switching back and forth at alternating pulse polarity succeeds.

To allow for a statistical analysis of the switching probability as a function of the pulse parameter, several pulse applications are carried out at different parameters. Again, intervals of five seconds were chosen for the pulse application. As before, the probability p to switch the magnetization with one pulse, defined by the ratio of pulse-triggered events and total number of applied pulses

$$p = \frac{n_{\mathrm{switch}}}{n_{\mathrm{pulse}}} \quad ,$$

is calculated from the experiments. Both switching directions $\uparrow$ (state "0" to state "1") and $\downarrow$ ("1" to "0") are thereby evaluated independently.

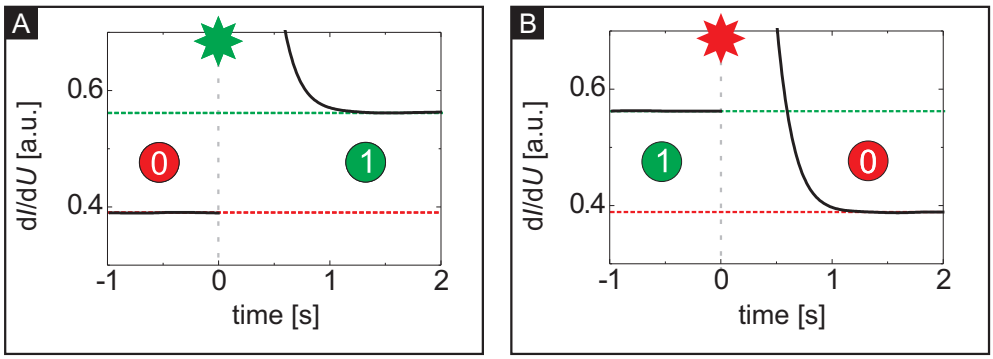

Figure 8.10: Current pulse experiments on a Fe ML nanoisland. The $\mathrm{d}I/\mathrm{d}U$ signal is shown as a function of time t for two pulsing experiments with opposite pulse polarities ($I_{\mathrm{pulse}} = 1.6\,\mu\mathrm{A}$, $I_{\mathrm{obs}} = 20\,\mathrm{nA}$, $U_{\mathrm{bias}} = \pm 180\,\mathrm{mV}$): (**A**) If the island is in state "0", a positive pulse polarity is chosen (green asterisk) to switch ↑ to state "1". (**B**) A reversed pulse polarity is chosen (red asterisk) to switch the island from "1" to "0" (↓). After each pulse the $\mathrm{d}I/\mathrm{d}U$ signal drops from saturation to state "1" or "0" level indicating the nanoisland's magnetization state after the respective pulse.

Experimental results

Figure 8.11 shows the resultant evolution of the magnetization with varying pulse length τ_{pulse} while keeping the pulse amplitude of $I_{\mathrm{pulse}} = 1.6\,\mu\mathrm{A}$ constant. For a compact illustration the results are displayed as introduced before (see page 68): The $\mathrm{d}I/\mathrm{d}U$ signal is read out prior to each pulse and shown as a bar diagram. Red and green color bars beneath indicate the respective magnetization state. A regular pattern of alternating high and low $\mathrm{d}I/\mathrm{d}U$ signal levels is therefore desired, because then every pulse application leads to magnetization reversal. In the color-coded read out beneath, the green and red bars would then alternate with every pulse. Therefore, consecutive bars of the same $\mathrm{d}I/\mathrm{d}U$ level or color indicate unsuccessful switching attempts. At a pulse length $\tau_{\mathrm{pulse}} = 50\,\mathrm{ms}$ (A) the $\mathrm{d}I/\mathrm{d}U$ bar pattern looks irregular. A closer look reveals that the positive pulses to switch ↑ worked quite reliably (nearly every red bar is directly followed by a green one), but switching ↓ needed in the most cases multiple pulse applications at negative polarity to succeed, as indicated by several consecutive green bars. The statistical analysis yields the switching probabilities $p_{\uparrow} = 0.95$ and $p_{\downarrow} = 0.35$. The efficiency of the pulse applications increases with a doubled pulse length ($\tau_{\mathrm{pulse}} = 100\,\mathrm{ms}$, (B)), recognized by the improved regularity of alternating $\mathrm{d}I/\mathrm{d}U$ levels: every switching attempt ↑ is now successful ($p_{\uparrow} = 1$), and switching ↓ is achieved in most cases by only one to two pulse applications (smaller blocks of green bars, $p_{\downarrow} = 0.76$). The $\mathrm{d}I/\mathrm{d}U$ signal level five seconds after pulse no. 61 is between the two signal levels of state "0" and state "1". The reason can be seen in the inset

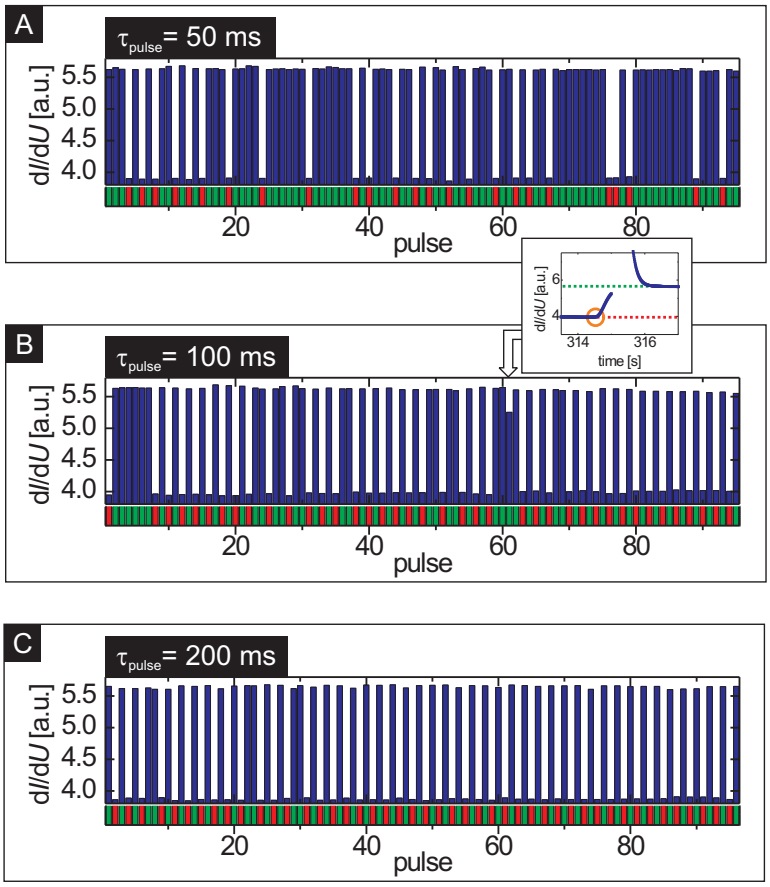

Figure 8.11: Results for current pulse experiments at alternating bias on the Fe ML nanoisland shown in Fig. 8.9: Cross sectional view of $\mathrm{d}I/\mathrm{d}U$ signal $t = 5\,\mathrm{s}$ after pulse applications at different pulse lengths τ_{pulse} ($I_{\mathrm{pulse}} = 1.6\,\mu\mathrm{A}$, $I_{\mathrm{obs}} = 20\,\mathrm{nA}$, $U_{\mathrm{bias}} = \pm 180\,\mathrm{mV}$). The inset in (**B**) shows a $\mathrm{d}I/\mathrm{d}U$ signal change due to a thermally induced switching event (orange circle) causing an ambiguous $\mathrm{d}I/\mathrm{d}U$ signal level in the bar diagram at the respective time.

where the $\mathrm{d}I/\mathrm{d}U$ signal is shown as a function of time for the relevant section: a thermally induced switching event occurred and the $\mathrm{d}I/\mathrm{d}U$ signal was changing from the low to the high level at the time of signal readout. Therefore this event was not pulse-triggered. Finally, pulse widths of $\tau_{\mathrm{pulse}} = 200\,\mathrm{ms}$ lead to a nearly perfect comb-like $\mathrm{d}I/\mathrm{d}U$ bar pattern (C). In the color-coded representation every red bar is followed by a green one, and vice versa holds for the most cases, too, indicating that the island is reliably switched for both transitions. The switching probabilities are $p_{\uparrow} = 1$ and $p_{\downarrow} = 0.95$, respectively.

Cross check with counter experiments

The question arises whether the events occur only due to the Joule heating of the island during the pulse: the overall power delivered to the island increases with pulse length. This could already lead to switching, independently of the current polarization. To exclude this possibility, pulses with the opposite polarity required to switch the island were applied. None of the pulses in this counter experiment ($I_{\mathrm{pulse}} = 1.6\,\mu\mathrm{A}$, $\tau_{\mathrm{pulse}} = 200\,\mathrm{ms}$, 100 pulses for each configuration) led to a magnetization reversal. The effective Joule heating remains constant, since

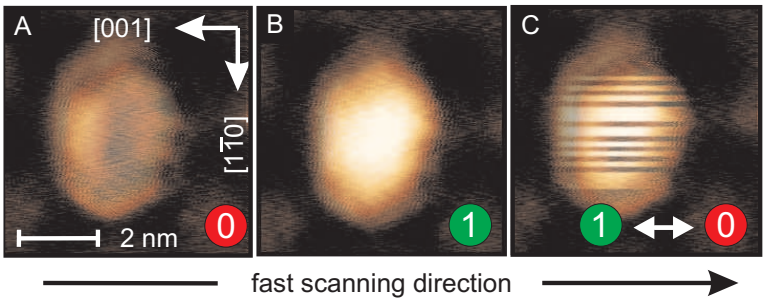

Figure 8.12: Nanoisland under investigation ($I_{\mathrm{obs}} = 20\,\mathrm{nA}$, $U_{\mathrm{bias}} = +180\,\mathrm{mV}$, $T = 30.9\,\mathrm{K}$). The first two $\mathrm{d}I/\mathrm{d}U$ maps show the nanoisland being in magnetization state "0" (**A**) and "1" (**B**), respectively. If current pulses are applied during the scanning procedure, the island appears striped (**C**). $\tau_{\mathrm{pulse}} = 100\,\mathrm{ms}$, $I_{\mathrm{pulse}} = 1.6\,\mu\mathrm{A}$, $U_{\mathrm{pulse}} = \pm 180\,\mathrm{mV}$.

the total current is preserved. Consequently, the spin torque is the driving force for the magnetization reversal.

Pulse application during scanning procedure

The current pulse experiments shown so far were performed while keeping the STM tip stationary above the island's center. Command sequences can be executed during a scanning procedure, too. Scanning is then interrupted, the tip is moved to the chosen site, a pulse executed, and the scanning procedure is resumed. Figure 8.12 shows three $\mathrm{d}I/\mathrm{d}U$ maps of the nanoisland utilized for the presented experiments: (A) and (B) show the island in its stable magnetic states "0" and "1", respectively. For the last $\mathrm{d}I/\mathrm{d}U$ map the image was paused after every 20th scan line, the tip was moved to the island's center, and a pulse was applied. Again, the pulse polarity was chosen depending on the state of the island. The nanoisland now appears striped, indicating the particular scan lines the pulses were initiated. The appearance reminds one of the thermally switching islands in chapter 6, but in contrast to the case of statistically occurring switching events, the magnetization here is switched at integer intervals of 10 scan lines. Unsuccessful switching attempts thereby led to three wider stripes in the $\mathrm{d}I/\mathrm{d}U$ map (C).

Quantification of spin torque and Joule heating

In the following, both spin torque and Joule heating will be roughly quantified by an analysis of the switching statistics. For the negative pulse polarity the probability $p_{\uparrow}$ ($p_{\downarrow}$) to switch the magnetization $\uparrow$ ($\downarrow$) within a pulse length τ_{pulse} is given by

$$p_{\uparrow,\downarrow}(\tau_{\mathrm{pulse}}) = 1 - \exp\left[-\frac{\tau_{\mathrm{pulse}}}{\bar{\tau}_{0,1}(I_{\mathrm{pulse}})}\right] \quad . \tag{8.2}$$

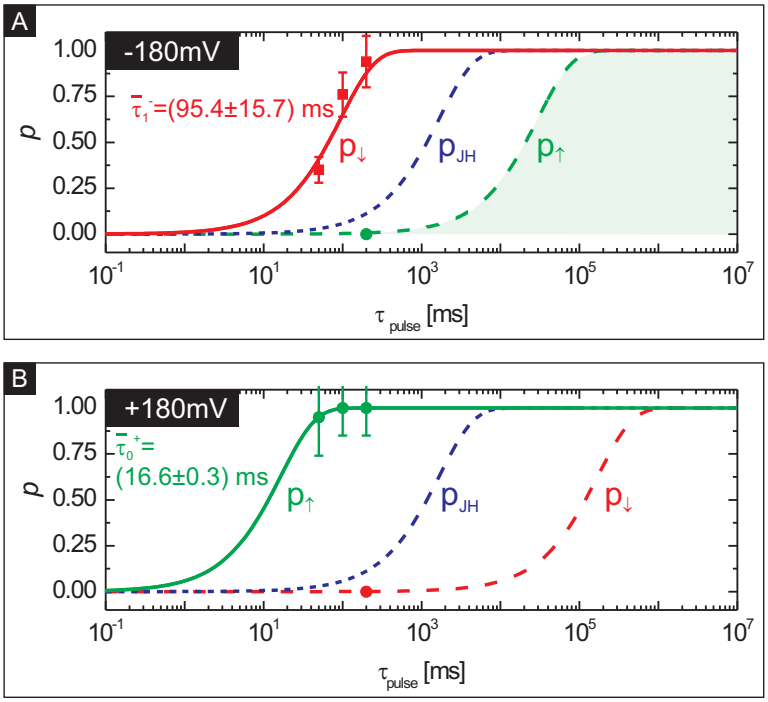

Figure 8.13: Switching probability p to switch the magnetization with one pulse ($I_{\mathrm{pulse}} = 1.6\,\mu\mathrm{A}$) as a function of the pulse length τ_{pulse} for negative (**A**) and positive (**B**) pulse bias. $p_{\uparrow,\downarrow}$ designate the cases where spin torque favors or hinders magnetization reversal, and p_{JH} designates the probability, if only Joule heating was acting. Data points mark results from the measurement, continuous line directly fitted curves (Eq. (8.2)), and dashed lines designate the curves for the calculated boundary values of c_{JH} and c_{ST}. See text for details.

$\bar{\tau}_{0,1}$ denotes the mean lifetime during the current pulse, affected by Joule heating and spin torque (see Eq. 7.3):

$$\bar{\tau}_{0,1}(I_{\mathrm{pulse}}) = \nu_0^{-1} \cdot \exp\left[\frac{E_{\mathrm{b}} \pm \Delta E_{\mathrm{ST}}}{k_{\mathrm{B}}(T + \Delta T_{\mathrm{JH}})}\right] = \nu_0^{-1} \cdot \exp\left[\frac{E_{\mathrm{b}} \pm c_{\mathrm{ST}} I_{\mathrm{pulse}}}{k_{\mathrm{B}}(T + c_{\mathrm{JH}} I_{\mathrm{pulse}})}\right] \quad . \tag{8.3}$$

c_{JH} is the Joule heating coefficient which gives the temperature change per unit current, and c_{ST} is the spin torque coefficient giving the effective energy barrier change per unit current (see section 7.2). The notation in Equation (8.3) also holds for negative pulse bias where switching $\downarrow$ is favored in the experiment. The exerted spin torque lowers the effective energy barrier for state "1" and therefore its mean lifetime. For state "0" the effective energy barrier and the lifetime are increased. At positive pulse polarity, the situation is reversed and switching $\uparrow$ is favored. Therefore state "0" and "1" have to be exchanged in Equation (8.3). However, a special case occurs if only Joule heating is acting. Then $c_{\mathrm{ST}} = 0$, and the equation reduces to

$$\bar{\tau}_{\mathrm{JH}}(I_{\mathrm{pulse}}) = \nu_0^{-1} \cdot \exp\left[\frac{E_{\mathrm{b}}}{k_{\mathrm{B}}(T + c_{\mathrm{JH}} I_{\mathrm{pulse}})}\right] \quad . \tag{8.4}$$

The lifetimes for both states here are only reduced by Joule heating. Note, that

$$\bar{\tau}_{\mathrm{JH}}(I_{\mathrm{pulse}}) = \sqrt{\bar{\tau}_0(I_{\mathrm{pulse}}) \cdot \bar{\tau}_1(I_{\mathrm{pulse}})} \quad . \tag{8.5}$$

To summarize, the switching probability p can be classified into three cases (again in the notation for a negative pulse bias):

- $p_\downarrow$: *The spin torque favors switching* $\downarrow$ by lowering the effective energy barrier for state "1" by ΔE_{ST}. The *combined* action of Joule heating *and* spin torque leads to a decrease in the mean lifetime $\bar{\tau}_1$ for state "1". In the experiment, this situation is utilized to achieve pulse-triggered switching events.

- $p_\uparrow$: *The spin torque hinders switching* $\uparrow$ by increasing the effective energy barrier for state "0" by ΔE_{ST} in contrast to the Joule heating which decreases the effective barrier. Therefore, state "0" exhibits a longer lifetime than state "1" ($\bar{\tau}_0 > \bar{\tau}_1$), and increased pulse lengths are necessary for magnetization reversal ($p_\uparrow(\tau_{\mathrm{pulse}}) < p_\downarrow(\tau_{\mathrm{pulse}})$). This situation occurred in the counter experiments.

- p_{JH}: *The spin torque is neglected* ($c_{\mathrm{ST}} = 0$) and only a Joule heating considered. The effective barrier would be equally reduced for both states by the Joule heating only. The mean lifetime $\bar{\tau}_{\mathrm{JH}}$ would then be $\bar{\tau}_1 < \bar{\tau}_{\mathrm{JH}} < \bar{\tau}_0$, and the probability to switch with one pulse p_{JH} would be independent from the switching direction. Although this situation did not occur in the experiments of this section, the consideration of this case will help us in the following discussion.

Again, the same holds for the reversed pulse polarity when exchanging $\uparrow$ with $\downarrow$, and "0" with "1". The island under investigation has comparable dimensions as island no. 1 in chapter 6, therefore energy barrier E_{b} and attempt frequency ν_0 are taken to be the same. Now we will successively combine the measurement results with the relations (8.2) to (8.5) to determine c_{JH} and c_{ST} for both bias polarities. We start with the measurements at negative bias voltage (Fig. 8.13 (A)):

1. The switching probabilities $p_\downarrow$ are determined from the experiment (red data points).

2. Fitting Eq. (8.2) to this data yields the mean lifetime of state "1" $\bar{\tau}_1 = (95.4 \pm 15.7)\,\mathrm{ms}$ (red, solid curve). The lifetime of state "1" is lowered by Joule heating *and* spin torque (case 1 from the list above).

3. The counter experiment yields $p_\uparrow(200\,\mathrm{ms}) = 0$ (green data point). This data point gives a lower boundary for $p_\uparrow$ (case 2), symbolized by the green area in the graph: Since no switching event has been observed, the mean lifetime of state "0" has to be considerably higher than the pulse length $\tau_{\mathrm{pulse}} = 200\,\mathrm{ms}$.

4. We position the curve for $p_\uparrow(\tau_{\mathrm{pulse}})$ according to Eq. (8.2) such that $p_\uparrow$ rises at slightly higher values of $\tau_{\mathrm{pulse}} = 200\,\mathrm{ms}$ (green, dashed curve). With this graphical estimation we find a lower boundary for the lifetime of state "0": $\bar{\tau}_0 \geq (30 \pm 5)\,\mathrm{s}$.

5. Knowing $\bar{\tau}_1$ and $\bar{\tau}_0$, we can calculate the mean lifetime for the case if Joule heating was neglected. Inserting both values in Equation (8.5) yields $\bar{\tau}_{\mathrm{JH}} \geq (1.7 \pm 0.8)\,\mathrm{s}$. The resulting switching probability $p_{\mathrm{JH}}(\tau_{\mathrm{pulse}})$ is plotted as a blue, dashed line (case 3).

6. With the help of Eq. (8.4) we can now determine the Joule heating coefficient from the lifetime $\bar{\tau}_{\mathrm{JH}}$:
$$c_{\mathrm{JH}} \leq (5.1 \pm 0.4)\frac{\mathrm{K}}{\mu\mathrm{A}} \quad .$$

7. The spin torque coefficient c_{ST} can be determined by Formula (8.3). Inserting $\bar{\tau}_1$ and c_{JH} yields
$$c_{\mathrm{ST}}^{-} \geq (6.0 \pm 3.5)\frac{\mathrm{meV}}{\mu\mathrm{A}} \quad .$$

This procedure can be shortened for the experiments at positive pulse polarity (Fig. 8.13 (B)). The first two steps are analogous:

1. From the experiment the switching probabilities $p_{\downarrow}$ are determined (green data points). Here, switching from state "0" to state "1" is favored by the spin torque (case 1).

2. Fitting Eq. (8.2) to the data yields a mean lifetime of $\bar{\tau}_0 = (16.6 \pm 0.3)\,\mathrm{ms}$ for state "0" (green, solid curve).

3. Since the Joule heating is independent of the current direction, we can use now the Joule heating coefficient c_{JH} determined for negative pulse polarity. Again, $\bar{\tau}_0$ and c_{JH} are inserted into Eq. (8.3). As a result, we find at positive bias voltage
$$c_{\mathrm{ST}}^{+} \geq (9.7 \pm 3.3)\frac{\mathrm{meV}}{\mu\mathrm{A}} \quad .$$

The coefficients c_{ST}^{+} and c_{JH} yield $p_{\downarrow}(\tau_{\mathrm{pulse}})$ and $p_{\mathrm{JH}}(\tau_{\mathrm{pulse}})$ for the two other cases, too (dashed curves in Fig. 8.13 (B)). The data point of the counter experiment $p_{\downarrow}(200\,\mathrm{ms}) = 0$ (red) correctly lies on the $p_{\downarrow}(\tau_{\mathrm{pulse}})$ curve.

In order to investigate the impact of pulse amplitude, current pulse experiments were performed with varying pulse amplitude I_{pulse} at a constant pulse length $\tau_{\mathrm{pulse}} = 100\,\mathrm{ms}$. Figure 8.14 shows the resulting switching probabilities $p(I_{\mathrm{pulse}})$ for $I_{\mathrm{pulse}} = 1.0\,\mu\mathrm{A}$, $1.4\,\mu\mathrm{A}$ and $1.6\,\mu\mathrm{A}$ for both pulse polarities. Red and green data points depict the probabilities determined from the experiment. A general increase of $p(I_{\mathrm{pulse}})$ can be observed as I_{pulse} is increased. Since no counter experiments have been performed for $\tau_{\mathrm{pulse}} = 100\,\mathrm{ms}$, the procedure to determine c_{ST} and c_{JH} must be altered here. This time we fit the switching probability given by Eq. (8.2) to the data, and by replacing the mean lifetime by expression (8.3) c_{ST} and c_{JH}

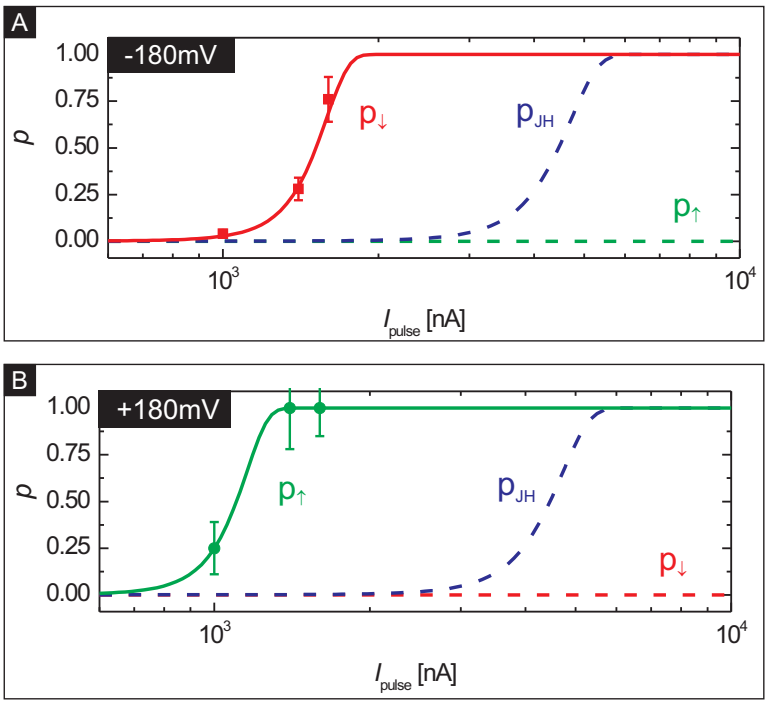

Figure 8.14: Switching probabilities $p_\downarrow$ and $p_\uparrow$ to switch the magnetization with one pulse as function of pulse amplitudes I_{pulse} for negative (A) and positive (B) pulse bias. Data points mark measurement results, continuous lines are fitted curves. The resulting fit parameters c_{ST} and c_{JH} are used to calculate the probability for the reversed switching and the case assuming only Joule heating, p_{JH} (dashed curves, see text for details).

become fit parameters. The previously determined bounds for c_{ST} and c_{JH} are incorporated into the fitting procedure, as well as the condition that c_{JH} must again be the same for both bias polarities. The resulting curves, $p_\downarrow$ at negative pulse bias, $p_\uparrow$ at positive, are plotted as continuous lines in Figure 8.14. From the fit we obtain the Joule heating coefficient

$$c_{\text{JH}} = 2.6 \pm 2.9 \frac{\text{K}}{\mu\text{A}} \quad ,$$

and the spin torque coefficient at negative and positive bias

$$c_{\text{ST}}^{-} = 11.9 \pm 7.0 \frac{\text{meV}}{\mu\text{A}} \quad ,$$

$$c_{\text{ST}}^{+} = 18.6 \pm 7.1 \frac{\text{meV}}{\mu\text{A}} \quad .$$

From this we can calculate the switching probabilities for the two other cases, namely switching without and switching against the spin torque. The results are plotted as dashed curves in Fig. 8.14.

8.3 Considerations for experimental optimization

The question arises whether there is a way to optimize pulse length τ_{pulse} and current amplitude I_{pulse} to achieve the desired switching events at minimal efforts.

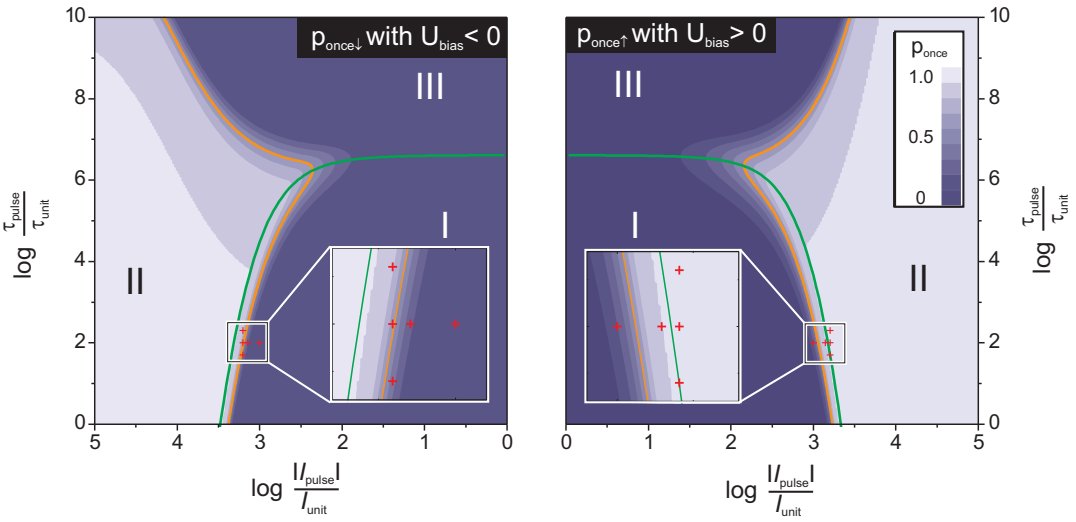

Figure 8.15: Switching probabilities $p_{\mathrm{once}\uparrow}$ and $p_{\mathrm{once}\downarrow}$ in contour plots as function of pulse length τ_{pulse} and amplitude I_{pulse} for the two bias polarities ($\tau_{\mathrm{unit}} = 1\,\mathrm{ms}$, $I_{\mathrm{unit}} = 1\,\mathrm{nA}$). Red crosses mark the experiment parameters used. Orange lines mark the level where $p_{\mathrm{once}} = p_{\mathrm{thre}} = 1 - \frac{1}{e}$. See text for details.

If the pulse duration τ_{pulse} is chosen too long, one runs the risk of multiple switching events. To address these questions, the results of the last section (8.2) were analyzed in more detail using the following estimation.
A simple expression for the probability of switching only once, for instance $\uparrow$, as function of $p_\uparrow$ and $p_\downarrow$ has the following form

$$p_{\mathrm{once}\uparrow}(I_{\mathrm{pulse}}, \tau_{\mathrm{pulse}}) = p_\uparrow(I_{\mathrm{pulse}}, \tau_{\mathrm{pulse}}) - p_\downarrow(I_{\mathrm{pulse}}, \tau_{\mathrm{pulse}}) \tag{8.6}$$

$$= \exp\left[-\frac{\tau_{\mathrm{pulse}}}{\bar{\tau}_1(I_{\mathrm{pulse}})}\right] - \exp\left[-\frac{\tau_{\mathrm{pulse}}}{\bar{\tau}_0(I_{\mathrm{pulse}})}\right] \quad . \tag{8.7}$$

The value of $p_{\mathrm{once}\uparrow}$ is ≈ 0, if either the pulse is not high enough to achieve any switching event or switching back *and* forth is probable. Only the pulse parameters in between these two cases lead to probabilities $p_{\mathrm{once}} > 0$. Figure 8.15 shows double logarithmic contour plots of this function for the values found in the last section. The data points of the pulse experiments are marked by red crosses. Three regions can be roughly distinguished:

- Region I where p_{once} is low, because the combination of τ_{pulse} and I_{pulse} is not sufficient to achieve any switching: $p_\uparrow = 0$, $p_\uparrow = 0 \Rightarrow p_{\mathrm{once}} = 0$.

- Region II, marking favorable parameter combinations that with a high probability lead to the desired switching events without the reversed switching:

$$|p_\downarrow - p_\uparrow| = 1 \Rightarrow p_{\text{once}} = 1.$$

- Region III, designating pulse parameters to be prevented, because reversed switching is also probable: $p_\uparrow = 1$, $p_\uparrow = 1 \Rightarrow p_{\text{once}} = 0$.

A threshold between reliable and unreliable switching can be defined by

$$p_{\text{thre}}(I_{\text{pulse}}, \tau_{\text{pulse}}) = 1 - \frac{1}{e} \quad .$$

This level is marked in Figure 8.15 by an orange curve. Towards respectively lower values of I_{pulse}, p_{once} drops below the threshold and should therefore be avoided if reliable switching is desired. The green curves here mark the pulse parameter combinations of τ_{pulse} and I_{pulse} that lead to the highest possible values of p_{once} for a given pulse amplitude I_{pulse}. This holds for the combinations of I_{pulse} and τ_{pulse}, where

$$\left| \frac{\partial p_{\text{once}}(I_{\text{pulse}}, \tau_{\text{pulse}})}{\partial \tau_{\text{pulse}}} \right|_{I_{\text{pulse}}} = 0 \tag{8.8}$$

$$\Rightarrow \tau_{\text{pulse}} = \quad \log \left[\frac{\bar{\tau}_a(I_{\text{pulse}})}{\bar{\tau}_b(I_{\text{pulse}})} \right] \cdot \frac{\bar{\tau}_a(I_{\text{pulse}}) \cdot \bar{\tau}_b(I_{\text{pulse}})}{\bar{\tau}_a(I_{\text{pulse}}) - \bar{\tau}_b(I_{\text{pulse}})} \quad . \tag{8.9}$$

The indices a and b denote the two different magnetization states. At a positive bias $a = 0$, $b = 1$, and at a negative bias $a = 1$, $b = 0$. Therefore, the point of intersection of these two curves can be regarded as optimal parameter combination in terms of a minimum pulse amplitude for reliable switching. On the other hand, the writing time in technical applications is favored to be kept short: The steep diminution of the threshold curve below the intersection point shows that the pulse length necessary for switching can be shortened by many orders of magnitude when using only slightly higher pulse amplitudes.

8.4 Determination of critical switching currents

In order to determine the critical current necessary for magnetization reversal, experiments with triangular current sweeps were performed. The choice of the same tip and nanostructure as presented in section 8.2 will allow for a comparison of the results. As for the current pulse applications, the tip is kept stationary above the island's center and the current sweeps were performed automatically by a program script at a closed feedback loop. The tunnel current is increased or decreased stepwise by $\Delta I = 4\,\text{nA}$. A variation of sweep rate $\mathrm{d}I/\mathrm{d}t$ is realized by changing the time delay Δt between the current steps.

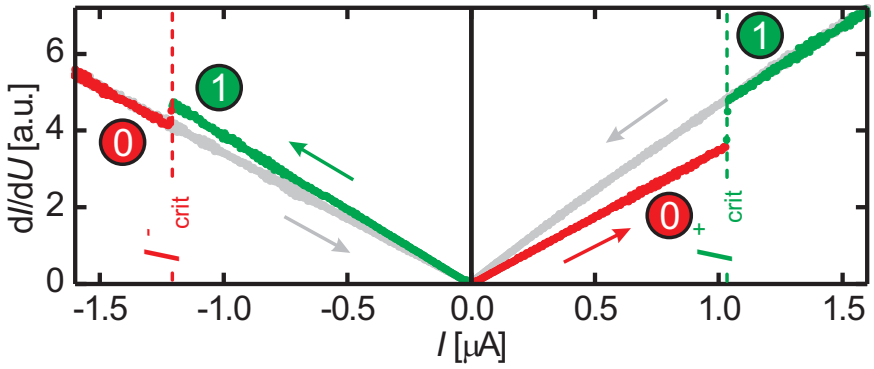

Figure 8.16: Switching the magnetization by increasing the tunnel current (sweep rate $\mathrm{d}I/\mathrm{d}t$ = 400 nA/s, $U_{\mathrm{bias}} = \pm 180$ mV, $T = 30.9$ K). Ramping the current at a positive bias (red arrow) forces the magnetization of the nanoisland to switch from state "0" to state "1" when exceeding a critical current I^{+}_{crit}. When ramping the current at a negative bias (green arrow) the magnetization of the nanoisland switches back from state "1" to state "0" at I^{-}_{crit}. Decreasing the current from high values back to zero leads to no reversal (gray line).

Figure 8.16 shows the $\mathrm{d}I/\mathrm{d}U$ signal as a function of current I for one current sweep at a sweeprate of $\mathrm{d}I/\mathrm{d}t = 400\,\mathrm{nA/s}$. Starting from a low current ($I = +20\,\mathrm{nA}$), the island remains in its initial state "0" until a critical current I^{+}_{crit} is reached and magnetization switching is triggered, as indicated by the jump in the $\mathrm{d}I/\mathrm{d}U(I)$ signal at I^{+}_{crit}. As shown in the section before, the spin torque exerted when injecting a high current at positive bias favors switching ↑ from state "0" to state "1". The current is ramped further up to $I = +1.6\,\mu\mathrm{A}$ before ramping it back to low values. No switching event is observed, the island remains in state "1". Ramping from $I = -20\,\mathrm{nA}$ to $I = -1.6\,\mu\mathrm{A}$ leads to a magnetization reversal from "1" to "0" at I^{-}_{crit}. Again the current ramped back without additional magnetization reversal. Obviously, the same holds here as for positive bias: The switching occurs into the state favored by the spin torque (here state "0"), but not back. By repeating the sweep 25 times we determined the mean critical currents $\overline{I}_{\mathrm{crit}}$ for switching back and forth, resulting in $\overline{I}^{+}_{\mathrm{crit}} = (1.0 \pm 0.1)\,\mu\mathrm{A}$ and $\overline{I}^{-}_{\mathrm{crit}} = (-1.2 \pm 0.2)\,\mu\mathrm{A}$. This procedure enables the determination of the critical current necessary for magnetization reversal directly from the experiment without making the detour over an extensive statistical analysis to determine spin torque and Joule heating coefficients. On the contrary, the investigation of the critical current will in the following discussion turn out to be an alternative way to determine the coefficients of spin torque and Joule heating.

We studied the critical current as a function of sweep rate. The experiment was repeated at different sweep rates $\mathrm{d}I/\mathrm{d}t$ ranging from 260 nA/s up to 1750 nA/s and the respective critical currents determined. The results are depicted in Fig. 8.17. A

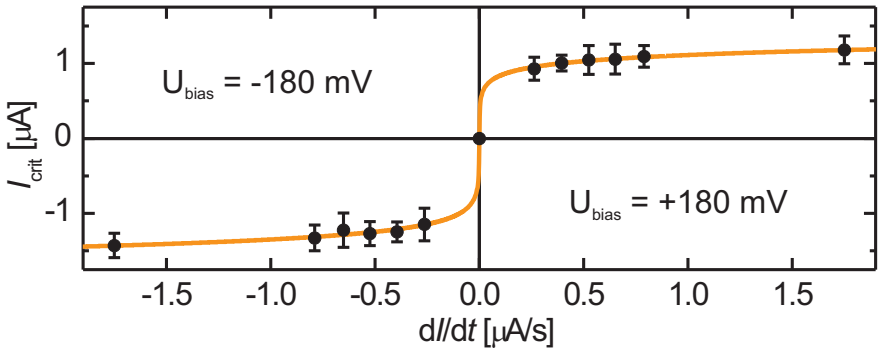

Figure 8.17: Critical current I_{crit} as a function of current sweeprate $\mathrm{d}I/\mathrm{d}t$ for both current polarities ($U_{\mathrm{bias}} = \pm 180\,\mathrm{mV}$, $T = 30.9\,\mathrm{K}$). Two fits result in curves superimposing another, depicted here in orange: Fitting with the conventional Kurkijärvi model as in Eq. (8.11) yields the fit parameters $I^{+}_{\mathrm{crit},0} = (3.96 \pm 0.04)\mu\mathrm{A}$ and $I^{-}_{\mathrm{crit},0} = (-4.90 \pm 0.05)\mu\mathrm{A}$. A fit with the extended Kurkijärvi model (Eq. (8.12)) gives $I^{+}_{\mathrm{crit},0} = (4.3 \pm 0.3)\mu\mathrm{A}$, $I^{-}_{\mathrm{crit},0} = (-5.4 \pm 0.4)\mu\mathrm{A}$ and $T_{\mathrm{eff}} = (31.8 \pm 0.6)\,\mathrm{K}$.

monotonic behavior can be observed: the critical current at which the magnetization direction is switched increases with increasing sweep rate. And, in agreement with the current pulse experiments of section 8.2, the positively biased current direction shows slightly lower critical currents than the negative one. However, here the injected current is varied with time at a constant rate. Consequently, the mean lifetime of a state becomes a function of the current rate, and therefore of time. To take the current sweep into account, we will make the ansatz to express the reduced lifetime at time t under the influence of a current ramp varied at the rate $\dot{I}$, as

$$\bar{\tau}(t) = \nu_0^{-1} \cdot \exp\left[\frac{E_{\mathrm{b}}}{k_{\mathrm{B}}T} \cdot \left(1 - \frac{\dot{I}t}{I_{\mathrm{crit},0}}\right)\right] \quad . \tag{8.10}$$

The original energy barrier E_{b} of the Arrhenius law is replaced by $E_{\mathrm{b}} \cdot \left(1 - \frac{\dot{I}t}{I_{\mathrm{crit},0}}\right)$ to account for an effective energy barrier reduction due to the spin torque during the current sweep [91]. $I_{\mathrm{crit},0}$ denotes the critical current at which switching would occur at $T = 0\,\mathrm{K}$. Following a formalism developed by Kurkijärvi [92] the critical current I_{crit} can now be expressed as a function of $\dot{I}$:

$$I_{\mathrm{crit}}(\dot{I}) = I_{\mathrm{crit},0}\left[1 - \frac{k_{\mathrm{B}}T}{E_{\mathrm{b}}} \ln\left(\nu_0 \frac{k_{\mathrm{B}}T}{E_{\mathrm{b}}} \frac{I_{\mathrm{crit},0}}{\dot{I}}\right)\right] \quad . \tag{8.11}$$

Fitting this equation to the acquired data in Fig. 8.17 shows good agreement and leads to critical currents of $I^{+}_{\mathrm{crit},0} = (3.96 \pm 0.04)\,\mu\mathrm{A}$ and $I^{-}_{\mathrm{crit},0} = (-4.90 \pm 0.05)\,\mu\mathrm{A}$. The temperature T in Eq. (8.11) is the experiment temperature and is kept fixed,

	current pulses	current ramps (Kurkijärvi model)	current ramps (extended Kurkijärvi model)
$c_{\mathrm{ST}}^{+}\left[\frac{\mathrm{meV}}{\mu\mathrm{A}}\right]$	18.6 ± 7.1	25.3 ± 0.3	23.3 ± 1.6
$c_{\mathrm{ST}}^{-}\left[\frac{\mathrm{meV}}{\mu\mathrm{A}}\right]$	11.9 ± 7.0	20.4 ± 0.2	18.5 ± 1.4
$c_{\mathrm{JH}}\left[\frac{\mathrm{K}}{\mu\mathrm{A}}\right]$	2.6 ± 2.9	-	≈ 0.75

Table 8.1: Comparison of spin torque and Joule heating coefficients determined by different methods. All experiments are performed with the same probe tip on the island shown in Fig. 8.9.

thus leaving a possible temperature change due to Joule heating unconsidered. Since this heating effect was shown to play an essential role in our experiments by decreasing the effective energy barrier additionally to the spin torque, its negation is here unreasonable. To account for the effect of Joule heating one can introduce an effective temperature T_{eff} and extend the Kurkijärvi model to

$$I_{\mathrm{crit}}(\dot{I}) = I_{\mathrm{crit},0}\left[1 - \frac{k_{\mathrm{B}}T_{\mathrm{eff}}}{E_{\mathrm{b}}}\ln\left(\nu_0\frac{k_{\mathrm{B}}T_{\mathrm{eff}}}{E_{\mathrm{b}}}\frac{I_{\mathrm{crit},0}}{\dot{I}}\right)\right] \quad . \tag{8.12}$$

The linear dependence of the Joule heating on the injected current is here neglected for the sake of simplicity. The effective temperature T_{eff} has then a value that is in between the experimental temperature T and the temperature when switching occurs $T + \Delta T_{\mathrm{JH}}$. Making T_{eff} an open fit parameter leads to a second fit of good agreement with the experimental data covering the previous fit curve (see Fig. 8.17). The fit parameters are here $I_{\mathrm{crit},0}^{+} = (4.3 \pm 0.3)\,\mu\mathrm{A}$, $I_{\mathrm{crit},0}^{-} = (-5.4 \pm 0.4)\,\mu\mathrm{A}$ and $T_{\mathrm{eff}} = (31.8 \pm 0.6)\,\mathrm{K}$, that is an effective temperature increase of $\approx 0.9\,\mathrm{K}$ with respect to the experiment temperature of $T_{\mathrm{exp}} = 30.9\,\mathrm{K}$. To allow for a comparison to the coefficients found in section 8.2, the critical currents found can be expressed in terms of spin torque coefficients by the use of

$$E_{\mathrm{b}} - c_{\mathrm{ST}}^{+,-} I_{\mathrm{crit},0}^{+,-} = 0 \quad .$$

The Joule heating coefficient can be estimated by taking a temperature increase of $\Delta T = T_{\mathrm{eff}} - T_{\mathrm{exp}} = 0.9\,\mathrm{K}$ at a critical current of $I_{\mathrm{crit}}^{+,-} \approx \pm 1.2\mu\mathrm{A}$.

For comparison the resulting coefficients determined from the different experiments and models are summarized in Tab. 8.1. The total negation of the Joule heating within the Kurkijärvi model leads to increased spin torque coefficients in comparison to the values found in the current pulse experiments. This is not

surprising since the entire energy barrier modification at high tunnel currents is ascribed within the Kurkijärvi model to be caused by spin torque only, therefore leading to an overestimation of the spin torque. The introduction of an effective temperature as open fit parameter to extend this model allows for a correction and modifies the values of c_{ST}^{+} and c_{ST}^{-} found before towards lower values. Although this model is still underestimating the effect of Joule heating by assuming a fixed *effective* temperature, its results are on the same order as the coefficients determined by the pulse-triggered switching experiments of section 8.2.

The critical currents determined correspond to local current densities of $j \approx 10^8\,\mathrm{A/cm^2}$, that is two orders of magnitude smaller than found in section 7.2. This is explained by the considerably smaller island size chosen here. For comparison: The experiments of section 7.2 were performed at $T = 50.6\,\mathrm{K}$ on an island consisting of approximately 80 atoms. The critical current estimated for switching a thermally *stable* structure of this size is not realizable within the tunnel regime. Here, the island is formed by approximately 40 iron atoms leading to a smaller energy barrier for magnetization reversal. Further, the injected current covers a major part of the magnetic nanostructure, thus, reducing the critical current densities necessary. The combined Joule heating and spin torque effects are shown to be high enough to allow for the manipulation of these small nanostructures, even in the quasistable regime.

Chapter 9

Summary and Outlook

Within our experimental work we could demonstrate the spin-torque manipulation on the local scale by means of SP-STM. The starting point was the examination of the intrinsic thermal switching behavior of Fe monolayer nanoislands on a W(110) surface. The investigation of the magnetization switching with a variable-temperature SP-STM allowed for the determination of the activation energy barrier E_b and the attempt frequency ν_0 for the magnetization reversal of individual nanoislands. Due to the high lateral resolution of the instrument, the island size and shape dependency of these parameters could be investigated. As a result, a domain wall nucleation and propagation through the nanostructures is found to be the reversal mechanism. Additionally, the determination of static domain wall widths allowed for the calculation of the exchange stiffness A and the anisotropy K of this system. The comparison with values in the literature reveals a discrepancy that is ascribed to different sample qualities.

In the next step, elevated spin-polarized tunnel currents were utilized to manipulate the thermally activated magnetization reversal. The spin-polarized current, delivered by the magnetic probe tip, led to a distinct modification of the intrinsic switching behavior. This was the first demonstration of a spin-transfer torque effect across a vacuum gap, i.e. without mechanical contact between the two electrodes involved. The exerted spin-torque was shown to be polarity dependent, as predicted in Slonczewski's theoretical work and demonstrated in experiments on layered structures. Spin-torque, Joule heating, and Oersted-field contributions were identified and quantified by an analysis of the state dependent magnetization lifetimes. In agreement with the literature, spin-torque and Joule heating were found to vary linearly with the tunnel current. The magnetization reversal is mainly influenced by the combined action of spin-torque and Joule heating, whereas the Oersted field modification of the effective energy barrier is rather small.
Afterwards, the heat-assisted spin-torque magnetization reversal of individual,

quasi-stable nanostructures was demonstrated. High spin-polarized current pulses were applied at a fixed bias polarity. The pulse length, the pulse amplitude, and the bias voltage were changed to gain a qualitative insight into pulse-triggered magnetization reversals. The exerted spin-torque was shown to vary with chosen bias voltage, demonstrating thereby its predicted dependency on the current polarization.
Spin-polarized current pulses and ramps at *alternating* bias polarity were then utilized to control the static magnetization of an iron island. Reliable and reversible magnetization switching was achieved. Here, the investigation of the switching efficiency as function of the pulse parameters permitted a further approach to discriminate and quantify the different effects of spin-torque and Joule heating in the pulse-triggered switching regime. Finally, critical currents for magnetization reversal were determined by triangular current sweeps at different sweep rates. The application of the original and a modified Kurkijärvi model allowed the determination of the spin-torque and the Joule heating coefficients and a comparison of the coefficients found by the different manipulation modes, i.e. the injection of current pulses and current ramps.
In summary, from the experiments the effective energy barrier modification due to the spin-torque was found to be between 2 and 20 meV/μA and the effective temperature elevation due to Joule heating is around 2 K/μA. Despite of a polarization dependence, these values vary for the different islands since the effective impact of spin-torque and Joule heating depends on the fraction of the island that was affected by the current injection. This inhomogeneous current distribution causes slightly higher critical current densities $j \approx 10^8\,\mathrm{A/cm^2}$ to be necessary for magnetization reversal compared to those utilized for magnetization reversal in layered devices. Although the structures utilized here were tremendously smaller than the free layer in experiments on tunnel magnetoresistance devices, the macro-spin model turns out to be also applicable here. Nevertheless, size effects are clearly visible and, for instance in the case of Joule heating, desirable.

Further investigations on the lateral dependency of critical currents could shed light on the question about the details of the switching mechanism induced by the spin-torque. Changing the substrate from a W(110) to a Mo(110) surface would allow the investigation of the spin-torque switching in iron monolayer islands that show an out-of-plane magnetization. Additional lateral effects can appear that might have been dominated in our experiments by the Oersted field.
Ongoing theoretical and experimental works [93–95] focus on the correlation between the spin-polarization of the tunnel current and the tip material and apex configuration. Tuning the tip polarization towards higher values gives a further possibility to improve the spin-torque switching efficiency.
Another way to manipulate bigger structures with elevated energy barriers for magnetization reversal could be to nucleate a domain wall at the rim of the struc-

ture and push or pull the wall afterwards through the structure by moving the tip during the current injection. This idea has been the motivation for first theoretical works on the topic of spin-transfer induced domain wall movement in a STM configuration [96].

These findings open the pathway to a wide range of new experiments and manipulation possibilities on the local scale. The SP-STM, already a powerful tool to image in real space on the atomic scale and to manipulate atoms mechanically on a surface, now is demonstrated to be capable of controlled spin-transfer torque manipulation. The local delivery of a spin-polarized current by the STM probe tip allows the reliable control of static magnetic structures at simultaneously achieved ultimate resolution. The usage of non-local external magnetic fields that affect the whole sample (and eventually the tip) is now dispensable. Additionally, antiferromagnetic nanostructures that remain unaffected by external magnetic fields might now be in range to be controllably manipulated and investigated further. The domain creation and manipulation in more complex structures is now closer. The gap between the spin-polarized magnetization manipulation of atoms and molecules towards solid state devices as nanopillars is closing. Further experiments in this intermediate regime should help to understand the crossover from the single atom spin manipulation in the full quantum mechanical picture [19, 97] to the control of bigger devices and their many body effects.

Bibliography

[1] W. Thomson. *The bakerian lecture: – on the electro-dynamic properties of metals*. Proceedings of the Royal Society of London **8**:(1856), 50.

[2] J. J. Thomson. *Cathode rays*. Philosophical Magazine **44**:(1897), 293.

[3] W. Gerlach and O. Stern. *Der experimentelle Nachweis der Richtungsquantelung im Magnetfeld*. Zeitschrift für Physik A: Hadrons and Nuclei **9**:(1922), 349. ISSN 0939-7922. 10.1007/BF01326983.

[4] M. Jullière. *Tunneling between ferromagnetic films*. Physics Letters A **54**:(1975), 225.

[5] L. Berger. *Emission of spin waves by a magnetic multilayer traversed by a current*. Physical Review B **54**, 13:(1996), 9353.

[6] J. C. Slonczewski. *Current-driven excitation of magnetic multilayers*. Journal of Magnetism and Magnetic Materials **159**:(1996), L1.

[7] J. A. Katine, F. J. Albert, R. A. Buhrman, E. B. Myers, and D. C. Ralph. *Current-driven magnetization reversal and spin-wave excitations in Co/Cu/Co pillars*. Phys. Rev. Lett. **84**, 14:(2000), 3149.

[8] Y. Huai, F. Albert, P. Nguyen, M. Pakala, and T. Valet. *Observation of spin-transfer switching in deep submicron-sized and low-resistance magnetic tunnel junctions*. Applied Physics Letters **84**, 16:(2004), 3118.

[9] G. D. Fuchs, N. C. Emley, I. N. Krivorotov, P. M. Braganca, E. M. Ryan, S. I. Kiselev, J. C. Sankey, D. C. Ralph, R. A. Buhrman, and J. A. Katine. *Spin-transfer effects in nanoscale magnetic tunnel junctions*. Appl. Phys. Lett. **85**:(2004), 1205.

[10] S. S. P. Parkin, C. Kaiser, A. Panchula, P. M. Rice, B. Hughes, M. Samant, and S.-H. Yang. *Giant tunnelling magnetoresistance at room temperature with MgO (100) tunnel barriers*. Nat Mater **3**, 12:(2004), 862.

[11] J. Katine and E. E. Fullerton. *Device implications of spin-transfer torques*. J. Magn. Magn. Mater. **320**, 7:(2008), 1217 .

[12] J. Åkerman. *Toward a universal memory.* Science **308**, 5721:(2005), 508.

[13] Y. Huai. *Spin-transfer torque MRAM (STT-MRAM): Challeges and prospects.* AAPPS Bulletin **18**:(2008), 33.

[14] G. Binnig, H. Rohrer, C. Gerber, and E. Weibel. *Tunneling through a controllable vacuum gap.* Applied Physics Letters **40**, 2:(1982), 178.

[15] G. Binnig, H. Rohrer, C. Gerber, and E. Weibel. *Surface studies by scanning tunneling microscopy.* Phys. Rev. Lett. **49**, 1:(1982), 57.

[16] R. Wiesendanger, H. J. Güntherodt, G. Güntherodt, R. J. Gambino, and R. Ruf. *Observation of vacuum tunneling of spin-polarized electrons with the STM.* Phys. Rev. Lett. **65**:(1990), 247.

[17] S. Heinze, M. Bode, A. Kubetzka, O. Pietzsch, X. Nie, S. Blügel, and R. Wiesendanger. *Real-space imaging of two-dimensional antiferromagnetism on the atomic scale.* Science **288**:(2000), 1805.

[18] F. Meier, L. Zhou, J. Wiebe, and R. Wiesendanger. *Revealing magnetic interactions from single-atom magnetization curves.* Science **320**, 5872:(2008), 82.

[19] S. Loth, K. von Bergmann, M. Ternes, A. F. Otte, C. P. Lutz, and A. J. Heinrich. *Controlling the state of quantum spins with electric currents.* Nature Physics **6**, 4:(2010), 1. ISSN 1745-2473.

[20] S.-W. Hla. *Scanning tunneling microscopy single atom/molecule manipulation and its application to nanoscience and technology.* Journal of Vacuum Science & Technology B: Microelectronics and Nanometer Structures **23**, 4:(2005), 1351.

[21] J. Tersoff and D. R. Hamann. *Theory of the STM.* Phys. Rev. B **31**:(1985), 805.

[22] J. Bardeen. *Tunnelling from a many-particle point of view.* Physical Review Letters **6**:(1961), 57.

[23] R. Wiesendanger. *Scanning Probe Microscopy and Spectroscopy.* Cambridge University Press, Cambridge, New York (1994).

[24] O. Fruchart, P. O. Jubert, M. Eleoui, F. Cheynis, B. Borca, P. David, V. Santonacci, A. Liénard, M. Hasegawa, and C. Meyer. *Growth modes of Fe(110) revisited: a contribution of self-assembly to magnetic materials.* Journal of Physics: Condensed Matter **19**, 5:(2007), 053001.

[25] J. C. Slonczewski. *Conductance and exchange coupling of two ferromagnets separated by a tunneling barrier.* Phys. Rev. B **39**:(1989), 6995.

[26] D. Wortmann, S. Heinze, P. Kurz, G. Bihlmayer, and S. Blügel. *Resolving complex atomic-scale spin structures by spin-polarized scanning tunneling microscopy.* Phys. Rev. Lett. **86**:(2001), 4132.

[27] R. Wiesendanger. *Spin mapping at the nanoscale and atomic scale.* Rev. Mod. Phys. **81**, 4:(2009), 1495.

[28] G. Binnig and D. P. E. Smith. *Single-tube three-dimensional scanner for scanning tunneling microscopy.* Review of Scientific Instruments **57**, 8:(1986), 1688.

[29] I. N. Krivorotov, N. C. Emley, J. C. Sankey, S. I. Kiselev, D. C. Ralph, and R. A. Buhrman. *Time-domain measurements of nanomagnet dynamics driven by spin-transfer torques.* Science **307**, 5707:(2005), 228.

[30] E. B. Myers, D. C. Ralph, J. A. Katine, R. N. Louie, and R. A. Buhrman. *Current-induced switching of domains in magnetic multilayer devices.* Science **285**:(1999), 867.

[31] R. Koch, G. Grinstein, G. Keefe, Y. Lu, P. Trouilloud, W. Gallagher, and S. Parkin. *Thermally assisted magnetization reversal in submicron-sized magnetic thin films.* Phys. Rev. Lett. **84**:(2000), 5419.

[32] M. D. Stiles and A. Zangwill. *Anatomy of spin transfer torque.* Phys. Rev. B **66**:(2002), 014407.

[33] J. C. Slonczewski. *Currents, torques, and polarization factors in magnetic tunnel junctions.* Phys. Rev. B **71**, 2:(2005), 024411.

[34] J. Z. Sun. *Spin angular momentum transfer in current-perpendicular nanomagnetic junctions.* IBM J. Res. & Dev. **50**:(2006), 81.

[35] D. L. Landau and E. M. Lifshitz. *On the theory of the dispersion of magnetic permeability in ferromagnetic bodies.* Phys. Z. Sowjetunion **8**:(1935), 153.

[36] W. F. Brown. *Thermal fluctuations of a single-domain particle.* Physical Review **130**:(1963), 1677.

[37] Z. Li and S. Zhang. *Thermally assisted magnetization reversal in the presence of a spin-transfer torque.* Phys. Rev. B **69**, 13:(2004), 134416.

[38] *Omicron NanoTechnology GmbH, 65232 Taunusstein, Germany, http://www.omicron.de.*

[39] *CryoVac GmbH, 53842 Troisdorf, Germany, http://www.cryovac.de.*

[40] T. Hänke. *A new variable-temperature scanning tunneling microscope and temperature dependent spin-polarized scanning tunneling microscopy on the Cr(001) surface.* Ph.D. thesis, Universität Hamburg (2005).

[41] O. Pietzsch, A. Kubetzka, D. Haude, M. Bode, and R. Wiesendanger. *A low-temperature ultrahigh vacuum scanning tunneling microscope with a split-coil magnet and a rotary motion stepper motor for high spatial resolution studies of surface magnetism.* Review of Scientific Instruments **71**, 2:(2000), 424.

[42] *Femto DLPCA-200, FEMTO Messtechnik GmbH, 10179 Berlin, Germany, http://www.femto.de.*

[43] *Stanford Research Systems, DSP Lock-In Amplifier, Model SR830.*

[44] M. Bode. *Spin-polarized scanning tunneling microscopy.* Reports of Progress in Physics **66**:(2003), 523.

[45] R. Wiesendanger, I. V. Shvets, D. Bürgler, G. Tarrach, H. J. Güntherodt, J. M. D. Coey, and S. Gräser. *Topographic and magnetic-sensitive stm study of magnetite.* Science **255**:(1992), 583.

[46] A. L. Bassi, C. S. Casari, D. Cattaneo, F. Donati, S. Foglio, M. Passoni, C. E. Bottani, P. Biagioni, A. Brambilla, M. Finazzi, F. Ciccacci, and L. Duò. *Bulk Cr tips for scanning tunneling microscopy and spin-polarized scanning tunneling microscopy.* Applied Physics Letters **91**:(2007), 173120.

[47] A. Kubetzka, M. Bode, O. Pietzsch, and R. Wiesendanger. *Spin-polarized scanning tunneling microscopy with antiferromagnetic probe tips.* Phys. Rev. Lett. **88**:(2002), 057201.

[48] M. Bode, O. Pietzsch, A. Kubetzka, S. Heinze, and R. Wiesendanger. *Experimental evidence for intra-atomic noncollinear magnetism at thin film probe tips.* Phys. Rev. Lett. **86**, 10:(2001), 2142.

[49] T. K. Yamada, M. M. J. Bischoff, T. Mizoguchi, and H. van Kempen. *Use of voltage pulses to detect spin-polarized tunneling.* Applied Physics Letters **82**, 9:(2003), 1437.

[50] M. Bode, S. Krause, L. Berbil-Bautista, S. Heinze, and R. Wiesendanger. *On the preparation and electronic properties of clean W(110) surfaces.* Surface Science **601**:(2007), 3308.

[51] H. J. Elmers, J. Hauschild, H. Höche, U. Gradmann, H. Bethge, D. Heuer, and U. Köhler. *Submonolayer magnetism of Fe/W(110): finite width scaling and percolation between islands.* Phys. Rev. Lett. **73**:(1994), 898.

[52] H. Bethge, D. Heuer, C. Jensen, K. Reshöft, and U. Köhler. *Misfit-related effects in the epitaxial growth of Fe/W(110).* Surf. Sci. **331–333**:(1995), 878.

[53] J. Hauschild, H. J. Elmers, and U. Gradmann. *Dipolar superferromagnetism in monolayer nanostripes of Fe(110) on vicinal W(110) surfaces.* Phys. Rev. B **57**, 2:(1998), R677.

[54] H. J. Elmers, G. Liu, and U. Gradmann. *Magnetometry of the ferromagnetic monolayer Fe(110) on W(110) coated with Ag.* Phys. Rev. Lett. **63**, 5:(1989), 566.

[55] U. Gradmann, G. Liu, H. J. Elmers, and M. Przybylski. *The ferromagnetic monolayer Fe(110) on W(110).* Hyperfine Interactions **57**:(1990), 1845.

[56] A. Kubetzka, O. Pietzsch, M. Bode, and R. Wiesendanger. *Magnetism of nanoscale Fe islands studied by spin-polarized scanning tunneling spectroscopy.* Phys. Rev. B **63**:(2001), 140407.

[57] J. Hauschild, U. Gradmann, and H. J. Elmers. *Perpendicular magnetization and dipolar antiferromagnetism in double layer nanostripe arrays of Fe(110) on W(110).* Applied Physics Letters **72**, 24:(1998), 3211.

[58] M. Bode. *Strukturelle und elektronische Eigenschaften ultradünner Eisenfilme auf W(110).* Ph.D. thesis, Universität Hamburg (1996).

[59] U. Gradmann and G. Waller. *Periodic lattice distortions in epitaxial films of Fe(110) on W(110).* Surface Science **116**, 3:(1982), 539 . ISSN 0039-6028.

[60] D. Sander, R. Skomski, A. Enders, C. Schmidthals, D. Reuter, and J. Kirschner. *The correlation between mechanical stress and magnetic properties of ultrathin films.* Journal of Physics D: Applied Physics **31**, 6:(1998), 663.

[61] U. Gradmann, J. Korecki, and G. Waller. *In-plane magnetic surface anisotropies in Fe(110).* Appl. Phys. A **39**:(1986), 101.

[62] H. J. Elmers, J. Hauschild, and U. Gradmann. *Critical behavior of the uniaxial ferromagnetic monolayer of Fe on W(110).* Physical Review B **54**:(1996), 15224.

[63] M. Pratzer, H. J. Elmers, M. Bode, O. Pietzsch, A. Kubetzka, and R. Wiesendanger. *Atomic-scale magnetic domain walls in quasi-one-dimensional Fe nanostripes.* Physical Review Letters **87**:(2001), 127201.

[64] M. Pratzer and H. J. Elmers. *Domain wall energy in quasi-one-dimensional Fe/W(110) nanostripes.* Phys. Rev. B **67**, 9:(2003), 094416.

[65] N. Weber, K. Wagner, H. J. Elmers, J. Hauschild, and U. Gradmann. *Nanoscale spatial switching of magnetic anisotropy in pseudomorphic Fe(110) on W(110).* Phys. Rev. B **55**:(1997), 14121.

[66] M. Bode, A. Kubetzka, O. Pietzsch, and R. Wiesendanger. *Spin-polarized scanning tunneling spectroscopy of Fe-nanowires.* Appl. Phys. A **72**:(2001), S149.

[67] H. J. Elmers, J. Hauschild, and U. Gradmann. *Onset of perpendicular magnetization in nanostripe arrays of Fe on stepped W(110).* Phys. Rev. B **59**:(1999), 3688.

[68] S. Meckler, N. Mikuszeit, A. Preßler, E. Y. Vedmedenko, O. Pietzsch, and R. Wiesendanger. *Real-space observation of a right-rotating inhomogeneous cycloidal spin spiral by spin-polarized scanning tunneling microscopy in a triple axes vector magnet.* Phys. Rev. Lett. **103**, 15:(2009), 157201.

[69] R. Kurzawa, K.-P. Kämper, W. Schmitt, and G. Güntherodt. *Spin-resolved photoemission study of in situ grown epitaxial Fe layers on W(110).* Sol. State Commun. **60**:(1986), 777.

[70] A. Wachowiak, J. Wiebe, M. Bode, O. Pietzsch, M. Morgenstern, and R. Wiesendanger. *Direct observation of internal spin structure of magnetic vortex cores.* Science **298**:(2002), 577.

[71] M. L. Néel. *Theorie du trainage magnetique des ferromagnetiques en grains fins avec application aux terres cuites.* Ann. Géophys. **5**:(1949), 99.

[72] W. Wernsdorfer, B. Doudin, D. Mailly, K. Hasselbach, A. Benoit, J. Meier, J.-P. Ansermet, and B. Barbara. *Nucleation of magnetization reversal in indvidual nanosized nickel wires.* Phys. Rev. Lett. **77**:(1996), 1873.

[73] W. Wernsdorfer, E. B. Orozco, K. Hesselbach, A. Benoit, B. Barbara, N. Demoney, A. Loiseau, H. Pascard, and D. Mailly. *Experimental evidence of the Néel-Brown model of magnetization reversal.* Phys. Rev. Lett. **78**:(1997), 1791.

[74] A. Hubert and R. Schäfer. *Magnetic Domains.* Springer (1998).

[75] G. Ehrlich. *Atomic displacements in one- and two-dimensional diffusion.* The Journal of Chemical Physics **44**, 3:(1966), 1050.

[76] T. W. McDaniel. *Ultimate limits to thermally assisted magnetic recording.* Journal of Physics: Condensed Matter **17**, 7:(2005), R315.

[77] D. Atkinson, D. A. Allwood, G. Xiong, M. D. Cooke, C. C. Faulkner, and R. P. Cowburn. *Magnetic domain-wall dynamics in a submicrometre ferromagnetic structure.* Nature Materials **2**:(2003), 85.

[78] W. Wernsdorfer, K. Hasselbach, A. Benoit, B. Barbara, B. Doudin, J. Meier, J.-P. Ansermet, and D. Mailly. *Measurement of magnetization switching in individual nickel nanowires.* Phys. Rev. B **55**:(1997), 11552.

[79] N. D. Rizzo, T. J. Silva, and A. B. Kos. *Relaxation times for magnetization reversal in a high coercivity magnetic thin film.* Phys. Rev. Lett. **83**, 23:(1999), 4876.

[80] D. Hinzke and U. Nowak. *Magnetization switching in a Heisenberg model for small ferromagnetic particles.* Physical Review B **58**:(1998), 265.

[81] U. Nowak and D. Hinzke. *Magnetization switching in small ferromagnetic particles: Nucleation and coherent rotation.* Journal of Applied Physics **85**:(1999), 4337.

[82] P. Hänggi, P. Talkner, and M. Borkovec. *Reaction-rate theory: fifty years after Kramers.* Rev. Mod. Phys. **62**, 2:(1990), 251.

[83] A. Kubetzka, O. Pietzsch, M. Bode, and R. Wiesendanger. *Spin-polarized scanning tunneling microscopy study of 360 degree walls in an external magnetic field.* Phys. Rev. B **67**:(2003), 020401.

[84] S. Rusponi, T. Cren, N. Weiss, M. Epple, P. Buluschek, L. Claude, and H. Brune. *The remarkable difference between surface and step atoms in the magnetic anisotropy of two-dimensional nanostructures.* Nature Materials **2**:(2003), 546.

[85] J. C. Slonczewski. *Excitation of spin waves by an electric current.* J. Magn. Magn. Mater. **195**:(1999), L261.

[86] I. Bat'ko and M. Bat'ková. *Calorimetric tunneling study of heat generation in metal-vacuum-metal tunnel junctions.* Eur. Phys. J. Appl. Phys. **31**, 3:(2005), 191.

[87] H. Goldenberg. *Heat flow in an infinite medium heated by a sphere.* British Journal of Applied Physics **3**:(1952), 296.

[88] M. P. Seah and W. A. Dench. *Quantitative electron spectroscopy of surfaces: A standard data base for electron inelastic mean free paths in solids.* Surface and Interface Analysis **1**:(1979), 2.

[89] I. N. Krivorotov, N. C. Emley, A. G. F. Garcia, J. C. Sankey, S. I. Kiselev, D. C. Ralph, and R. A. Buhrman. *Temperature dependence of spin-transfer-induced switching of nanomagnets.* Phys. Rev. Lett. **93**, 16:(2004), 166603.

[90] J. Tersoff and D. R. Hamann. *Theory and application for the scanning tunneling microscope.* Phys. Rev. Lett. **50**:(1983), 1998.

[91] E. B. Myers, F. J. Albert, J. C. Sankey, E. Bonet, R. A. Buhrman, and D. C. Ralph. *Thermally activated magnetic reversal induced by a spin-polarized current.* Phys. Rev. Lett. **89**, 19:(2002), 196801.

[92] J. Kurkijärvi. *Intrinsic fluctuations in a superconducting ring closed with a josephson junction.* Phys. Rev. B **6**, 3:(1972), 832.

[93] A. Schlenhoff, S. Krause, G. Herzog, and R. Wiesendanger. *Bulk Cr tips with full spatial magnetic sensitivity for spin-polarized scanning tunneling microscopy.* Applied Physics Letters **97**, 8:(2010), 083104.

[94] S. F. Ceballos, G. Mariotto, S. Murphy, and I. V. Shvets. *Fabrication of magnetic STM probes and their application to studies of the Fe_3O_4(001) surface.* Surface Science **523**, 1-2:(2003), 131 . ISSN 0039-6028.

[95] P. Ferriani, C. Lazo, and S. Heinze. *Origin of the spin polarization of magnetic scanning tunneling microscopy tips.* Phys. Rev. B **82**, 5:(2010), 054411.

[96] T. Stapelfeldt, R. Wieser, E. Vedmedenko, and R. Wiesendanger. *Domain wall manipulation with a magnetic tip.* Phys. Rev. Lett., accepted .

[97] F. Delgado, J. J. Palacios, and J. Fernández-Rossier. *Spin-transfer torque on a single magnetic adatom.* Phys. Rev. Lett. **104**, 2:(2010), 026601.

Publications

- S. Krause, L. Berbil-Bautista, G. Herzog, M. Bode, and R. Wiesendanger, *Current-Induced Magnetization Switching with a Spin-Polarized Scanning Tunneling Microscope*, Science **317**, 1537 (2007).
- S. Krause, G. Herzog, T. Stapelfeldt, L. Berbil-Bautista, M. Bode, E. Y. Vedmedenko, and R. Wiesendanger, *Magnetization Reversal of Nanoscale Islands: How Size and Shape Affect the Arrhenius Prefactor*, Physical Review Letters **103**, 127202 (2009).
- G. Herzog, S. Krause, and R. Wiesendanger, *Heat assisted spin torque switching of quasistable nanomagnets across a vacuum gap*, Applied Physics Letters **96**, 102505 (2010).
- A. Schlenhoff, S. Krause, G. Herzog, and R. Wiesendanger, *Bulk Cr tips with full spatial magnetic sensitivity for spin-polarized scanning tunneling microscopy*, Applied Physics Letters **97**, 083104 (2010).
- S. Krause, G. Herzog, A. Schlenhoff, and R. Wiesendanger, *Quantification of Joule heating and spin-torque on the atomic scale using a spin-polarized scanning tunneling microscope*, (submitted, 2011).

Conferences

Contributed talks

- 2007-12-10
  G. Herzog, S. Krause, L. Berbil-Bautista, M. Bode, and R. Wiesendanger, *Superparamagnetic switching behavior of nanoislands Fe/W(110)*, Graduate-Class Workshop GK1268, Reinbek (Germany)

- 2008-02-25
  G. Herzog, S. Krause, and R. Wiesendanger, *The Effect of Step Atoms on the Switching Behavior of Superparamagnetic Nanoislands*, 72$^{\text{nd}}$ Spring Conference, Deutsche Physikalische Gesellschaft, Berlin (Germany)

- 2008-09-22
  G. Herzog, *Observing and Manipulating Magnetic Nanostructures by SP-STM*, SFB 668 Workshop, St. Peter Ording (Germany)

- 2008-10-30
  G. Herzog, *Investigations of Superparamagnetic Nanoislands - Current Status*, Graduate-Class Workshop GK1268, Husum (Germany)

- 2009-10-09
  G. Herzog, S. Krause, and R. Wiesendanger, *Current-Induced Magnetization Switching of Thermally Quasistable Nanoislands - Our New Toolbox*, Graduate-Class Workshop GK1268, Schwerin (Germany)

- 2010-03-25
  G. Herzog, S. Krause, A. Emmenegger and R. Wiesendanger, *Heat assisted Spin Torque Switching of Nanomagnets by SP-STM*, 74$^{\text{th}}$ Spring Conference, Deutsche Physikalische Gesellschaft, Regensburg (Germany)

- 2010-08-20
  G. Herzog, S. Krause, A. Emmenegger and R. Wiesendanger, *Spin Torque Switching of Nanomagnets by SP-STM*, SP-STM3, Seoul (South Korea)

- 2010-08-24
  G. Herzog, S. Krause, A. Emmenegger and R. Wiesendanger, *Spin Torque*

Switching of Nanomagnets by SP-STM, International Conference on Nanoscience and Technology, Beijing (China)

- 2010-10-14
  G. Herzog, S. Krause, A. Emmenegger and R. Wiesendanger, *Heat assisted Spin Torque Switching of Nanomagnets by SP-STM*, Graduate-Class Workshop GK1268, Jever (Germany)

Posters

- 2008-07-16 & 18
  G. Herzog, S. Krause, L. Berbil-Bautista, T. Stapelfeldt, E. Y. Vedmedenko, M. Bode, and R. Wiesendanger, *Observing the Thermal Switching Behavior of Superparamagnetic Nanoislands by SP-STM*, NSS5 / SP-STM2, Athens, Ohio (USA).

- 2008-07-22
  G. Herzog, S. Krause, L. Berbil-Bautista, T. Stapelfeldt, E. Y. Vedmedenko, M. Bode, and R. Wiesendanger, *Observing the Thermal Switching Behavior of Superparamagnetic Nanoislands by SP-STM*, International Conference on Nanoscience and Technology, Keystone, Colorado (USA).

- 2008-09-11 & 12
  G. Herzog, L. Zhou, S. Krause, F. Meier, J. Wiebe, and R. Wiesendanger, *Spin-Polarized Scanning Tunneling Microscopy and Spectroscopy*, 2$^{\text{nd}}$ International Summer School of the GrK "Physics of Functional Micro- and Nanostructures", Hamburg (Germany).

- 2009-07-28
  G. Herzog, S. Krause, L. Berbil-Bautista, M. Bode, and R. Wiesendanger, *Investigation of the Thermal Switching Behavior of Superparamagnetic Nanoislands by SP-STM*, International Conference on Magnetism (ICM), Karlsruhe (Germany).

- 2009-09-17 & 18
  G. Herzog, L. Zhou, S. Krause, F. Meier, J. Wiebe, and R. Wiesendanger, *Spin-Polarized Scanning Tunneling Microscopy and Spectroscopy*, 3$^{\text{rd}}$ International Summer School of the GrK "Physics of Functional Micro- and Nanostructures", Hamburg (Germany).

- 2010-09-16 & 17
  G. Herzog, P. Löptien, L. Zhou, S. Krause, F. Meier, J. Wiebe, and R. Wiesendanger, *Spin-Polarized Scanning Tunneling Microscopy and Spectroscopy*, 4$^{\text{th}}$ International Summer School of the GrK "Physics of Functional Micro- and Nanostructures", Hamburg (Germany).

Danksagung

An dieser Stelle möchte ich einigen Menschen, die zum Gelingen dieser Arbeit beigetragen haben, meinen Dank aussprechen.

Herrn Prof. Dr. Wiesendanger danke ich für die Möglichkeit, meine Promotion in seiner Arbeitsgruppe, unter hervorragenden Arbeitsbedingungen durchführen zu können. Er hat meine Arbeit stets unterstützt, mir Vertrauen entgegengebracht und viele Freiheiten gewährt. Dafür und für die Übernahme der Erstgutachten meiner Dissertation und Disputation danke ich ihm.

Unter der Leitung von Herrn Prof. Dr. Merkt durfte ich den Großteil meiner Promotionszeit als Mitglied des Graduiertenkollegs 1286 verbringen. Wir Stipendiaten profitierten und profitieren von seinem großen Engagement für unser Graduiertenkolleg, sowohl in "physikalischen" als auch in "un-physikalischen" Belangen. Hierfür möchte ich ihm an dieser Stelle danken.

Für die Übernahme der Zweitgutachten bedanke ich mich bei Herrn Prof. Dr. Merkt als Gutachter meiner Dissertation, und Herrn Priv.-Doz. Dr. habil. Guido Meier als Gutachter meiner Disputation.

Seit meinem ersten Tag in dieser Arbeitsgruppe stand Dr. Stefan Krause mir Tag für Tag mit Rat und Tat zur Seite. In vielen gemeinsamen Arbeitsstunden brachte er mir im Labor die Meßapparatur näher, führte mich in die SP-STM Technik ein und liess mich an seinem wissenschaftlichen Erfahrungsschatz teilhaben. Die gute, jahrelange Zusammenarbeit am Experiment und die zahlreichen, fruchtbaren Diskussionen über vergangene und anstehende Messungen und Ergebnisse trugen entscheidend zum Gelingen dieser Arbeit bei. Dafür sei ihm hier gedankt.

Mit dem Beginn meiner Promotion stiess Dipl.-Phys. Anika Schlenhoff zu uns und erwies sich als wertvolle Erweiterung unseres Teams. Unsere gemeinsame Laborarbeit, sowohl bei Messungen als auch bei Reparaturarbeiten, war stets von kollegialer Unterstützung geprägt. Ich danke ihr für die produktive Arbeitsatmosphäre, in der wir viele Fragestellungen diskutierten und das weitere Vorgehen beratschlagten. Ich wünsche ihr und dem gesamten wissenschaftlichen Nach-

wuchs von Lab-018 weiterhin viel Erfolg und zahlreiche, spannende Experimente an diesem Messaufbau.

Dem gesamten Team um und mit Dr. habil. Elena Y. Vedmedenko sei für die gute Zusammenarbeit gedankt. Insbesondere Dr. Robert Wieser ist immer sowohl für ein gutes “Theorie vs. Experiment”-, als auch “Theorie vs. Theorie”-Gespräch zu haben.

Dr. Jessica Bickel und Dr. Berenike Schröder schulde ich Dank für die inhaltlichen und sprachlichen Korrekturen an dieser Arbeit. Beide hatten mir ihre Hilfe spontan zugesagt und meine Arbeit zügig und gewissenhaft überprüft.

Unter der Anleitung von Dr. André Kubetzka habe ich während des Praktikums meine ersten Experimente mit einem Rastertunnelmikroskop durchgeführt. Ihm verdanke ich mein Interesse und die Faszination für diese Technik.

Die gesamte Gruppe R zeichnet sich durch ihre Vielfalt und ihren hohen Erfahrungsschatz aus. Ich danke dieser Gruppe für die gute Arbeitsatmosphäre, die sich in stetiger Bereitschaft zu produktiven Diskussionen und Hilfestellungen widerspiegelt.

Ebenso danke ich dem gesamten Graduiertenkolleg 1286. Das Zusammenkommen unserer Gruppe, aber auch einzelner Mitglieder, war stets von gegenseitigem wissenschaftlichen Interesse und wertvollen Diskussionen geprägt.

Die vorgestellten Experimente benötigten eine kontinuierliche Zuführung von flüssigem Helium. Daher sei an dieser Stelle dem gesamten Team um die Helium-Verflüssiger-Anlage für ihre emsige und zuverlässige Arbeit gedankt.

Meiner Familie und den Freunden, die mich in den letzten Jahren begleitet haben, schulde ich einen besonderen Dank. Ohne ihre anwährende Unterstützung und ihren stetigen Zuspruch wäre die Fertigstellung dieser Arbeit nicht möglich gewesen.

⊙

Erklärung

Hiermit erkläre ich, dass ich die vorliegende Promotionsarbeit selbständig und ohne fremde Hilfe verfasst habe. Andere als die von mir angegebenen Quellen und Hilfsmittel sind nicht verwendet worden. Den benutzten Werken wörtlich oder inhaltlich entnommene Stellen sind als solche kenntlich gemacht.

Hamburg, im Mai 2011